8-2005

Study of Rheological Properties of Polymeric Liquids by Using Multiple-Mode Models

Bangwu Jiang
University of Tennessee - Knoxville

To the Graduate Council:

I am submitting herewith a dissertation written by Bangwu Jiang entitled "Study of Rheological Properties of Polymeric Liquids by Using Multiple-Mode Models." I have examined the final electronic copy of this dissertation for form and content and recommend that it be accepted in partial fulfillment of the requirements for the degree of Doctor of Philosophy, with a major in Chemical Engineering.

Brian J. Edwards, Major Professor

We have read this dissertation and recommend its acceptance:

John Collier, Simioan Petrovan, Bin Hu

Accepted for the Council:
Dixie L. Thompson

Vice Provost and Dean of the Graduate School

(Original signatures are on file with official student records.)

To the Graduate Council:

We are submitting herewith a dissertation written by Bangwu Jiang entitled "Study of Rheological Properties of Polymeric Liquids by Using Multiple-Mode Models." We have examined the final electronic copy of this dissertation for form and content and recommend that it be accepted in partial fulfillment of the requirements for the degree of Doctor of Philosophy, with a major in Chemical Engineering.

Brian J. Edwards
Major Professor

David J. Keffer
Major Professor

We have read this dissertation
and recommend its acceptance.

John Collier

Simioan Petrovan

Bin Hu

Acceptance for the Council:

Anne Mayhew

Vice Chancellor and Dean of Graduate Studies
(Original signatures are on file with official student records.)

Study of Rheological Properties of Polymeric Liquids by Using Multiple-Mode Models

A Dissertation
Presented for the
Doctor of Philosophy
Degree
The University of Tennessee, Knoxville

Bangwu Jiang
August, 2005

Abstract

Knowledge of the rheological properties of non-Newtonian fluids is critical for modeling in polymer-processing equipment such as injection molders, extruders, and blow molders. Rheological measurements can be obtained through standard flows, such as shear flow and elongational flow. In our research, we modeled the rheological properties of polymeric fluids in several types of experiments: transient and steady shear flow, small amplitude oscillatory shear flow, transient elongational flow, and step-strain shear flow.

The accuracy of modeling calculations depends critically on the performance of the rheological model used. Differential constitutive models with a single relaxation time can be used for exploratory fluid dynamics research and provide insight into the qualitative effects of viscoelasticity in complex flow fields. However, differential models with a single relaxation time give a poor quantitative description of rheological properties, since most non-Newtonian media exhibit not just one, but a whole spectrum of relaxation times; therefore multiple relaxation modes models were used in our research.

One of the coupled linear relaxation models, the Two Coupled Maxwell Modes (TCMM) Model, was used to describe quantitatively shear-thickening behavior, which can be observed under certain conditions for high molecular weight polymers dissolved in low viscosity solvents. In this case, the shear viscosity of the polymer solution increases with increasing shear rate. A full parameterization of the TCMM Model to the experimental data from the literature provided a thorough understanding of the

significance of the model parameters and a clear insight into the peculiar behavior of shear thickening in dilute polymer solutions.

The primary part of the research focused on models with linear springs. A typical, industrial-grade, low-density polyethylene polymer was studied using three types of multi-mode models: i) uncoupled linear relaxation models; ii) coupled linear relaxation models; iii) uncoupled non-linear relaxation models. The data from small amplitude oscillatory shear flow and steady shear flow were fitted to obtain the parameters of the different models using the Nelder and Mead Downhill Simplex method. Then the predictions for the other standard flows mentioned in the first paragraph were compared with experimental data. This allowed us to determine the degree of the performance of the different models with regards to the corresponding system studied. Overall evaluations of model performance were presented in detail.

Finally, we tested the effects of spring type on the performance of the models described above. We replaced the linear elastic springs in all of the prior models with nonlinear springs to determine whether this would improve model performance in elongational flow. The Finitely-Extensible Nonlinear Elastic Spring Model was used to describe the nonlinear elastic springs. The result was negative, however: no improvement was obtained over the linear spring models and more parameters were present which required further fitting to experimental data.

Dedication

This dissertation is dedicated to my parents, Xingshu Jiang and Sulan Zhang, for their hard work and deep tolerance in raising me up; to my wife, Echo, for believing in me and encouraging me to explore new fields; to my son, Joshua, who puts more responsibilities in my heart.

Acknowledgements

I wish to thank Dr. Brian Edwards and Dr. David Keffer for their continual guidance and support in this research work. I also wish to thank the members of our research group, in particularly Prajakta Kamerkar, for inspiring discussions, warm-hearted help and encouragement. I would like to thank the Department of Chemical Engineering at the University of Tennessee, Knoxville for the financial support that made this work possible. I would also like to thank all my committee members for helpful advice. Finally I greatly appreciate the encouragement and support from my family and friends.

Table of Contents

List of Tables

List of Figures

Nomenclature

ACER	Advanced Capillary Extrusion Rheometer
ARES	Advanced Rheometrics Expansion System
EWMM	The Extended White/Metzner Model
FENE springs	Finitely extensible nonlinear elastic spring
LDPE	Low-density Polyethylene
MCMM Model	Multiple Coupled Maxwell Modes Model
NMDSM	Nelder and Mead Downhill Simplex Method
ODEs	Ordinary differential equations
PEO/e	Polyethylene oxide/ethanol
PE/x	Polyethylene/xylene
PP/t	Polypropylene/tetralin
PP Model	Pom-Pom or Pom-Pon Model
RMS	Relative mean square
FCMM-EWM Mode	Fully Coupled Maxwell Modes Model with the White/Metzner-like extension
FCMM model	Fully Coupled Maxwell Modes Model
PCMM-EWM Mode	Pair-wise Coupled Maxwell Modes Model with the White/Metzner-like extension
PCMM model	Pair-wise Coupled Maxwell Modes Model
PS/d	Polystyrene/decalin
SAOSF	Small-amplitude oscillatory shear flow)
SS	Shear stress
TCMM Model	Two Coupled Maxwell Modes Model
UEWM Model	Uncoupled Extended White/Metzner Model
UMM Model	Uncoupled Maxwell Modes Model
UGM Model	Uncoupled Giesekus Model
FC-FENE-P-EWM Model	Fully Coupled FENE-P Model with the White/Metzner-like extension
A	Deformation tensor
a	The vector spanning the major axis of an ellipsoidal structure
b	the dimensionless maximum possible spring extension
$\mathbf{c}^1$, $\mathbf{c}^2$	Conformation tensors
$\tilde{\mathbf{c}}^i$	Dimensionless conformation tensor
c^*	Critical concentration for coil overlap
f	The size distribution function of the structures
G'	Storage modulus
G''	Loss modulus
H_c	A dimensionless constant $\lambda\dot{\gamma}_c$
k_B	Boltzmann's constant

K_1, K_2	Hookean spring constants
M	Molecular weight
N_A	Avogadro's number
N_1	Fist normal stress difference
n_1, n_2	The effective concentrations of the modes
R	The end-to-end vector of a polymer chain
R_0	The maximum possible spring extension
t	Time
T	The absolute temperature
v	Velocity
λ_1, λ_2	Relaxation times of the modes
θ	Degree of interaction between the two modes
$\sigma_{\alpha\beta}$	Extra stress tensor
$\Delta n''$	Dichroism
η	Viscosity
$\dot{\gamma}_c$	Critical shear rate
$\dot{\gamma}_d$	Shear rate where the linear dichroism displays a global maximum
$\dot{\gamma}_m$	Shear rate where viscosity reaches local maximum
ω	The angular frequency
Ψ	Normal stress coefficient
$\psi(\mathbf{x}, \mathbf{R}, t)$	Distribution function,

PART 1

Introduction

One overall goal of theoretical rheologists for many years has been to obtain a level of understanding of material behavior sufficient to allow for the prediction of viscoelastic properties in arbitrary flow fields. This overall goal is still a significant challenge to theoretical rheologists. Since the rheological properties of polymeric fluids are critical for polymer processing operations, such as injection molding, extruding, and blow molding, from the practical view, a rheological model is required to describe all aspects of viscoelastic properties. Only when a model can meet this stringent requirement, can rheological simulations be used to design intricate flow processes involving real polymeric materials. This goal is still largely unrealized, although a huge effort has been put into rheological modeling. As the computational power has dramatically increased recently, it is time to assess how closely the models available can describe the viscoelastic properties of typical industrial polymers.

In this dissertation, we offer a current assessment of the potential predictive capabilities of several classes of semi-phenomenological models (i.e., models involving empirical parameters). Real polymers have a whole spectrum of relaxation times; therefore, our research focuses on multiple-mode models. The model classes examined in our research are the following: the uncoupled (i.e., no interactions between relaxation modes) linear relaxation models with constant relaxation times, the uncoupled linear relaxation models with variable relaxation times, and uncoupled non-linear relaxation models; these three classes belong to models with uncoupled modes. The other two classes of models examined in our research are those that involved coupled relaxation modes: pair-wise coupled modes models and fully coupled modes models. We also examined the models with both coupling effects and variable relaxation times. The

detailed information on the models examined herein will be given in Parts 3 and 4. The assessment of these semi-phenomenological models can help to judge the capabilities and drawbacks of each model class, which can help guide new modeling research.

The strategy in our research is to fit the models examined herein to a limited amount of easily obtained experimental data of a typical polymer fluid, and then to examine how well each quantitatively predicts experimental data to which the inherent model parameters were not explicitly fit. The methodology used to fit the model parameters to the requisite amount of experimental data is now easily implemented using standard desktop computers. We use the most basic optimization scheme available, the Nelder and Mead Downhill Simplex Method [1.1] in our research to fit model parameters.

In Part 2, one of coupled linear relaxation models, the Two Coupled Maxwell Modes (TCMM) Model, is used to describe quantitatively shear-thickening behavior, which can be observed under certain conditions for high molecular weight polymers dissolved in low viscosity solvents. A full parameterization of the TCMM model was performed by using all of the available experimental data for steady-shear viscosity and dichroism in the literature. Furthermore, functional dependencies of the parameters were determined as functions of temperature, concentration, and molecular weight of the polymer.

In Parts 3 and 4, a typical, industrial, low-density polyethylene (LDPE) polymer is studied using the multiple modes models mentioned above with regard to the rheological properties of polymer melts in diverse flow fields, including (i) transient shear flow, (ii) steady-state shear flow, (iii) small-amplitude oscillatory shear flow, and (iv) transient uniaxial elongational flow. Several classes of multiple-mode rheological

constitutive equations are tested for fitting and predicting viscoelastic flow properties. We fit the phenomenological parameters of each model examined to experimental data taken in small-amplitude oscillatory shear flow and steady shear flow. These parameter values are then used to generate predictions for the transient shear and uniaxial elongational flow experiments, and the predictions are then compared to experimental data. Model successes and failures are discussed, and the outlook for using rheological equations in real design processes is addressed.

In Part 5, we use the same parameters for the models obtained in Part 4 to generate predictions for step-strain experiments, and then compare the predictions with experimental data. The performances of the different models are presented and discussed.

In Part 6, we tried to replace the linear elastic springs in all of the models tested in Parts 4 and 5 with finitely-extensible non-linear elastic (FENE) springs [1.2] to improve the model performances in elongational flow. The well-known FENE-P extension was used to describe the non-linear elastic spring [1.3]. Results and discussions are given in detail in Part 6, but the result was basically negative: the FENE springs provided no improvement over linear springs, and only increased the number of empirical parameters. Finally, we draw conclusions on every part of our research in Part 7.

References

1.1 W.H. Press, W.T. Vettuling, S.A. Tevkolsky, and B.P. Flannery, *Numerical Recipes in Fortran 77*, Cambridge University Press, Cambridge, 1992.

1.2 A.P. G. van Heel, M.A. Hulsen, and B.H.A.A. van den Brule, *J. Non-Newtonian Fluid Mech.*, 1998. **75**: p. 253

1.3 A. N. Beris and B.J. Edwards, *Thermodynamics of Flowing Systems*. 1994, New York: Oxford University Press.

PART 2

Modeling Shear Thickening in Dilute Polymer Solutions: Temperature, Concentration and Molecular Weight Dependence

This part is revised slightly from a paper by the same name published in the "Journal of Applied Polymer Science" in 2003. The full citation is:

B. Jiang, D. J. Keffer, B. J. Edwards, J. N. Allred, "Modeling Shear Thickening in Dilute Polymer Solutions: Temperature, Concentration and Molecular Weight", J. Appl. Polym. Sci. **90,** (2003), 2997-3011.

In this part, "we" refers to my co-authors and myself. My primary contributions include: (1) development of the computational methods; (2) development of the data-fitting strategy; (3) all of the computational work and analysis; (4) most of the writing.

2.1 Introduction

The anomaly of shear thickening, where the viscosity of the solution increases with increasing shear rate, can be observed under certain conditions with high molecular weight polymers dissolved in low viscosity Newtonian solvents. Generally, dilute solutions of high molecular weight polymers dissolved in low viscosity Newtonian solvents display shear thinning behavior, where the viscosity of the solution decreases with increasing shear rate at intermediate and high shear rates [2.1]. However, shear thickening has been observed in some cases; the most recent literature review may be found in [2.2, 2.3]. Although the shear-thinning phenomenon is regarded widely as an intramolecular effect due to the extension and orientation of the polymer chains in solution [2.4], different explanations have been put forth to explain shear thickening [2.5-2.11].

In Figure 2.1[1], we show a typical flow curve displaying shear thickening in a dilute polymer solution at steady state. This experimental behavior of shear thickening was observed by Layec-Raphalen and Wolff [2.12] and Vraholpoulou and McHugh [2.13]. The usual pattern of shear-thinning behavior is evident at low to intermediate shear rates. The viscosity reaches a local minimum with increasing shear rate at $\dot{\gamma}_c$, and then the viscosity begins increasing with increasing shear rate. A local maximum in the viscosity is attained at a very high shear rate, $\dot{\gamma}_m$, followed by a resumption of shear thinning at extremely high shear rates [2.12, 2.13]. At very low shear rates, not evident in Figure 2.1, the solutions presumably display a Newtonian plateau in viscosity relative to shear rate. However, as these solutions are very dilute, and hence their viscosities very low, linear viscoelastic behavior is not available since only high shear rate devices are experimentally manageable.

As mentioned above, the solutions of interest presently are all dilute, meaning the concentration of polymer in solvent is below the critical concentration for coil overlap, c^* [2.2, 2.3, 2.12, 2.13, 2.18]. Specific values of this quantity for the relevant solutions examined herein can be found in the references cited.

Various explanations of this anomalous behavior were reviewed in the preceding paper [2.1]. Some of these explanations are of intermolecular and some are of intramolecular origins [2.5-11]. Definitive experimental evidence confirming the intermolecular nature of shear thickening was provided in 1992 by Kishbaugh and McHugh [2.2, 2.3, 2.14].

[1] All the tables and figure are located in the appendix at the end of the part.

Rheo-optical measurements of linear dichroism, linear birefringence, and shear viscosity indicated that shear thickening was definitely associated with some sort of supermolecular structure formation [2.2, 2.3, 2.14]. Typical experimental data from this study are illustrated in Figure 2.2. Note that almost concurrently with the critical shear rate, $\dot{\gamma}_c$, where the viscosity has a minimum, the linear dichroism displays a global maximum at $\dot{\gamma}_d$. The value of $\dot{\gamma}_d$ is usually equal to, or else slightly less than, the value of $\dot{\gamma}_c$. At the same time, the magnitude of the linear birefringence increases monotonically with increasing shear rate.

Vrahopoulou and McHugh [2.13] advanced a conceptual basis for explaining the shear-thickening behavior, and Kishbaugh and McHugh [2.2, 2.3, 2.14] extended it based upon the rheo-optical data summarized in these paragraphs and Figure 2.2. The main point of their explanation was that the solutions begin to develop micron-sized, optically-isotropic particles before the critical shear rate where the shear-thickening behavior begins to manifest, and that the continuous growth of these particles with increasing shear rate leads to the shear-thickening behavior evident in the viscosity curve.

There are some shortcomings to the explanation of shear thickening discussed above. First, it cannot explain why the onset of shear thickening always occurs at an equivalent or slightly larger value of shear rate than the maximum in dichroism curve [2.1]. Second there is contradiction between the increase in size of the particles and the monotonic increase of birefringence with increasing shear rate [2.1].

Edwards *et al.* [2.1] suggested a somewhat different explanation based on the Two Coupled Maxwell Modes (TCMM) Model [2.1, 2.15, 2.16]. In this explanation, at

very low shear rates, the solutions exhibit a Newtonian plateau in viscosity, which is due to the short-time dynamics of the individual polymer chains and intermolecular associations. As shear rate increases, this plateau gives way to shear-thinning behavior, which is brought on by the stretching and orienting of the individual chains and the intermolecular structures. As the shear rate increases, the chains and structures continue to elongate and orient, and the viscosity of the solution continues to drop. At the critical shear rate, the viscosity of the solution is no longer able to support the extension of the structures, and subsequently they decrease in extension for higher shear rates. Once they have resumed a spherical distribution, they no longer contribute to changes in the relative stress level, and shear thinning resumes as the individual chain distribution continues to extend. This maximum in the extension of the structures with respect to shear rate rationalizes why the maximum in the dichroism curve always corresponds to the minimum in the viscosity curve. Moreover these structures are not isotropic but anisotropic, and are composed of anisotropic polymer chains, thus rationalizing the monotonically increasing behavior of the birefringence with increasing shear rate. The TCMM Model also provided predictions for other rheological characteristic functions, such as the first and second normal-stress coefficients.

The experimental data of Refs. [2.2, 2.3, 2.12, 2.13, 2.18] are generally not accurate enough near the viscosity minima to determine whether or not these minima are associated with a specific value of the shear stress. If such exists, the TCMM Model will also support this conclusion through the parameterized fits of the experimental data. However, without sufficiently accurate experimental data, no conclusions on this issue can be derived from the TCMM Model.

In the TCMM Model there are five parameters: λ_1, λ_2, n_1, n_2, and θ. The first two are the constant relaxation times of the two modes, measured in units of time. The first mode corresponds to the free polymer chains remaining in solution, and the second to the supermolecular structures formed during shear. The second two parameters are the effective concentrations of the two modes, measured in units of moles per volume. The final (dimensionless) parameter, θ, represents the degree of interaction between the two modes. Edwards *et al.* [2.1] applied the TCMM Model to a sampling of the experimental shear-thickening data available in the literature, and used this to infer the physics behind this anomalous behavior, as described in the preceding paragraphs. A sensitivity analysis therein [2.1] revealed the extent of uncertainties in the fitted values of these parameters.

In this paper, we present a full parameterization of the TCMM Model to all known experimental data from the literature. This provides a more thorough understanding of the significance of the model parameters, as well as insight into how they vary with concentration, temperature, molecular weight, and polymer architecture. Comparison of experimental data and model predictions results in a clearer insight into the peculiar behavior of shear thickening in dilute polymer solutions.

2.2 Background

2.2.1 The Two Coupled Maxwell Modes Model

The TCMM Model is a special case of the Multiple Coupled Maxwell Modes Model, which was developed in Ref. [2.15]. In the TCMM Model, we use two conformation tensors, $\mathbf{c}^1(\mathbf{x},t)$ and $\mathbf{c}^2(\mathbf{x},t)$, to describe the orientation and extension of

the individual polymer chains in solution and the supermolecular associations [2.1]. The eigenvalues and eigenvectors of these second-rank tensors quantify the extension and orientation of the two corresponding modes**.** The first conformation tensor, $\mathbf{c}^1(\mathbf{x},t)$, is taken as the second moment of the distribution function, $\psi(\mathbf{x},\mathbf{R},t)$ [2.1, 2.4]:

$$\mathbf{c}^1 = \int \mathbf{RR}\ \psi\ d^3R \tag{2.1}$$

In this expression, $\mathbf{R}$ is the end-to-end vector of a dissolved polymer chain. The second conformation tensor, $\mathbf{c}^2(\mathbf{x},t)$, is associated with the intermolecular structures that form during shear, and is given by

$$\mathbf{c}^2 = \int \mathbf{aa}\ \ f\ d^3a \tag{2.2}$$

where $f(\mathbf{x},\mathbf{a},t)$ is the size distribution function of the structures and $\mathbf{a}$ is the vector spanning the major axis of an ellipsoidal structure [2.1].

In the TCMM Model, these conformation tensors are not only affected by the applied deformation, but by each other as well [2.1, 2.16]. Many rheological models of differential type have been developed using uncoupled modes, in which the individual mode tensors are affected by the applied deformation only [2.4]. The introduction of coupling among the various modes of relaxation led to a general class of coupled relaxation mode models derived in Ref. [2.15]. In the two-mode limit, the evolution equations for the conformation tensors are

$$\frac{\partial c^1_{\alpha\beta}}{\partial t} + v_\gamma \nabla_\gamma c^1_{\alpha\beta} - c^1_{\alpha\gamma}\nabla_\gamma v_\beta - c^1_{\beta_\gamma}\nabla_\gamma v_\alpha = -\frac{1}{\lambda_1} c^1_{\alpha\beta} + \frac{k_B T}{\lambda_1 K_1}\delta_{\alpha\beta}$$
$$-\frac{\theta}{2k_B T}\sqrt{\frac{n_2}{n_1}}\ \frac{1}{\sqrt{\lambda_1\lambda_2}}\left[K_2\left(c^1_{\alpha\gamma}c^2_{\beta_\gamma} + c^2_{\alpha\gamma}c^1_{\beta_\gamma}\right) - 2k_B T\ c^1_{\alpha\beta}\right]$$

$$\frac{\partial c^2_{\alpha\beta}}{\partial t} + v_\gamma \nabla_\gamma c^2_{\alpha\beta} - c^2_{\alpha\gamma}\nabla_\gamma v_\beta - c^2_{\beta\gamma}\nabla_\gamma v_\alpha = -\frac{1}{\lambda_2} c^2_{\alpha\beta} + \frac{k_B T}{\lambda_2 K_2}\delta_{\alpha\beta} - \frac{\theta}{2k_B T}\sqrt{\frac{n_2}{n_1}}\frac{1}{\sqrt{\lambda_1\lambda_2}}\left[K_1\left(c^2_{\alpha\gamma}c^1_{\beta\gamma} + c^1_{\alpha\gamma}c^2_{\beta\gamma}\right) - 2k_B T\, c^2_{\alpha\beta}\right] \tag{2.3}$$

In these expressions, k_B is Boltzmann's constant, T is the absolute temperature, and K_1, K_2 are the Hookean spring constants of each Maxwell mode. The parameters, λ_1, λ_2, n_1, and n_2 must be greater than or equal to zero for the model to make sense physically. The coupling parameter, θ, appears to be lie within the range [0, 1]; however, it is usually a small positive fraction [2.16]. Currently, there is no theory to provide values for these five parameters, and so they must be obtained from fits of the model to experimental data.

The extra stress tensor, $\sigma_{\alpha\beta}$, used for calculating the rheological properties of the polymer solutions, is a linear sum over the two conformation tensors,

$$\sigma_{\alpha\beta} = \sum_{i=1}^{2}\left(n_i N_A K_i c^i_{\alpha\beta} - n_i N_A k_B T \delta_{\alpha\beta}\right) \tag{2.4}$$

where N_A is Avogadro's number. Using this expression, the rheological characteristic functions, such as the shear viscosity and normal stress coefficients, can be calculated in the usual fashion [2.4]. Note that Eq. (2.3) is easier to solve in dimensionless form [2.1], using dimensionless conformation tensors, $\tilde{\mathbf{c}}^i = K_i \mathbf{c}^i / k_B T$.

2.2.2 Dichroism

Linear dichroism is the difference in intensity of linearly polarized light parallel and perpendicular to an axis of orientation [2.17]. This optical property is often used to get information on the size and shape of micro-structural entities. The linear dichroism in

our system is due to two sources: Rayleigh scattering from the structures and the innate dichroism of the individual molecules [2.1, 2.14]. Consequently, the dichroism is expressed as $\Delta n'' = \Delta n_1'' + \Delta n_2''$, where

$$\Delta n_1'' = \frac{4\pi}{5} k^3 \frac{cN_A m_s}{M} (\alpha_1^2 - \alpha_2^2)_1 [\mathrm{tr}\,\tilde{\mathbf{c}}^1 - 3] \tag{2.5}$$

and

$$\Delta n_2'' = \frac{8\pi}{15} m_p n_2 N_A k^3 (\alpha_1^2 - \alpha_2^2)_2 \frac{b}{(1 + 36/\sigma^2)} \tag{2.6}$$

The first term, expressed by Eq. (2.5), is the innate dichroism of the deformed polymer chains. The symbols appearing in this equation are the wave number, $k = 2\pi/(6.328\times10^{-7}\,\mathrm{m})$, the polymer concentration, c, the polymer molecular weight, M, the refractive index of the solvent, $m_s = 1.474$, and the polarizability difference, $(\alpha_1^2 - \alpha_2^2)_1 = -1.25\times10^{-42}\,\mathrm{cm}^6$/molecule [2.2, 2.14]. (Note that dichroism data exists only for the Polystyrene/decalin system, as described below.)

The second term, expressed by Eq. (2.6), is the linear dichroism of the supermolecular structures according to the Rayleigh Scattering Theory [2.1, 2.2, 2.14]. The symbols appearing in this expression are the refractive index of the polymer, $m_p = 1.59$, and several other functions. The anisotropy function, b, is given by

$$b = \frac{p^2 - 1}{p^2 + 1} \tag{2.7}$$

where p is the sphericity or shape of the structure [2.1]:

$$p = (1 + \frac{3}{2}[\mathrm{tr}\,\tilde{\mathbf{c}}^2 - 3])^{3/4} \tag{2.8}$$

The quantity σ is a dimensionless shear rate relative to the size and shape of the assumed structures [2.2, 2.14]:

$$\sigma = \frac{\eta_s V_p \nu(p)}{k_b T}\dot{\gamma} \tag{2.9}$$

where V_p is the volume of the structure [2.1],

$$V_p = \frac{4\pi}{3p^2}a^3 = \frac{4\pi}{3p^2}([\mathrm{tr}\,\tilde{\mathbf{c}}^2 - 3]\langle \mathbf{aa}\rangle_0)^{3/2} \tag{2.10}$$

and

$$\frac{1}{\nu(p)} = \frac{p^2}{p^4+1}\left[-1 + \frac{2p^2-1}{2p\sqrt{p^2-1}}\ln\left[\frac{p+\sqrt{p^2-1}}{p-\sqrt{p^2-1}}\right]\right] \tag{2.11}$$

In Eq. (2.10), $\langle \mathbf{aa}\rangle_0$ is a parameter fitted to the dichroism curve by matching the maximum value of $\Delta n''$ at the shear rate $\dot{\gamma}_d$. After the parameter fitting has been completed, the effective structure size (length of major axis), a, can be determined by taking the square root of the primary eigenvalues of $\tilde{\mathbf{c}}^2$ multiplied by the factor $\langle \mathbf{aa}\rangle_0$: $a = \sqrt{(\lambda_p - 1)\langle \mathbf{aa}\rangle_0}$. The polarizability difference of the structures, $(\alpha_1^2 - \alpha_2^2)_2$, is given by

$$\frac{16\pi^2}{V_p^2}(\alpha_1^2 - \alpha_2^2)_2 = \left[\frac{1}{L_1 + 1/(m_1^2-1)}\right]^2 - \left[\frac{1}{(L_1-1)/2 + 1/(m_1^2-1)}\right]^2 \tag{2.12}$$

where

$$L_1 = \frac{1-e^2}{e^2}\left[-1 + \frac{1}{2e}\ln\left[\frac{1+e}{1-e}\right]\right]^2 \tag{2.13}$$

and

$$e^2 = \left[1 - \frac{1}{p^2}\right] \tag{2.14}$$

Using these equations, the linear dichroism and its orientation angle relative to the direction of flow can be calculated after solving the TCMM Model for the non-vanishing components of $\tilde{\mathbf{c}}^1$ and $\tilde{\mathbf{c}}^2$.

2.3 Experiment

2.3.1 Data Acquisition

The data that we used to obtain parameters for the TCMM Model was taken from Refs. [2.2, 2.3, 2.12, 2.13, 2.18]. Layec-Raphalen and Wolff [2.12] measured viscosity as a function of shear rate for dilute solutions of Polystyrene/decalin (PS/d) of five different average molecular weights. Relative viscosities were measured by a capillary viscometer. They studied shear thickening for dilute solutions of PS/d as a function of concentration, molecular weight, and shear rate, which yielded a quantitative analysis of the dependence of shear thickening on these variables [2.12].

Vrahopoulou and McHugh studied shear thickening for three different polymer/solvent systems: Polyethylene/xylene (PE/x), Polypropylene/tetralin (PP/t), and Polyethylene oxide/ethanol (PEO/e). They measured the viscosities of several crystallizable polymer solutions as functions of the wall shear rate in a capillary viscometer.

Kishbaugh and McHugh [2.2, 2.3] obtained the most detailed experimental data on shear thickening by measuring not only the shear viscosity, but also the linear birefringence and linear dichroism and their associated orientation angles. A Couette

flow cell was used in these simultaneous rheo-optical experiments to study the PS/d system.

The critical shear rate, $\dot{\gamma}_c$, where the minimum in the viscosity occurs, is a very important quantity for understanding shear thickening. From the available experimental data, we generated plots of the dependence of the critical shear rate as a function of polymer concentration, temperature, and molecular weight. Results are presented in Figures 2.3, 2.4, and 2.5.

Figure 2.3 depicts $\dot{\gamma}_c$ for PE/x solutions as a function of temperature for three concentrations. We observe that the critical shear rate increases with increasing temperature for all concentrations. We can rationalize this behavior in terms of a physical mechanism: as the temperature increases, the viscosity of a liquid typically decreases. With the lower viscosity, the shear thickening behavior is naturally postponed until higher shear rates are applied. One can also explain the increase in critical shear rate with increasing temperature by considering the temperature dependence of the relaxation time, λ. From experiments, we know that relaxation times decrease as the temperature increases. If we assume that $H_c = \lambda\dot{\gamma}_c$ is a dimensionless constant at the critical shear rate at the different temperatures, then the critical shear rate, $\dot{\gamma}_c$, increases as relaxation time, λ, decreases. Since the viscosity minimum is associated with the physics of supermolecular structuring, it is evident that an increase in temperature acts to reduce the degree of structuring by increasing the kinetic energy of the polymer chain segments. In order to offset this reduction, a larger deformation rate is required.

Also in Figure 2.3, we observe that the critical shear rate decreases with increasing polymer concentration. We can explain this relationship by considering that, as the polymer concentration increases, the effect of the polymer is magnified. In a previous article [2.1], we provided evidence that shear-thickening behavior is due to the decrease in size and anisotropy of associations of polymer particles in the solvent. The sizes of these polymer structures presumably increase with polymer concentration. Consequently, it is plausible that the rate of size decrease also accelerates with polymer concentration, and so the minimum shear rate required for this size decrease to manifest itself is correspondingly smaller. Furthermore, since λ increases with polymer concentration, a smaller value of $\dot{\gamma}_c$ is required to attain the critical value of H_c.

In Figure 2.4, we plot $\dot{\gamma}_c$ of PS/d solutions as a function of polymer concentration for five different molecular weights. Figure 2.4 supports the conclusion taken from Figure 2.3 that, as polymer concentration is increased, the critical shear rate decreases for all molecular weights. The scatter in the data is generated from two sources of error: primarily, experimental error from the original work [2.12] and, to a lesser extent, error due to the computer software used to acquire the numerical values from the published plots.

Additionally in Figure 2.4, we see that the critical shear rate generally decreases with increasing molecular weight. At the two highest values of molecular weight, we see a partial violation of this explanation of molecular weight dependence. We can explain this violation by postulating that at very high molecular weights, we reach a plateau where the critical shear rate is no longer a function of molecular weight. Such a plateau exists because the effect of increasing chain length will become weaker when the

molecular weight is already very high. Additionally the distribution of molecular weight will influence the effect of the molecular weight on critical shear rate. However, we do not know the distribution of molecular weight for these polymers and cannot evaluate this effect. Furthermore, since λ generally increases with molecular weight, again the dimensionless quantity H_c describes well the qualitative solution behavior.

In Figure 2.5, we plot the critical shear rates of PE/x solutions as functions of temperature for two molecular weights. Figure 2.5 supports the conclusion from Figure 2.4 that the critical shear rate decreases with increasing molecular weight and the conclusion from Figure 2.3 that the critical shear rate increases with increasing temperature for all concentrations. However, for the lower molecular weight value, $\dot{\gamma}_c$ decreases slightly with increasing temperature. We suspect that this slight, anomalous trend is within the experimental error of the data.

2.3.2 Data Fitting Methodology

The method we used to optimize our parameters λ_1, λ_2, n_1, n_2, and θ in the TCMM Model was Nelder and Mead's Downhill Simplex Method [2.19], which requires only functional evaluations, not derivative evaluations. While this method is not very efficient in terms of the number of functional evaluations it requires, the simplex method can always find a minimum, provided that one exists. However, the simplex method is not guaranteed to find a global minimum. On the contrary, the minimum found is strongly dependent on the initial guess of the problem. To compensate for this shortcoming, we scattered our initial guesses in the five-dimensional parameter space to find the deepest minimum. If we are dealing with a series of data sets where, for example,

only molecular weight is varied, then we used the scatter technique to find the minimum for the first data set. For each subsequent data set in the series, we used the optimized parameter set from the previous data set in the series as the initial guess.

Within the simplex method, the evolution equations for the conformation tensors, Eq. (2.3), were solved using an iterative Newton-Raphson Method for the current set of parameter values. The extra stress tensor expression, Eq. (2.4), was then evaluated, and the shear viscosity calculated. This gave rise to an objective function, defined below, which the simplex method tried to minimize.

Because we were interested in modeling the shear-thickening phenomenon, we fitted our parameters primarily to experimental data in the shear-thickening range of shear rates. This range is bounded by $\dot{\gamma}_c$ and $\dot{\gamma}_m$ (see Figure 2.1). We used the following expression for our objective function, F_{obj}^{η}, which is the function minimized by the simplex method:

$$F_{obj}^{\eta} = \left[\frac{\sum_{i=1}^{n_{data}^{\eta}} w_i \left(\frac{\eta_i^e - \eta_i^m}{\eta_i^e} \right)^2 + w(\eta(\dot{\gamma}_c)) \left(\frac{\eta(\dot{\gamma}_c)^e - \eta(\dot{\gamma}_c)^m}{\eta(\dot{\gamma}_c)^e} \right)^2 + w(\dot{\gamma}_c) \left(\frac{\dot{\gamma}_c^e - \dot{\gamma}_c^m}{\dot{\gamma}_c^e} \right)^2}{n_{data}^{\eta} + 2} \right]^{\frac{1}{2}} \quad (2.15)$$

where $w(\eta(\dot{\gamma}_c))$ is the weighting factor for the value of the viscosity at the critical shear rate, $w(\dot{\gamma}_c)$ is the weighting factor for the value of $\dot{\gamma}_c$, n_{data}^{η} is the number of experimental viscosity data points, η_i^e is the *i*-th experimental viscosity data point, and η_i^m is the corresponding value as calculated with the TCMM Model. We set $w(\eta(\dot{\gamma})_c)$

and $w(\dot{\gamma}_c)$ equal to 100 in order to be sure that we fit the experimental value of the viscosity well at $\dot{\gamma}_c$. The weighting factor for all other data points was given by

$$w_i = \begin{cases} 0 & \dot{\gamma} < \dot{\gamma}_c^e \\ 1 & \dot{\gamma}_c^e < \dot{\gamma} < \dot{\gamma}_m^e \\ 0 & \dot{\gamma} > \dot{\gamma}_m^e \end{cases} \tag{2.16}$$

In some cases, we had available experimental data for the dichroism. When this was the case, we slightly altered the optimization procedure, described above, by adding a sixth fitting parameter, $\langle \mathbf{aa} \rangle_0$, which characterized the size of the super-molecular structures. (This parameter appears in the expression for the linear dichroism, Eq. (6).) The same numerical methods were used to optimize all six parameters; however, a new objective function was needed for the dichroism data:

$$F_{obj}^d = \left[\frac{\sum_{i=1}^{n_{data}^d} w_i \left(\frac{\Delta n_i''^e - \Delta n_i''^m}{\Delta n_{\max}''^e} \right)^2}{n_{data}^d} \right]^{\frac{1}{2}} \tag{2.17}$$

where $w_i = 1$ is the weighting factor for the dichroism, $\Delta n_i''^e$ is the experimental dichroism data taken from the literature [2.2, 2.3], $\Delta n_i''^m$ is the value computed by the TCCM Model, and $\Delta n_{\max}''^e$ is the experimental value of the dichroism at $\dot{\gamma}_d$.

We used two different methods to optimize the six parameters, λ_1, λ_2, n_1, n_2, θ, and $\langle \mathbf{aa} \rangle_0$, for the cases where dichroism data were available. One method was to use the optimized values for the five parameters λ_1, λ_2, n_1, n_2, and θ using only the viscosity data and subsequently optimizing to the dichroism data varying only the sixth parameter.

The second method was to optimize all six parameters simultaneously to a new objective function: $F_{obj} = F_{obj}^{\eta} + F_{obj}^{d}$. We compare the two methods of optimization in the following section.

2.4 Results and discussion

Three different experimental studies provided the data for our comparisons. These were the capillary viscometric examinations of Layec-Raphalen and Wolff [2.12] and Vrahopoulou and McHugh [2.13, 2.18], and the Couette rheo-optical experiments of Kishbaugh and McHugh [2.2, 2.3]. All experimental data presented in the above sources was parameterized using the TCMM Model. Parameter values for a sampling of these experiments are presented in Tables 2.1 and 2.2, as well as in the following figures.

2.4.1 Comparison of the General Trends of the Theoretical and Experimental Results

In Figure 2.6, we show some typical optimized fits of the TCMM Model for PE/x solutions ($M = 2.90 \times 10^6$ g/mole, $c = 0.05$ wt%) with the experimental data of Vrahopoulou and McHugh [2.13, 2.18]. The TCCM Model faithfully demonstrates the critical features of the experimental data. At a given temperature, both the model and experimental reduced viscosity display a minimum (at $\dot{\gamma}_c$) and a maximum (near $\dot{\gamma}_m$) with respect to shear rate. Moreover, the TCMM Model also quantifies the temperature dependence of the viscosity correctly. The viscosity decreases with increasing temperature at any particular shear rate, and the minima of the viscosity curves occur at increasing values of $\dot{\gamma}_c$ as the temperature increases. Therefore, the overall performance

of the TCMM Model is quite satisfactory, especially in the shear-thickening range of shear rates where the parameter fitting was concentrated.

The TCMM Model has several typical discrepancies with the experimental data. First, at low shear rates, the TCMM Model always overpredicts the viscosity. Second, after the value of the shear rate where the maximum viscosity is observed, $\dot{\gamma}_m$, the TCMM Model does not predict as steep a drop in the viscosity as is observed experimentally. We could improve the fit in these two shear-rate regions by incorporating more complicated features into the model, such as shear-rate dependent relaxation times. However, these additional features would provide only quantitative improvement in shear-rate regions outside of the main region of interest at the cost of requiring additional parameters and without necessarily providing any new, relevant physical information.

2.4.2 The Dependence of λ_1 on Temperature, Concentration, and Molecular Weight

In Figure 2.7, we plot the relaxation time of the chain conformation mode, λ_1, as a function of temperature for five PE/x solutions of different molecular weights and concentrations. We see that λ_1 decreases with increasing temperature for all of the cases. As the temperature increases, the kinetic motion of the individual atoms increases, which makes polymer chain conformational rearrangements easier.

Also in Figure 2.7, we observe that, at constant temperature and molecular weight (2.90×10^6 g/mole), there appears to be a non-monotonic dependence between λ_1 and polymer concentration. Figure 2.8 contains additional information about the functional

dependence of this relaxation time on polymer concentration. In this figure, we plot the relaxation time as a function of concentration for five different molecular weights of PS/d solutions at 25°C. The relaxation time generally increases with increasing concentration for the constant molecular weight, but it seems to arrive at a plateau when the polymer concentration reaches 0.25 g/dl. We can explain the increase in λ_1 at low concentrations by considering that, as the polymer concentration increases, the extent of intermolecular interactions increases, thus making it more difficult for the polymer chains to relax. We also observe a plateau at higher polymer concentrations, which is possibly caused by the increased number of polymer chains that take part in the supermolecular structuring: larger and more numerous structures require more polymer chains, thus decreasing the number of free polymer chains remaining in solution.

We can also consider the dependence of λ_1 on molecular weight at constant temperature and polymer concentration. Figure 2.8 shows that λ_1 generally increases with increasing molecular weight for the same temperature and polymer concentration. As the average length of the polymer chain increases, the more difficult it is for the molecule to relax. Therefore, the increase in relaxation time with increasing molecular weight is expected. However, at the highest molecular weights, there are exceptions to this trend. This anomalous dependence at high molecular weights is also observed in the values of the critical shear rates obtained from the experimental data--see Figure 2.4. In all likelihood, at some point further increases in molecular weight probably have negligible effect upon the phenomenon under consideration.

2.4.3 The Dependence of λ_2 on Temperature, Concentration, and Molecular Weight

In Figure 2.9, we plot the relaxation time of the structure conformation mode, λ_2, as a function of temperature for five cases of PE/x solutions of different molecular weights and concentrations. We see that λ_2 decreases with increasing temperature for most cases. This trend is similar to the λ_1 temperature trend for the same reason; namely, that the supermolecular structures relax more easily at higher temperatures.

Also in Figure 2.9, we observe, at constant temperature and molecular weight (2.90×10^6 g/mole), an increase in λ_2 with polymer concentration, in contrast to the behavior of λ_1, which showed a maximum. In Figure 2.10, we plot λ_2 as a function of concentration for five different molecular weights of PS/d solutions at 25°C. We see that this relaxation time increases when concentration is lower than about 0.05 g/dl, then decreases with increasing concentration until it reaches a plateau at about 0.25 g/dl. To rationalize such behavior, one must resort to evidence from the previous article [2.1]: the size of the structures does not necessarily scale with concentration. It is quite possible that the structures are fewer and larger at lower concentrations and smaller yet more numerous at higher concentrations.

We can also consider the dependence of λ_2 on molecular weight at constant temperature and polymer concentration. In Figure 2.9, we see that λ_2 increases with molecular weight. Figure 2.10 shows the same general trend, except at the highest molecular weight, as was the case with λ_1. This probably occurs for the same reason; namely, that it is more difficult for the longer polymer chains, which make up the supermolecular structures, to relax.

2.4.4 The Dependence of n_1 on Temperature, Concentration, and Molecular Weight

In Figure 2.11, we plot the effective concentration of the chain conformation mode, n_1, as a function of temperature for five cases of PE/x solutions of different molecular weights and concentrations. Figure 2.11 shows that n_1 is generally insensitive to temperature changes between 110°C and 125°C. The average percentage change in n_1 with temperature is less than 10%. We expect little change in n_1 with temperature, as temperature should not have any effect on the amount of mass in the solutions. However, it does have a slight effect for concentrations that are measured in wt% since the solvent density depends on temperature: as the temperature increases, the solvent density decreases, and thus the effective mass of polymer in a unit volume of solvent decreases as well. These variations are generally within about 10%.

In Figure 2.12, we plot the effective concentration of the chain mode as a function of concentration for five different molecular weights of PS/d solutions at $25°C$. This figure demonstrates that n_1 generally increases with increasing concentration at constant molecular weight, as expected: the increasing polymer concentration certainly increases the effective concentration of the free chains in solution.

We can also consider the dependence of n_1 on molecular weight at constant temperature and polymer concentration. Results here are inconclusive. This can probably be ascribed to experimental data scatter and uncertainty in the five-parameter optimization.

2.4.5 The Dependence of n_2 on Temperature, Concentration, and Molecular Weight

Figure 2.13 plots the effective concentration of the structure mode, n_2, as a function of temperature for five cases of PE/x solutions of different molecular weights and concentrations. Figure 2.13 demonstrates that n_2 is also generally insensitive to temperature changes between 110°C and 125°C.

In Figure 2.14, we plot n_2 as a function of concentration for five different molecular weights of PS/d at $25°C$. We observe the general trend that n_2 decreases with increasing polymer concentration. Such an observation is consistent with the results of Ref. [2.1], wherein it was noted that structure size increased with increasing polymer concentration. However, as the structure size increased, the number of structures decreased. Hence, n_2 decreased with increasing polymer concentration.

Figure 2.14 also demonstrates that n_2 generally decreases with increasing molecular weight for the same polymer concentration. The rationale for this trend is as above: increasing the molecular weight produces larger, but fewer, structures.

2.4.6 The Dependence of θ on Temperature, Concentration, and Molecular Weight

In Figure 2.15, we plot the coupling parameter, θ, as a function of temperature for five samples of PE/x solutions of different molecular weights and concentrations. This figure shows that θ is generally insensitive to temperature changes, as was shown previously [2.1].

In Figure 2.16, we plot the coupling parameter as a function of concentration for five different molecular weight samples of PS/d solutions at $25°C$. This figure shows

that θ is essentially independent of concentration at lower concentrations, but that it generally increases with increasing concentration at higher concentrations. In order to rationalize this behavior, we consider that n_1 generally increases with increasing concentration and that n_2 generally decreases. The coupling parameter is most likely a function of both n_1 and n_2; a molecular model corresponding to the macroscopic TCMM Model might reveal an exact functional dependency.

We can also consider the dependence of θ on molecular weight at constant temperature and polymer concentration. Figure 2.15 shows that θ increase with increasing molecular weight. Figure 2.16 also shows that θ generally increases with increasing molecular weight for the same polymer concentration. As the polymer chains become longer with increasing molecular weight, it seems reasonable that a greater degree of interaction between the modes would develop. Note that, in all cases, the coupling parameter is a small, positive fraction, which is consistent with previous examinations of the TCMM Model [2.16].

2.4.7 Inclusion of the Dichroism Data in the Parameter Fitting

For some of the experimental runs, we have available measurements of both the shear viscosity and the dichroism at steady state. As noted before, the dichroism calculation with the TCMM Model requires one additional parameter beyond the five needed for fitting the viscosity data only. We optimized the additional data using two methods, as described in the preceding section. In Method 5+1, we optimized the first five parameters to the viscosity data only. Then, holding these parameters constant, we

optimized the sixth parameter, $\langle \mathbf{aa} \rangle_0$, individually to the dichroism data. In Method 6, we simultaneously optimized all six parameters to the combined objective function, $F_{obj} = F_{obj}^{\eta} + F_{obj}^{d}$, incorporating both viscosity and dichroism data.

In Figure 2.17, we plot the viscosity and dichroism as functions of the shear rate for a PS/d solution (6.8×10^6 g/mole, $T = 25°C$, and $c = 0.25$ g/dl). As in Figure 2.2, we observe a maximum in the dichroism curve that occurs shortly before the minimum in the viscosity curve. Figure 2.17 demonstrates that the TCMM Model can fit the experimental data for viscosity and dichroism simultaneously, and that similar results can be obtained using either of the two different methods of optimization. Consequently, a sufficiently good fit of the TCMM Model to experimental data requires only viscosity data. Very little improvement, if any, is obtained by optimizing to additional dichroism data. We should also point out that, if we ignore the viscosity data and fit all six parameters to the dichroism data only, then we can fit the experimental dichroism data well but the viscosity fittings are qualitatively and quantitatively incorrect. Thus dichroism data alone is insufficient to obtain a decent fit of the TCMM Model.

In Figure 2.18, we show the behavior of the parameter $\langle \mathbf{aa} \rangle_0$ as a function of polymer concentration for the solutions where dichroism data was available. The variations of this structure-size parameter with concentration are in both directions; in general, it varies inversely with the number of structures formed in the solutions. It appears that $\langle \mathbf{aa} \rangle_0$ does not depend greatly on molecular weight, indicating that the typical structure size does not vary much from one polymer sample to another.

2.5 Conclusion

In this work, we have fit the TCMM Model to experimental data for viscosity and dichroism during steady-state shear flow. The TCMM Model can account for the qualitative features of both the viscosity and dichroism data. We fit the six parameters (two relaxation times, two modal concentrations, a coupling parameter, and a particle size parameter) of the TCMM Model in order to obtain quantitative agreement with the experimental data.

From this fitting procedure, we were able to establish the functional dependence of the relaxation times, modal concentrations, coupling parameter, and the particle size parameter as functions of temperature, polymer concentration, and polymer molecular weight, using the physical basis of the TCMM Model. We showed that, by optimizing to only the viscosity data, we were able to obtain the same relaxation times, modal concentrations, and coupling parameter as when optimizing to both the viscosity and dichroism data simultaneously. This is useful because, typically, the dichroism data is not available.

Thus the TCMM Model seems to give an adequate quantitative description of the shear-thickening phenomenon, and to offer new insight into the physics of structure formation in dilute polymer solutions, as first discussed in Ref. [2.1]. Further validation of the model may be obtained by examining transient experimental data taken during start up and cessation of shear flow [2.20].

Acknowledgements

The authors would like to acknowledge graduate student support from the Department of Chemical Engineering at the University of Tennessee. Additionally, the authors would like to thank P.A. Kamerkar and C.W. Reneau for their insightful discussions during the preparation of this manuscript.

References

2.1. B.J. Edwards, D.J. Keffer, and C.W. Reneau, *J. of Appl. Polym. Sci.*, **85**, 1714 (2002).

2.2. A. J. Kishbaugh, Ph.D. Dissertation, University of Illinois, 1992.

2.3. A. J. Kishbaugh and A.J. McHugh, *Rheol. Acta*, **32**, 9 (1993).

2.4. R.B. Bird, C.F. Curtiss, R.C. Armstrong, and O. Hassager, *Dynamics of Polymeric Fluids, Vols. 1 and 2, Sec. Ed.*, John Wiley and Sons, New York, 1987.

2.5. A. Peterlin, *J. Chem. Phys.*, **33**, 1799 (1960).

2.6. A. Peterlin, *Makromol. Chem.*, **45**, 338 (1961).

2.7. A. J. Kishbaugh and A. J. McHugh, *J. Non-Newtonian Fluid Mech.*, **34**, 181 (1990).

2.8. C. Wolff, A. Silberberg, Z. Priel, and M. N. Layec-Raphalen, *Polymer*, **20**, 281 (1979).

2.9. C. Wolff, *Adv. Colloid Interface Sci.*, **17**, 263 (1982).

2.10.E.P. Vrahopoulou and A.J. McHugh, *J. Rheol.*, 31, 371 (1987).

2.11. E.P. Vrahopoulou and A.J. McHugh, *Chem. Eng. Commun.*, **57**, 289 (1987)

2.12. M. Layec-Raphalen and C. Wolff, *J. Non-Newtonian Fluid Mech.*, **1**, 159 (1976).

2.13. E.P. Vrahopoulou and A.J. McHugh, *J. Non-Newtonian Fluid Mech.*, **25**, 157 (1987).

2.14. A.J. Kishbaugh and A.J. McHugh, *Rheol. Acta*, **32**, 115 (1993).

2.15. A.N. Beris and B.J. Edwards, *Thermodynamics of Flowing Systems*, Oxford University Press, New York, 1994.

2.16. B.J. Edwards, A.N. Beris, and V.G. Mavrantzas, *J. Rheol.*, **40**, 917 (1996).

2.17 A. Rodger and B. Nordėnd, *Circular Dichroism and Linear Dichroism*, Oxford University Press, 1997.

2.18 E. P. Vrahopoulou, Ph.D. Dissertation, University of Illinois, 1986.

2.19. W.H. Press, W.T. Vettuling, S.A. Tevkolsky, and B.P. Flannery, *Numerical Recipes in Fortran 77*, Cambridge University Press, Cambridge, 1992.

2.20. A. Kamerkar, B.J. Edwards, D.J. Keffer, and C.W. Reneau, *Chem. Eng. Commun.*, 192, 89-107 (2005)

Appendix

Tables

Table 2.1: Optimized parameters for the PE/x solutions of Vrahopoulou and McHugh [2.13, 2.18].

M	T	c	λ_1	λ_2	n_1	n_2	θ
g/mole	°C	wt %	s	s	mole/m^3	mole/m^3	-
2.90x10^6	110	0.0075	2.87E-03	7.41E-02	3.93E-05	1.74E-05	2.99E-03
2.90x10^6	120	0.0075	2.62E-03	6.88E-02	3.85E-05	1.73E-05	3.04E-03
2.90x10^6	125	0.0075	2.38E-03	7.60E-02	4.00E-05	1.85E-05	3.30E-03
1.6x10^5	110	0.01	1.52E-03	3.07E-02	6.62E-05	3.00E-05	1.84E-03
1.6x10^5	125	0.01	1.36E-03	3.09E-02	6.30E-05	2.88E-05	2.08E-03
6.0x10^5	110	0.01	2.56E-03	6.70E-02	4.00E-05	1.94E-05	2.90E-03
6.0x10^5	125	0.01	1.77E-03	5.72E-02	4.90E-05	2.36E-05	3.27E-03
2.90x10^6	115	0.005	2.67E-03	8.03E-02	3.76E-05	1.80E-05	2.95E-03
2.90x10^6	120	0.005	2.38E-03	7.01E-02	3.99E-05	1.88E-05	3.27E-03
2.90x10^6	125	0.005	2.23E-03	7.14E-02	4.04E-05	1.92E-05	3.40E-03
2.90x10^6	110	0.01	1.97E-03	8.87E-02	5.86E-05	2.84E-05	1.26E-02
2.90x10^6	115	0.01	1.81E-03	8.67E-02	6.00E-05	2.94E-05	1.11E-02
2.90x10^6	120	0.01	1.75E-03	8.42E-02	5.88E-05	2.90E-05	1.07E-02
2.90x10^6	125	0.01	1.72E-03	8.02E-02	5.68E-05	2.82E-05	1.07E-02

Table 2.2: Optimized parameters for the PS/d solutions of Layec-Raphalen and Wolff [2.12].

M	c	λ_1	λ_2	n_1	n_2	θ
g/mole	g/dl	s	s	mole/m^3	mole/m^3	-
8.40 x10^6	0.167	1.28E-02	4.17E-02	1.95E-04	2.00E-06	2.82E-03
8.40 x10^6	0.110	8.82E-03	2.91E-02	2.49E-04	3.82E-06	2.40E-03
8.40 x10^6	0.0889	1.16E-02	6.25E-02	1.41E-04	2.76E-05	2.58E-04
8.40 x10^6	0.0675	1.18E-02	6.14E-02	1.33E-04	2.60E-05	2.58E-04
8.40 x10^6	0.0557	1.07E-02	5.85E-02	1.39E-04	3.05E-05	2.59E-04
8.40 x10^6	0.0446	1.07E-02	6.02E-02	1.33E-04	3.17E-05	1.73E-04
8.40 x10^6	0.0326	1.07E-02	6.03E-02	1.29E-04	3.25E-05	1.78E-04
8.40 x10^6	0.0245	8.04E-03	4.56E-02	1.68E-04	4.29E-05	2.70E-04
7.32 x10^6	0.129	1.63E-02	1.25E-01	9.74E-05	2.76E-05	2.52E-04
7.32 x10^6	0.109	1.47E-02	1.47E-01	9.72E-05	3.19E-05	1.74E-04
7.32 x10^6	0.091	1.12E-02	1.39E-01	1.19E-04	4.26E-05	1.84E-04
7.32 x10^6	0.0642	1.20E-02	9.24E-02	1.15E-04	3.33E-05	1.68E-04
7.32 x10^6	0.0505	4.84E-03	4.48E-01	2.16E-04	1.07E-04	2.35E-04
7.32 x10^6	0.0428	4.83E-03	4.54E-01	2.12E-04	1.09E-04	3.28E-04
7.32 x10^6	0.0326	4.41E-03	2.90E-01	2.28E-04	1.17E-04	2.82E-04
7.32 x10^6	0.0251	4.69E-03	2.62E-01	2.11E-04	1.10E-04	3.83E-04
7.32 x10^6	0.0192	4.78E-03	1.89E-01	2.07E-04	1.06E-04	3.40E-04
3.70 x10^6	0.2450	9.72E-03	2.93E-02	2.89E-04	2.34E-06	2.12E-03
3.70 x10^6	0.195	8.07E-03	2.49E-02	3.09E-04	2.82E-06	3.27E-03
3.70 x10^6	0.149	1.07E-02	5.97E-02	1.59E-04	3.82E-05	9.26E-05
3.70 x10^6	0.108	9.48E-03	4.89E-02	1.72E-04	3.68E-05	1.25E-04
3.70 x10^6	0.0831	6.10E-03	4.54E-02	2.24E-04	7.34E-05	1.30E-04
3.70 x10^6	0.0653	5.89E-03	6.43E-02	2.06E-04	8.28E-05	1.10E-04
3.70 x10^6	0.0472	3.73E-03	1.01E-01	2.82E-04	1.40E-04	1.50E-04
3.37 x10^6	0.297	5.71E-03	1.75E-02	4.80E-04	4.61E-06	3.37E-03
3.37 x10^6	0.235	5.68E-03	1.77E-02	4.38E-04	5.75E-06	2.74E-03
3.37 x10^6	0.177	4.21E-03	1.31E-02	5.39E-04	6.38E-06	2.88E-03
3.37 x10^6	0.132	3.23E-03	9.86E-03	7.06E-04	4.91E-06	3.97E-03
3.37 x10^6	0.0888	6.35E-03	4.54E-02	2.13E-04	6.78E-05	1.29E-04
3.37 x10^6	0.0514	3.27E-03	7.76E-02	3.22E-04	1.57E-04	1.42E-04
3.37 x10^6	0.0448	2.84E-03	7.71E-02	3.63E-04	1.80E-04	1.23E-04
2.74 x10^6	0.401	4.90E-03	1.48E-02	6.24E-04	1.18E-06	3.54E-03
2.74 x10^6	0.241	5.24E-03	1.57E-02	4.74E-04	1.13E-06	1.90E-03
2.74 x10^6	0.197	4.32E-03	1.30E-02	5.41E-04	1.67E-06	1.67E-03
2.74 x10^6	0.161	4.29E-03	1.29E-02	5.18E-04	1.98E-06	1.50E-03

Figures

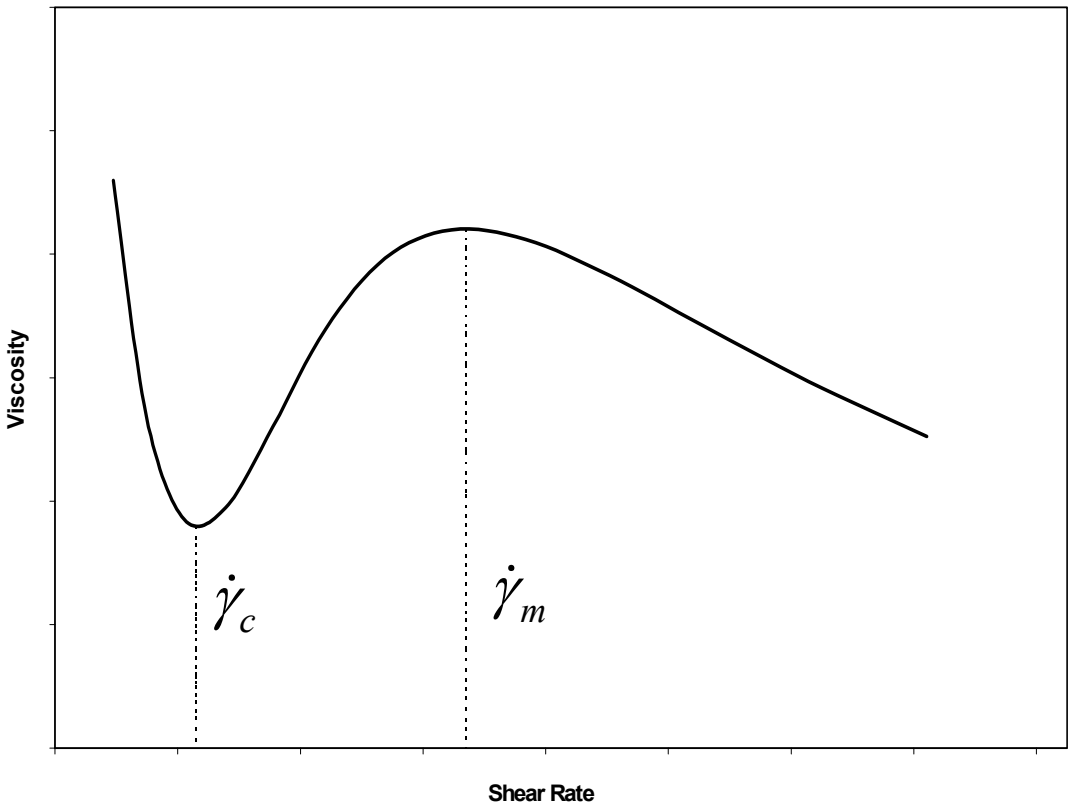

Figure 2.1: A typical plot of viscosity versus shear rate for a dilute polymer solution that exhibits shear thickening. The increase in viscosity begins at the critical shear rate, $\dot{\gamma}_c$, and shear thinning resumes at $\dot{\gamma}_m$.

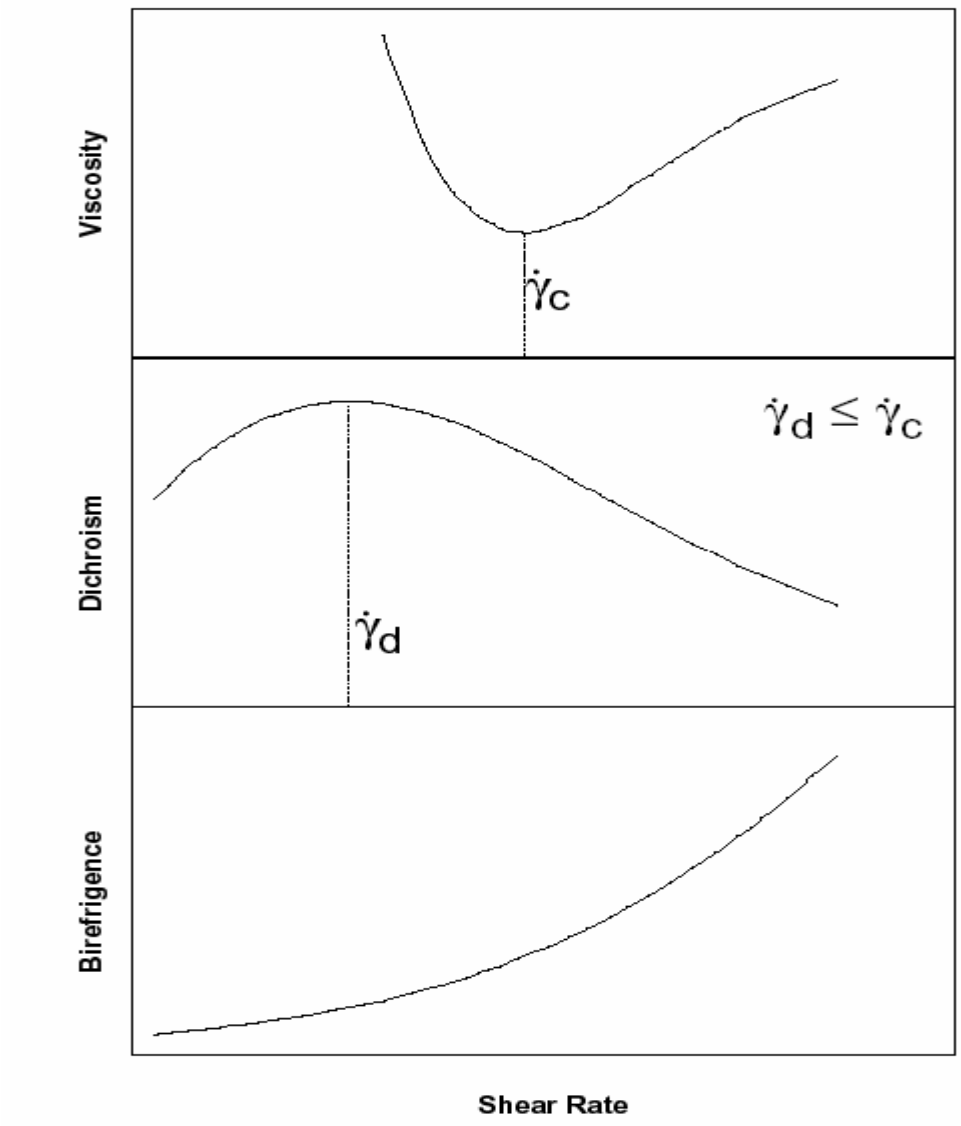

Figure 2.2: Typical flow curves for viscosity, dichroism, and negative birefringence versus shear rate as observed in simultaneous rheo-optical measurements.

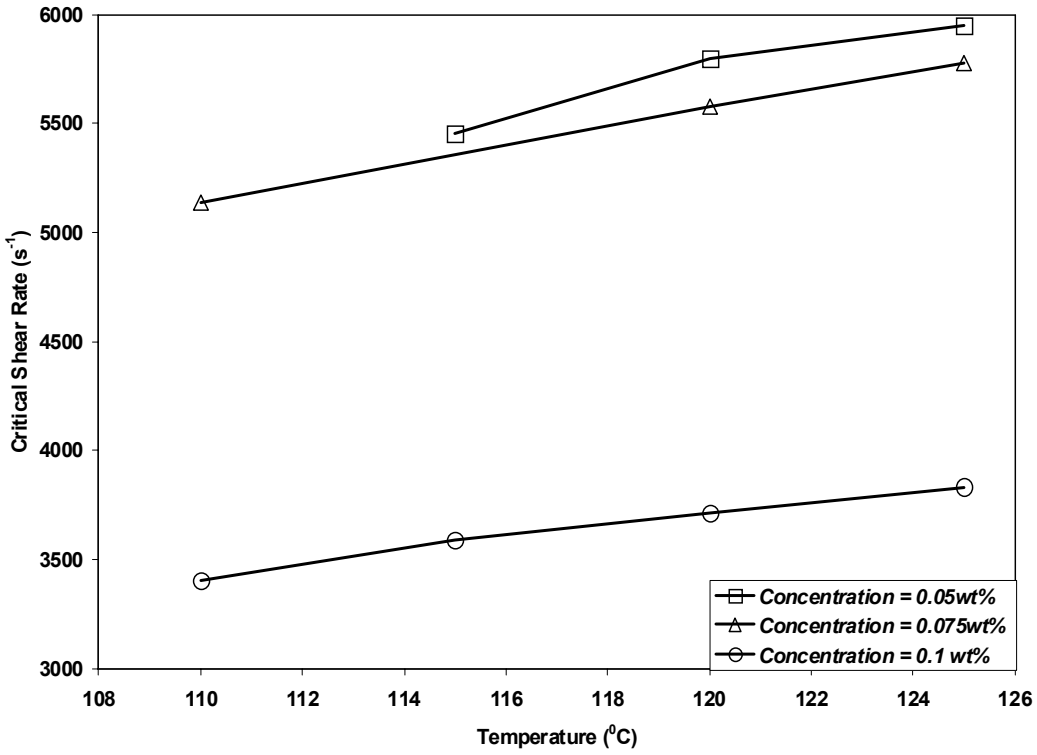

Figure 2.3: Critical shear rates of PE/x ($M = 2.90\times10^6$ g/mole) solutions as functions of the temperature for $c = 0.05,\ 0.075,\ 0.1$ wt%.

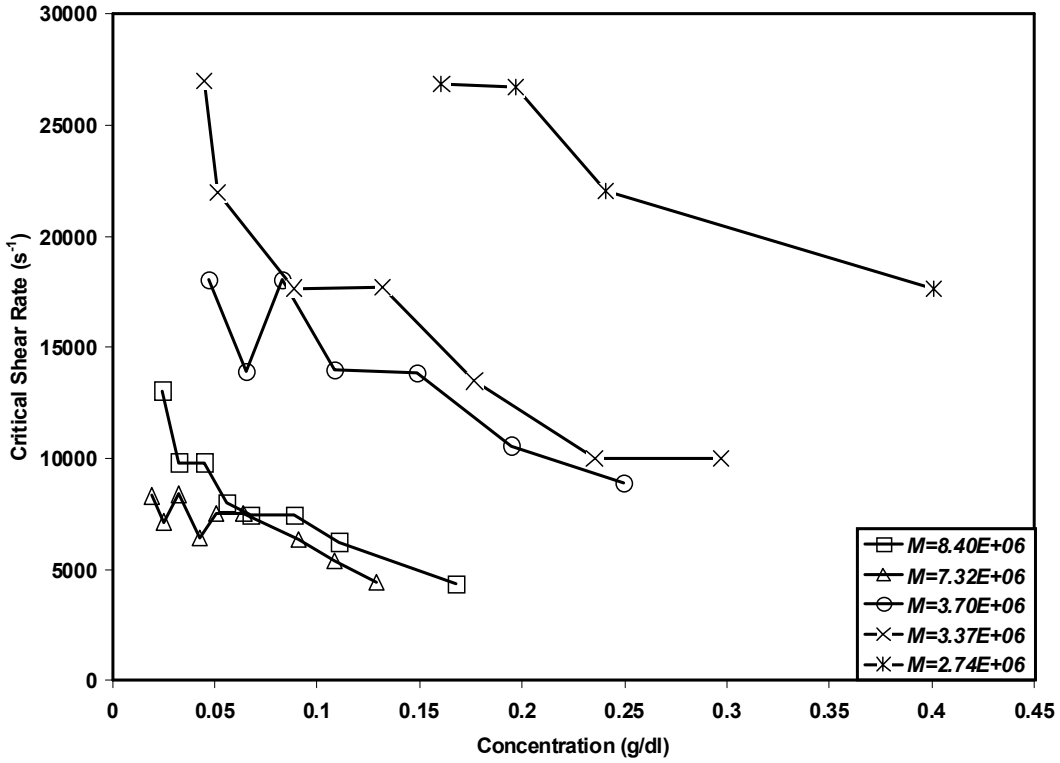

Figure 2.4: Critical shear rates of PS/d solutions as functions of the concentration for $M = 8.40\times10^6$, 7.32×10^6, 3.70×10^6, 3.37×10^6, 2.74×10^6 g/mole.

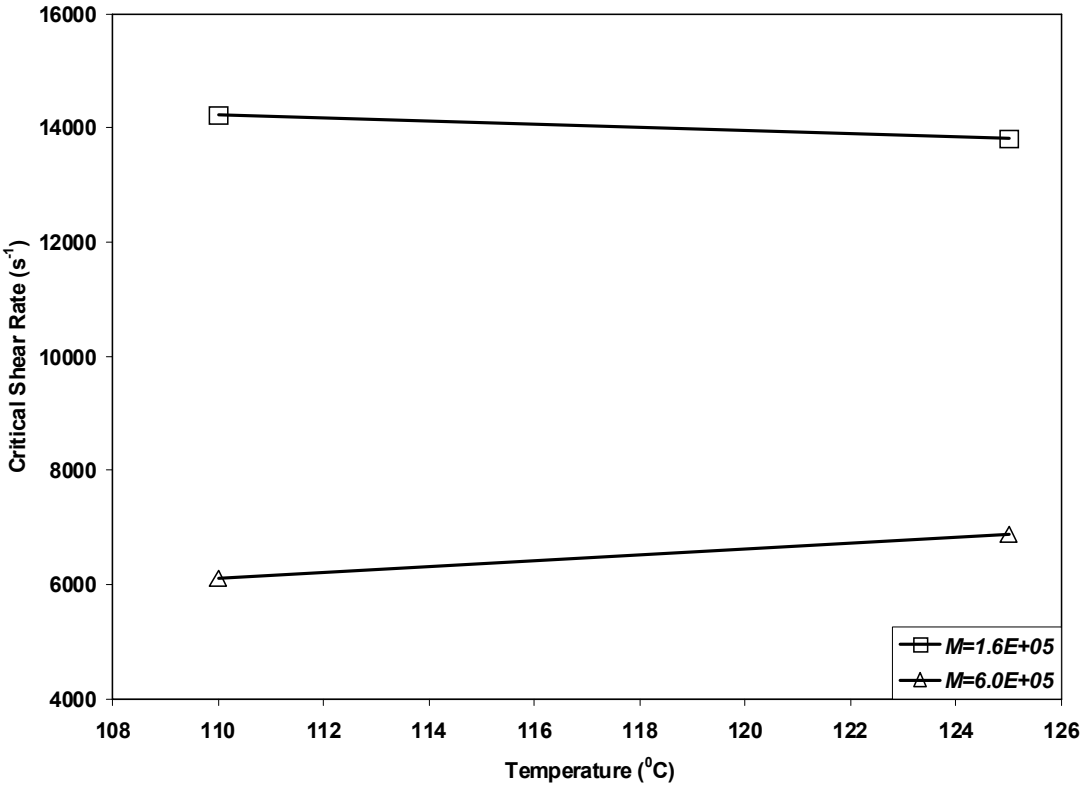

Figure 2.5: Critical shear rates of PE/x solutions as functions of the temperature for $M = 6.0\times10^5, 1.6\times10^5$ g/mole.

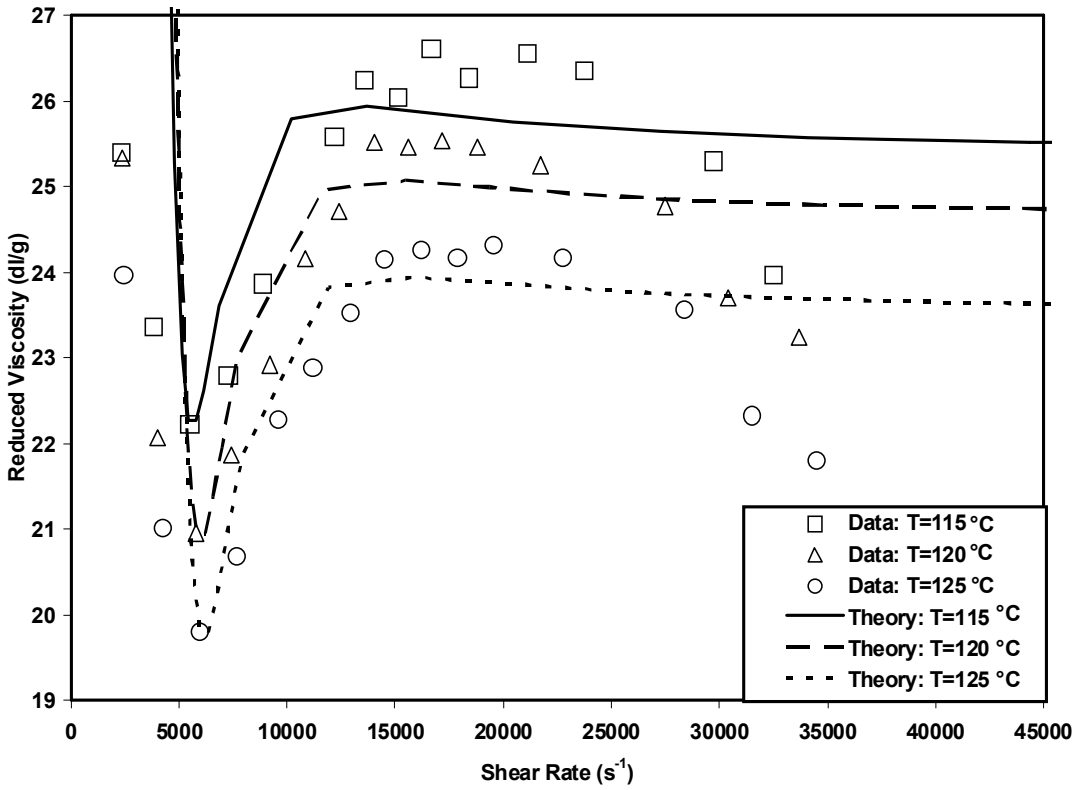

Figure 2.6: A typical plot of viscosity versus shear rate comparing model fits and experimental data for a PE/x solution at various temperatures.

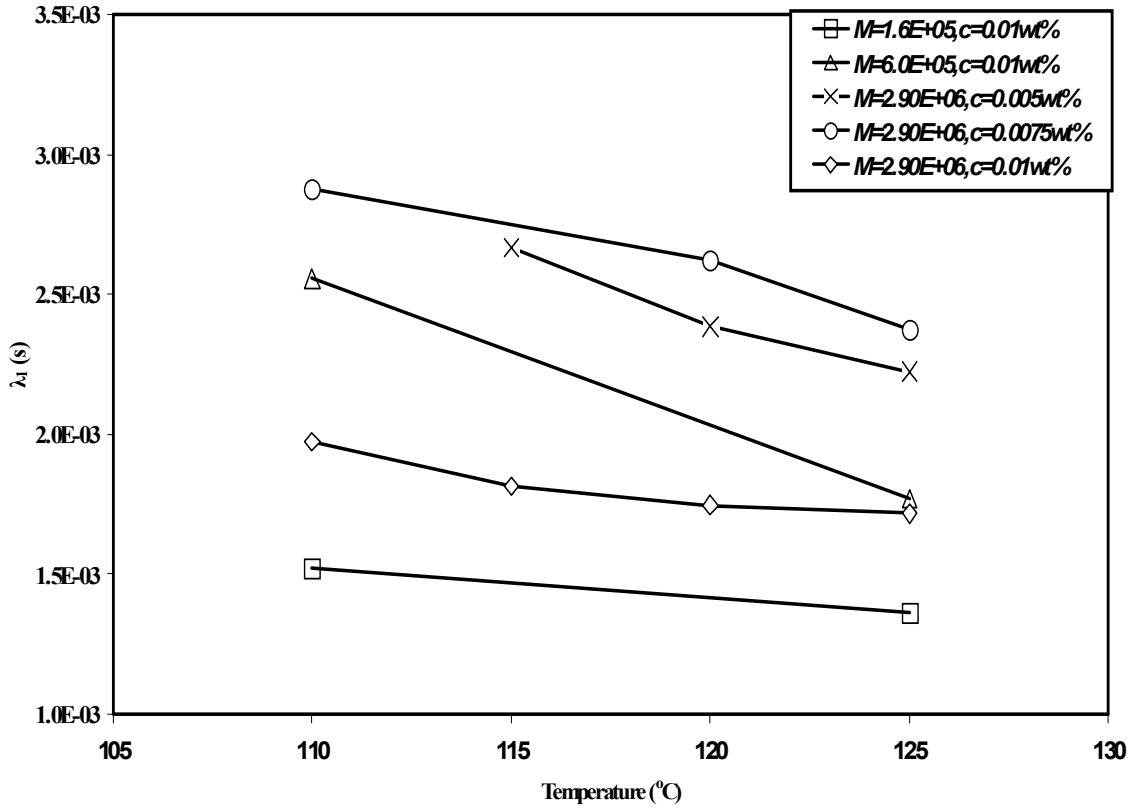

Figure 2.7: The parameter λ_1 as a function of the temperature for PE/x solutions of different molecular weights and concentrations.

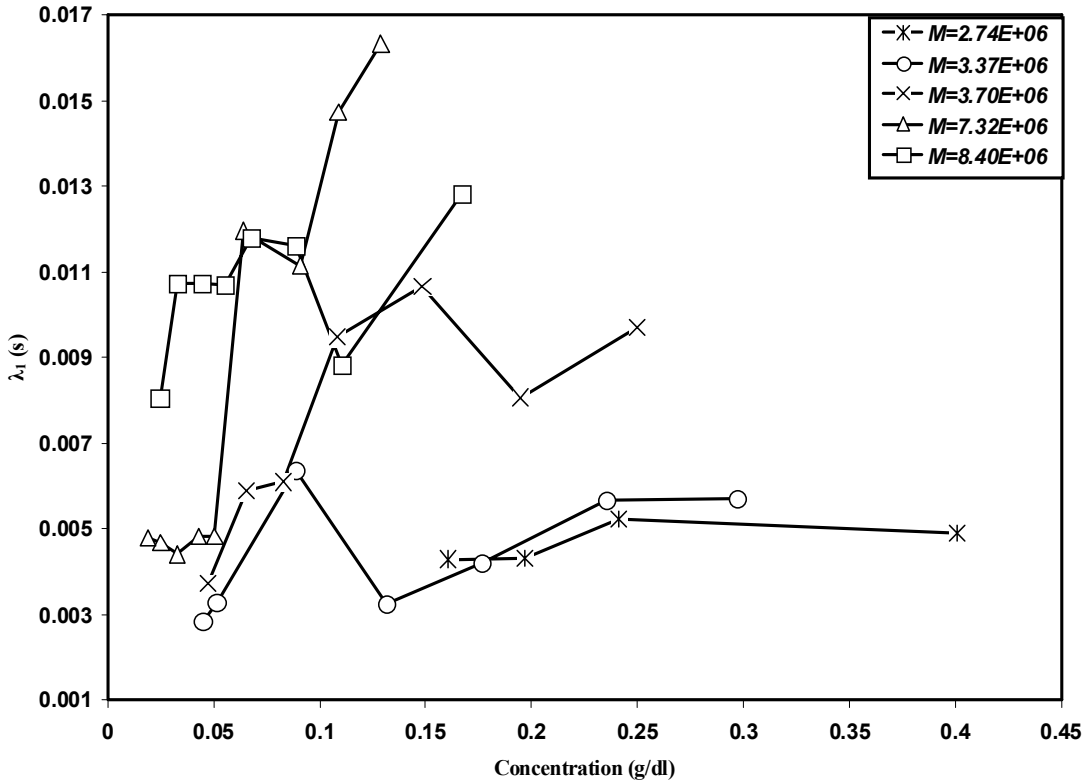

Figure 2.8: The parameter λ_1 as a function of the concentration for PS/d solutions of different molecular weights.

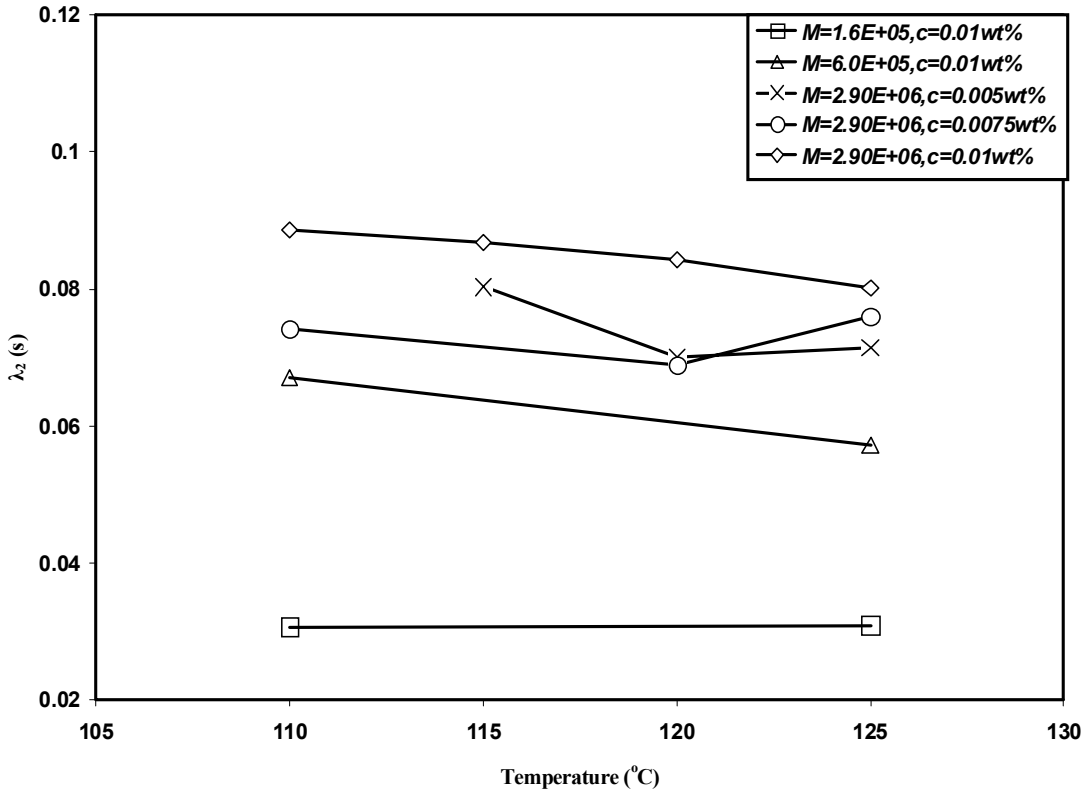

Figure 2.9: The parameter λ_2 as a function of the temperature for PE/x solutions of different molecular weights and concentrations.

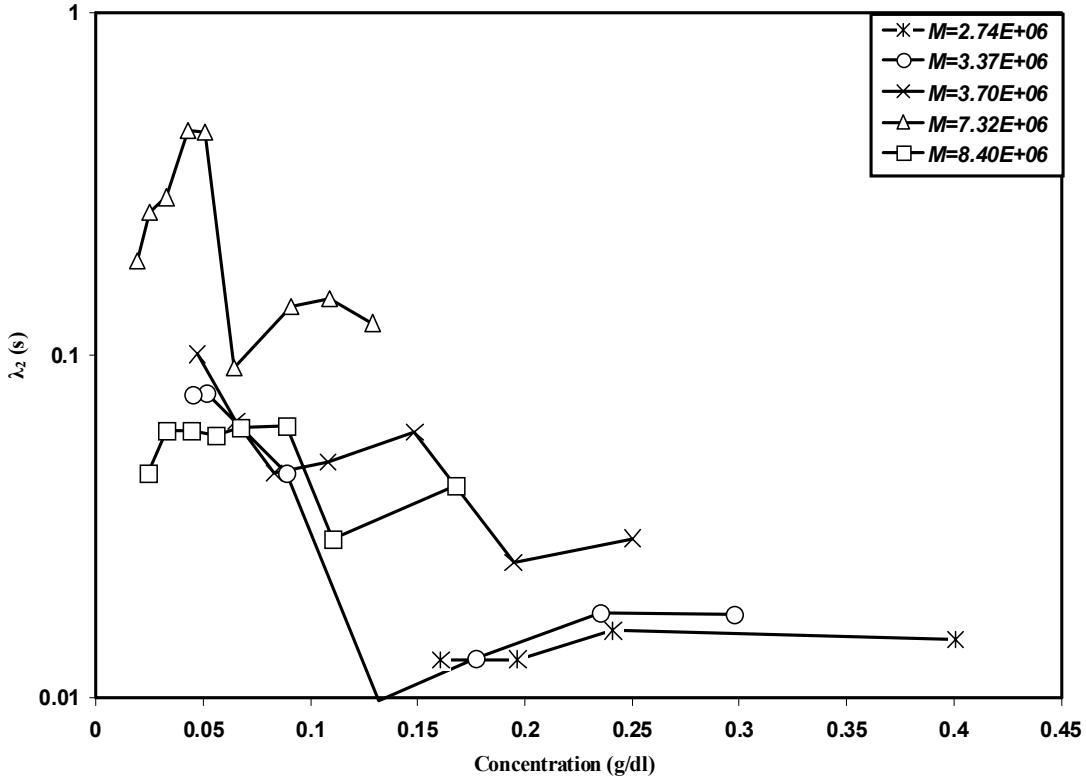

Figure 2.10: The parameter λ_2 as a function of the concentration for PS/d solutions of different molecular weights.

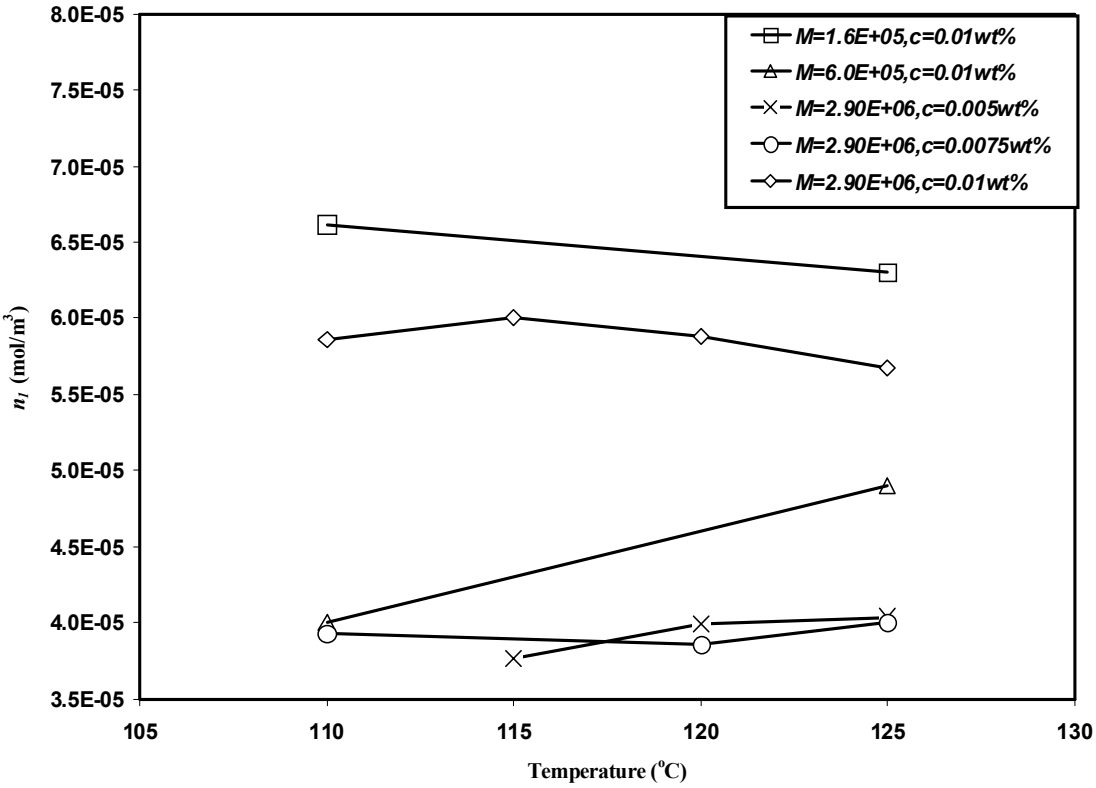

Figure 2.11: The parameter n_1 as a function of the temperature for PE/x solutions of different molecular weights and concentrations.

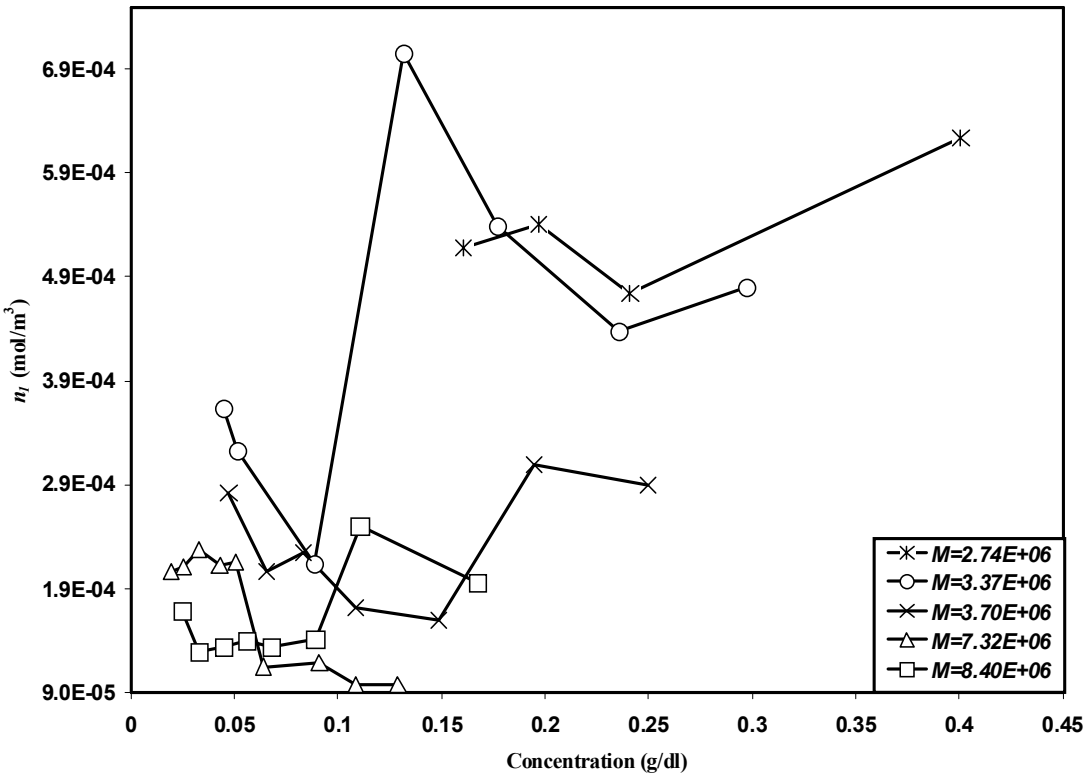

Figure 2.12: The parameter n_1 as a function of the concentration for PS/d solutions of different molecular weights.

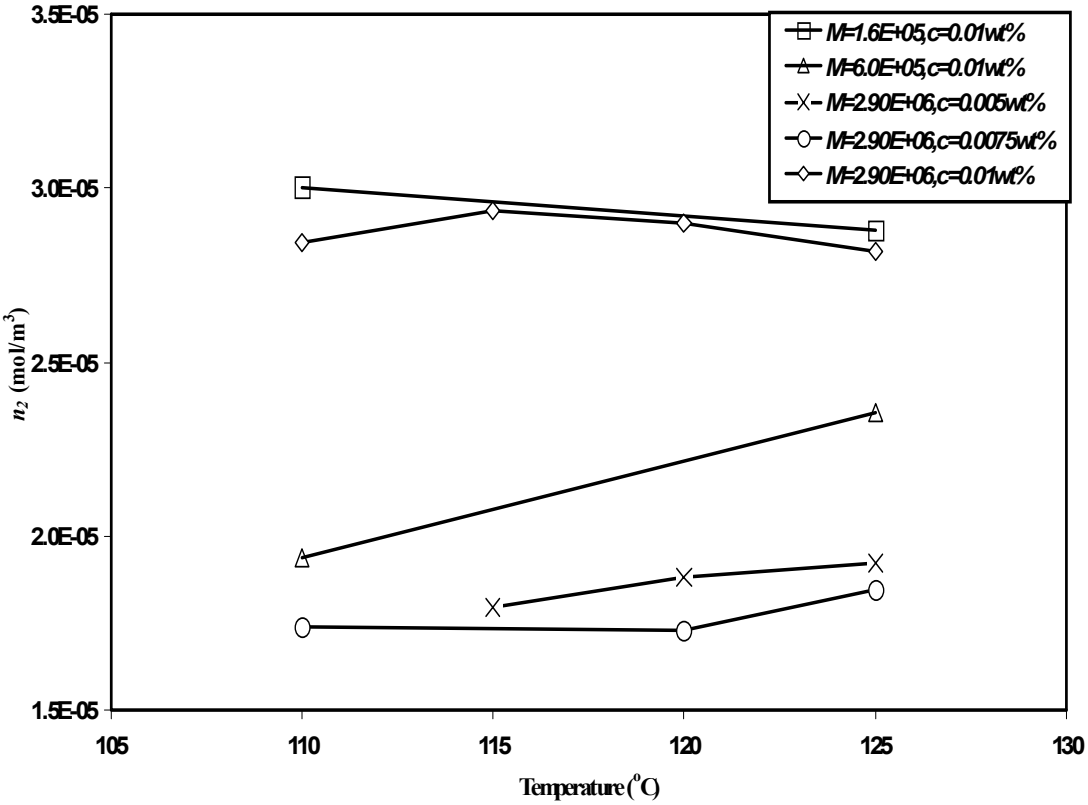

Figure 2.13: The parameter n_2 as a function of the temperature for PE/x solutions of different molecular weights and concentrations.

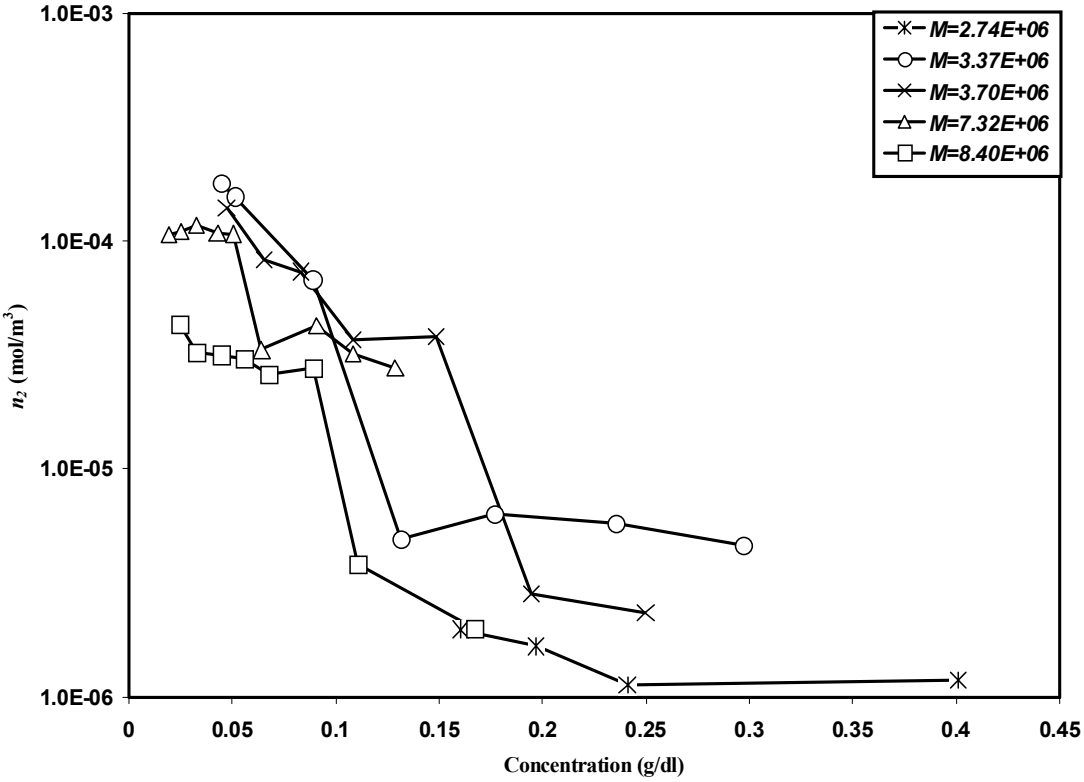

Figure 2.14: The parameter n_2 as a function of the concentration for PS/d solutions of different molecular weights.

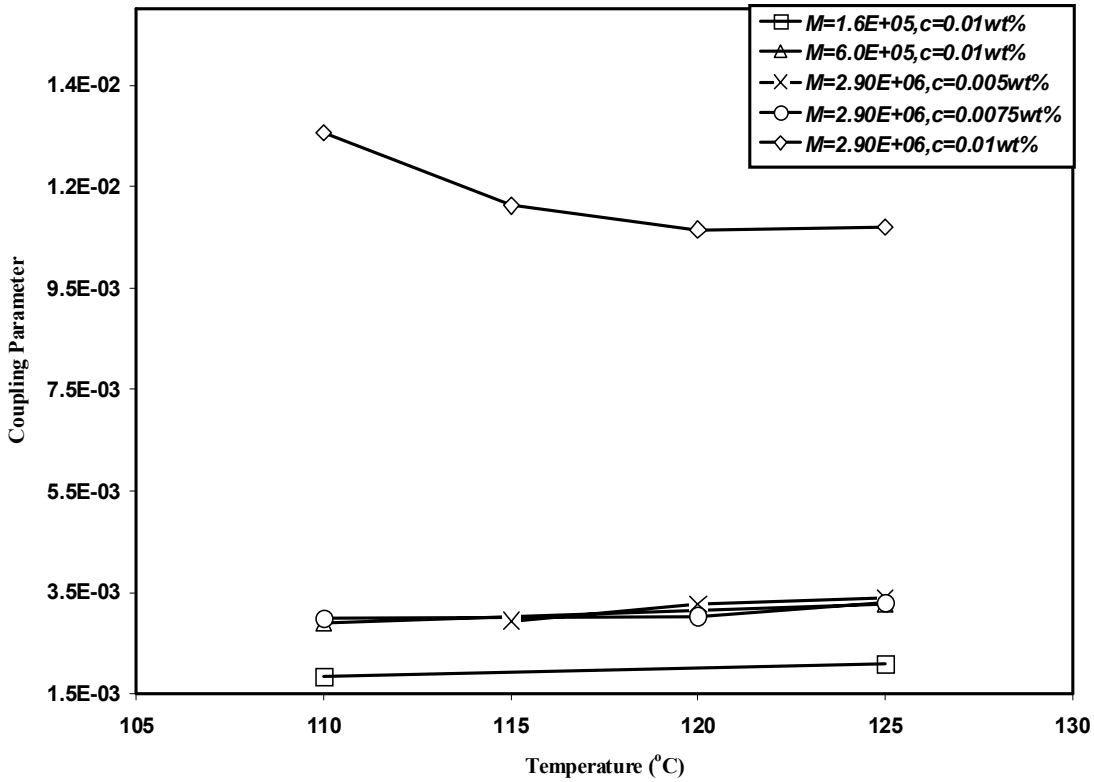

Figure 2.15: The parameter θ as a function of the temperature for PE/x solutions of different molecular weights and concentrations.

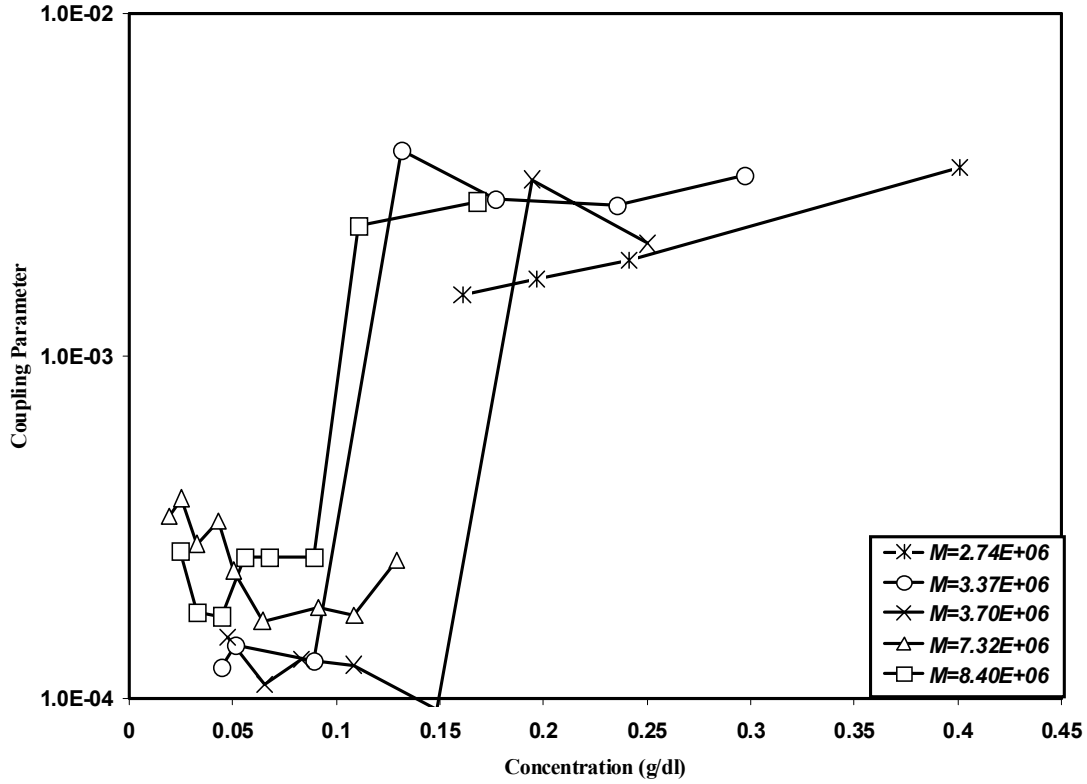

Figure 2.16: The parameter θ as a function of the concentration for PS/d solutions of different molecular weights.

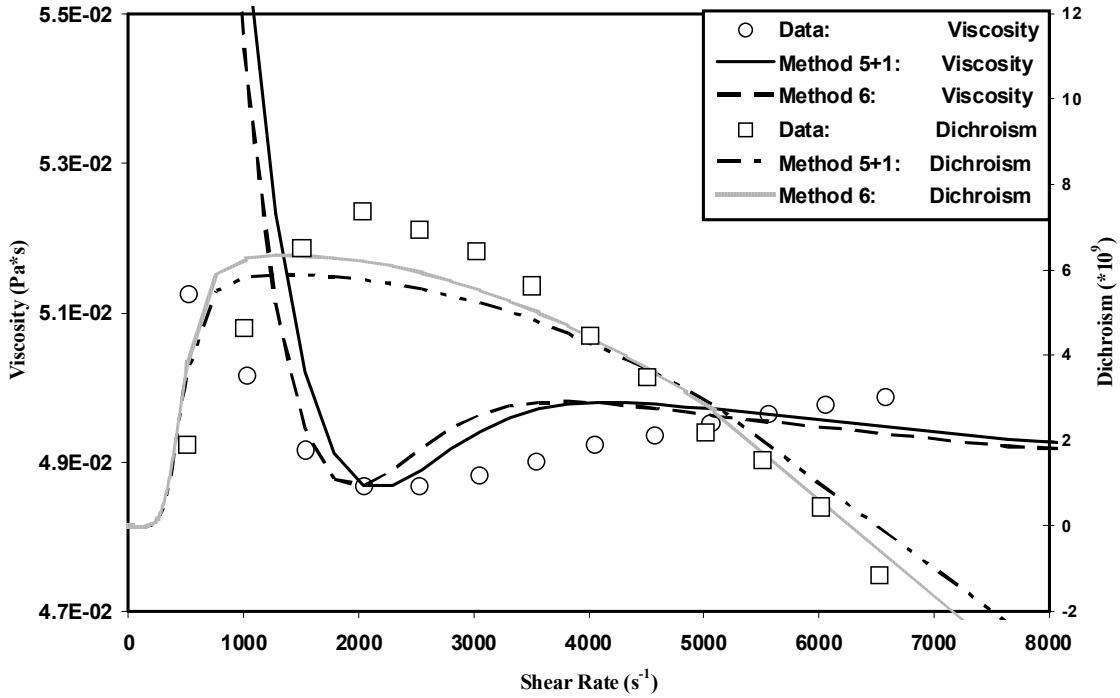

Figure 2.17: Viscosity and dichroism versus shear rate for the TCMM Model and experimental data for a PS/d solution (6.8×10^{6} g/mole, $c = 0.25$ g/dl) at $25°C$.

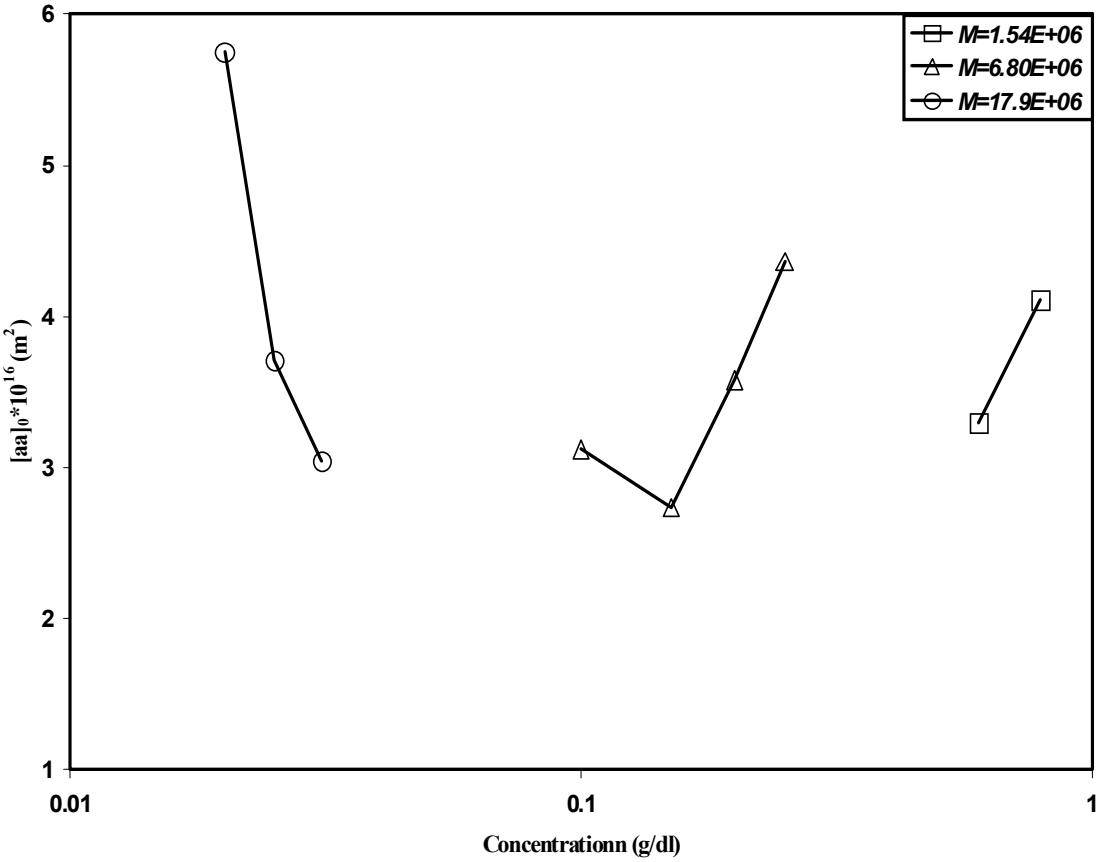

Figure 2.18: The parameter $\langle \mathbf{aa} \rangle_0$ as a function of the concentration for PS/d solutions of different molecular weights.

PART 3

A Test Case for Predicting the Rheological Properties of Polymeric Liquids: the Multiple Coupled Maxwell Modes Model

This part is revised slightly from a paper by the same name published in the "Journal of Non-Newtonian Fluid Mechanics" in 2004. The full citation is:

B. Jiang, P. Kamerkar, D. J. Keffer, B. J. Edwards, "A Test Case for Predicting the Rheological Properties of Polymeric Liquids: the Multiple Coupled Maxwell Modes Model", J. Non-Newtonian Fluid Mech., 120(2004), 11-32.

In this part, "we" refers to my co-authors and myself. My primary contributions include: (1) development of the computational methods and model equations; (2) development of the data-fitting strategy; (3) all of the computational work and analysis; (4) most of the writing.

3.1 Introduction

Over the past half century, theoretical rheologists world-wide have faced a daunting and so far unrealizable challenge: to derive a rheological model for polymer melts and solutions that can actually predict data quantitatively for experiments that have not yet been conducted. Of course, that statement alone only begins to state the nature of the challenge. In more detail, rheologists want a model that can be parameter fit to a few simple, standard experiments, and then used, without changing the parameter values, to predict the results of any other conceivable experiment on the same material, regardless of how complicated. Indeed, this is the Holy Grail of rheology, and only when this goal has finally been attained can practicing engineers actually use rheological simulations to design intricate flow processes involving real polymeric materials.

Only in the past five years have rumors of grail sightings begun to spread. Real polymers have whole spectra of relaxation times. If one wishes to produce a model capable of describing quantitatively all of the rheological properties of a polymeric liquid in all types of flow fields (and not just one property here, one there, but never both at the same time), then one must have the concept of multiple relaxation modes embedded in the model. Furthermore, these relaxation modes affect each other; i.e., they do not act independently. Indeed, a multiple, uncoupled mode version of the Upper-Convected Maxwell Model (UCMM) gives exactly the same erroneous predictions as the single-mode version for nonlinear viscoelastic response, although it works well for the linear response. Of course, one wants a model that works for *both* linear and nonlinear viscoelastic responses, and hence one is forced to allow some form of interaction to occur between the various relaxation modes of the polymeric fluid.

It was during the past five year period, alluded to earlier, that researchers have begun taking relatively new rheological models (developed over the past two decades) that were written in terms of two *coupled* relaxation modes (in one form or another), and extending them to six, eight, or even ten relaxation modes simply by duplicating the model two, three, or four times. Hence one ended up with a multiple relaxation modes model, with pair-wise coupling between the various modes. Unfortunately, this technique does not allow for anything more than pair-wise coupling; this difficulty was overcome by the approach of Ref. [3.1] used to develop the fully-coupled MCMM Model.

A number of these two coupled modes models are summarized in Section 3.8.2 of Ref. [3.1]. As a recent example, consider the Pom-Pom Model of McLeish and Larson [3.2] and the thermodynamically consistent Pom-Pon Model of Öttinger [3.3], both

referred to collectively as the PP Model in the sequel. This model contains two variables in addition to the velocity gradient field, one associated with the relative backbone stretch of the polymers and the other with the backbone orientation. These variables effectively represent two relaxation modes, since each variable has its own evolution equation with relaxation-type terms on the right-hand side. The key here, however, is that the evolution equations are coupled, and one variable cannot relax without affecting the relaxation of the other. In a recent article [3.4], Chodankar et al. used a twelve-mode PP Model with pair-wise coupling by duplicating the two evolution equations (just described) the requisite number of times (6). Initial indications described in Ref. [3.4] were quite encouraging with respect to fitting experimental data.

All that being said, one must wonder what is actually essential for accomplishing this formidable task. The original derivations of the PP Model [3.2, 3.3] and other recent multiple-mode models rely on ideas conceived at the molecular level of description through reptation theory. Many such mechanisms such as "tube stretching" and "convected constraint release" are now cited to rationalize the molecular-level dynamics giving rise to macroscopic rheological responses, and with good reason; however, when one duplicates the evolution equations for a given model several times over to obtain a multiple-mode version of the same model (with pair-wise coupling), the result essentially becomes phenomenological, no matter how sacrosanct its physical origins. Consequently, one is forced to wonder if such sanctity is even called for in the first place if one's only goal is to fit quantitatively experimental rheological behavior, while eschewing knowledge of the underlying molecular mechanisms that give rise to it. Is it possible, perhaps, that gross and flagrant phenomenology in its simplest and purest form can do

just as good of a job in guiding the persevering rheologist to the deep, dark, underground vault to the Holy Grail?

In this article, the above-stated premise is examined in detail. There was not enough time to complete this examination prior to *The 3rd International Workshop on Nonequilibrium Thermodynamics* at Princeton, but the results thus far are highly suggestive. To begin this examination, the simplest multiple-mode phenomeno-logical model one can possibly deduce is taken as the fundamental basis: the Multiple Coupled Maxwell Modes (MCMM) Model derived by Beris and Edwards [3.1] ten years ago. This model is nothing more than an extension of the usual multiple-mode version of the UCMM, except it was derived using the principles of nonequilibrium thermodynamics, which were espoused at this workshop. Using these principles, it was apparent that the various relaxation modes of the Multiple-Mode Maxwell Model should interact with each other, and the simplest possible expressions for these interactions were developed [3.1].

From this point forward, the MCMM Model is simplified further: all couplings are restricted to be pair-wise. Thus each mode affects and is affected by only one other mode. The reason for this is two-fold. First, this limits the generality of the MCMM Model to the special case of the replicated two-mode models, which were discussed earlier. Thus we can examine the basic physics of a whole class of models at the same time. Second, it allows us to examine the effect of coupling on rheological responses in the simplest circumstance. For this latter reason, in this paper we also limit ourselves to Maxwell modes: linear, infinitely extensible springs and only Maxwell-type relaxation terms (i.e., no Giesekus-type relaxation terms, for example). Consequently, one has a model that is very similar in spirit to the multiple-mode version of the PP Model examined by

Chodankar et al. [3.4], described earlier, but without any explicit accounting of the underlying molecular-level dynamical responses. Can such blatant phenomenology actually allow for the prediction of unmeasured rheological data? Probably not, but it can certainly act as a divining rod to point the persevering rheologist in the right direction.

3.2 Objective

In this work, we examine the possibility that the MCMM Model can simultaneously describe the quantitative rheological properties of polymer melts in diverse flow fields, including regimes in which the viscoelastic response is both linear and nonlinear. Specifically, we model four types of experimental data: (i) transient and (ii) steady-state shear flow, (iii) small-amplitude oscillatory flow, and (iv) transient elongational flow.

In this work, we limit ourselves to, at most, eight modes. As stated in the introduction, the modes are coupled pair-wise. There is no reason to expect a priori that eight modes are sufficient to describe quantitatively the rheological data over a very large range of experiments and deformation rate regimes: for instance, in the work of Chodankar et al. [3.4] discussed earlier, twelve modes were needed. We limit ourselves to eight modes in this preliminary paper so that we can examine the model behavior from the ground up; i.e., by starting with one pair of modes and adding additional pairs as necessary. Only by such a method can true understanding by achieved. Furthermore, to achieve true understanding of mode coupling, we must work with the simplest model possible, which is why we are examining Maxwell modes in this test case.

To obtain the parameters necessary to use the model, we want to optimize its fit to as little experimental data as possible, and to use only easily obtainable data taken with standard rheological testing equipment. It is thus critical to have a good optimization scheme. In this preliminary work, we use the most basic optimization scheme available, the Nelder and Mead Downhill Simplex Method (NMDSM) [3.5], because it is easy to implement and use. We had no desire, initially, to spend a great deal of time and effort developing a sophisticated optimization scheme only to find out later that our overall goal was unobtainable. Furthermore, we wanted to use an optimization method that anyone could use, not just an expert in the subject. Polymer engineers need not only viable models, but also straightforward methods for using them. Consequently, one of our tasks for this article is to demonstrate that this simple technique, which can be found in any numerical recipe text, can be used successfully to fulfill our goal.

In light of the above remarks, the objective for this preliminary study is to fit, as quantitatively as possible, data from several different rheological experiments over large ranges of deformation rates using at most eight pair-wise coupled Maxwell modes. From this exercise, we wish to determine how much and what kind of experimental data is absolutely necessary for parameterization of a typical rheological model. What special techniques are needed for the optimization of parameters? Hopefully, this preliminary report will provide the answers to these questions, so that a more thorough study can address the primary goal or predicting rheological data for real polymeric fluids.

3.3 The Multiple Coupled Maxwell Modes Model

The Multiple Coupled Maxwell Modes Model used herein is restricted to pair-wise coupling between the modes. Consequently, it is essentially a replicated version of the Two Coupled Maxwell Modes (TCMM) Model, discussed at some length in Refs. [3.1, 3.6, 3.7]. The TCMM Model is written in terms two conformation tensors, $c^1(x,t)$ and $c^2(x,t)$. These two tensors describe the distribution and orientation of chain segments associated with the two supposed relaxation mechanisms [3.1, 3.6, 3.7]. These two conformation tensors are affected by the imposed flow field and by each other. In the TCMM Model, the evolution equation for the first tensor, $c^1(x,t)$, is

$$\frac{\partial c^1_{\alpha\beta}}{\partial t} + v_\gamma \nabla_\gamma c^1_{\alpha\beta} - c^1_{\alpha\gamma}\nabla_\gamma v_\beta - c^1_{\beta\gamma}\nabla_\gamma v_\alpha = -\frac{1}{\lambda_1}c^1_{\alpha\beta} + \frac{k_B T}{\lambda_1 K_1}\delta_{\alpha\beta} - \frac{\theta}{2k_B T}\sqrt{\frac{n_2}{n_1}}\frac{1}{\sqrt{\lambda_1\lambda_2}} \times\left[K_2\left(c^1_{\alpha\gamma}c^2_{\beta\gamma} + c^2_{\alpha\gamma}c^1_{\beta\gamma}\right) - 2k_B T c^1_{\alpha\beta}\right] \tag{3.1}$$

where k_B is Boltzmann's constant, T is the absolute temperature, K_1 and K_2 are the Hookean spring constants of the respective Maxwell mode, n_1 and n_2 are effective concentrations of the two modes, λ_1 and λ_2 are the constant relaxation times of the two modes, and θ is the degree of interaction between the two modes. The evolution equation for the second mode-conformation tensor, $\mathbf{c}^2(\mathbf{x},t)$, can be obtained from Eq. (3.1) by permuting the mode indices.

Physically, the parameters λ_1, λ_2, n_1, and n_2 must be greater than or equal to zero. The model typically requires that θ is bounded between -1 and 1 [3.1, 3.6]; however, this parameter is normally a small positive fraction [3.6, 3.7]. These five parameters must be obtained from fits of the model to experimental data.

The extra stress tensor, $\sigma_{\alpha\beta}$, can be expressed as a linear sum over the mode conformation tensors,

$$\sigma_{\alpha\beta} = \sum_{i=1}^{2} \left(n_i N_A K_i c^i_{\alpha\beta} - n_i N_A k_B T \delta_{\alpha\beta} \right) \tag{3.2}$$

where N_A is Avogadro's number. This expression can be used to calculate the rheological properties of the polymeric liquid.

Equation (3.1) can be rewritten in terms of the mode stress tensors after substituting the expression for the extra stress tensor given by Eq. (3.2):

$$\lambda_1 \frac{\partial \sigma^1_{\alpha\beta}}{\partial t} + \sigma^1_{\alpha\beta} + \theta \frac{n_1}{n_2} \sqrt{\frac{n_1 \lambda_1}{n_2 \lambda_2}} \sigma^2_{\alpha\beta} + \frac{\theta}{2 n_2 N_A k_B T} \sqrt{\frac{n_1 \lambda_1}{n_2 \lambda_2}} (\sigma^1_{\alpha\gamma} \sigma^2_{\gamma\beta} + \sigma^2_{\alpha\gamma} \sigma^1_{\gamma\beta}) = \eta_1 (\nabla_\alpha v_\beta + \nabla_\beta v_\alpha) \tag{3.3}$$

The equation for σ^2 can be obtained from Eq. (2.3) by permuting the mode indices. The complex modulus can be expressed as [3.1, 3.6]

$$\frac{G}{i\omega} = \frac{\eta_1 (De_2 i + 1) + \eta_2 (De_1 i + 1) \sqrt{\eta_1 \eta_2} \theta \chi}{(1 - De_1 De_2) + i(De_1 + De_2) - \theta^2} \tag{3.4}$$

where $De_i \equiv \omega \lambda_i$, $\eta_i = n_i N_A K_B T \lambda_i$, and $\chi = \frac{\eta_1 De_2}{\eta_2 De_1} + \frac{\eta_2 De_1}{\eta_1 De_2}$. Note that only four of the coefficients λ_1, λ_2, n_1, n_2, and θ can be determined from the complex modulus data [3.1, 3.6]. This implies that for any value of θ, an equivalent fit of the complex modulus data can be obtained. It also implies that if one performs only linear experiments, then it is impossible to tell whether or not mode coupling actually occurs. Thus θ can be viewed as a nonlinear fitting parameter, since it is not defined in the linear experiment.

A key point derived from the TCMM Model is the following [3.6]. Rheological experiments do not determine the relaxation time constants of materials. They determine characteristic times for materials in the rheological experiment under investigation. In the case of no coupling between the modes, it so happens that these characteristic times are equivalent to the relaxation time constants of the material. When the modes are coupled, this is not the case. For the stress relaxation experiment of Ref. [3.6], for example (see Figure 3.1[2] therein), the characteristic time associated with the larger relaxation time constant is longer that that relaxation time. For the smaller of the two relaxation time constants, the associated characteristic time is shorter than the smaller relaxation time constant.

Some useful information regarding the nature of Eq. (3.3) can be gleaned from writing it in dimensionless form,

$$\frac{\partial \tilde{\sigma}^1_{\alpha\beta}}{\partial \tilde{t}} + \sqrt{\frac{\lambda_2}{\lambda_1}}\tilde{\sigma}^1_{\alpha\beta} + \theta\sqrt{\frac{n_1}{n_2}}\tilde{\sigma}^2_{\alpha\beta} + \frac{\theta}{2}\sqrt{\frac{n_1}{n_2}}(\tilde{\sigma}^1_{\alpha\gamma}\tilde{\sigma}^2_{\gamma\beta} + \tilde{\sigma}^2_{\alpha\gamma}\tilde{\sigma}^1_{\gamma\beta}) = \nabla_\alpha \tilde{v}_\beta + \nabla_\beta \tilde{v}_\alpha \tag{3.5}$$

In this expression, the dimensionless quantities are defined as $\tilde{t} \equiv t/\sqrt{\lambda_1\lambda_2}$, $\nabla_\alpha \tilde{v}_\beta \equiv \sqrt{\lambda_1\lambda_2}\ \nabla_\alpha v_\beta$, and $\tilde{\sigma}^i_{\alpha\beta} \equiv \sigma^i_{\alpha\beta}/n_i N_A k_B T$. The evolution equation for mode two is obtained from Eq. (3.5) by permuting the indices. These expressions indicate for a given value of $\theta \neq 0$ that, as the ratio n_1/n_2 increases, mode 2 has more of an effect on mode 1, and mode 1 has less of an effect on mode 2. As the ratio λ_1/λ_2 increases, mode 2 has more effect on mode 1, and mode 1 has less effect on mode 2. If n_1 is much larger than n_2, it is tempting to claim that the total stress is approximately $\tilde{\sigma}^1$; however, since

[2] All the tables and figures are located in the appendix at the end of part

the dimensionless equations are nonlinear in the mode stress tensors, this is not necessarily so unless $\theta = 0$. Furthermore, whether θ is positive or negative determines whether the mode coupling acts to augment or alleviate stress in the material.

As mentioned above, more than two relaxation modes are necessary to describe polymer melts, since a spectrum of relaxation times exists for these materials. For example, we cannot get quantitatively accurate results when we use the TCMM Model to fit the complex modulus data from a polymer melt undergoing small-amplitude oscillatory flow. In Figure 3.1, we plot the storage modulus, G', and loss modulus, G'', as a function of frequency, ω, for a low-density Polyethylene (LDPE) melt with a molecular weight of 80,350 g/mol at a temperature of $175^{\circ}C$. The TCMM Model was fitted to the experimental data (using the technique described below), resulting in the parameter values specified in Table 3.1. (Note that the coupling parameter is set equal to zero: as shown in Ref. [3.6], the linear viscoelastic behavior is independent of this parameter.) From the figure, we see that the TCMM Model can only fit, at best, the gross qualitative features of the data. At lower frequencies, the TCMM Model gives a reasonable fit to the data for the loss modulus; however, this model cannot fit the data quantitatively over the whole range of frequency because higher frequencies incite shorter relaxation times to respond. The TCMM Model has just two relaxation times, which means it is very difficult to fit the complex modulus across the entire range of frequencies. Therefore, we are forced to include additional modes in the model.

Obviously, more modes are needed to describe this material. Consequently, the MCMM Model with pair-wise mode coupling is used herein. It is composed of multiple TCMM Models; i.e., pair-wise coupling is assumed between the modes. We will

investigate whether or not this assumption still maintains a sufficient degree of coupling to capture the quantitative rheological behavior of the polymer, within the current eight-mode limit, although perhaps not as efficiently as a MCMM Model with greater than pair-wise coupling.

The extra stress tensor, σ^{MCMM}, of the MCMM Model can be expressed as a linear sum over the stress tensors of the TCMM Model as

$$\sigma_{\alpha\beta}^{MCMM} = \sum_{i=1}^{N} \sigma_{\alpha\beta}^{TCMM} \tag{3.6}$$

where N is the number of TCMM mode pairs used in the MCMM Model. The evolution equations of the TCMM Model, Eq. (3.3) and its indicial permutation, can thus be used for the MCMM Model with pair-wise coupling by replicating it the requisite number of times ($N-1$).

As an initial example, we examine the performance of MCMM Model (for $N=2$) for the previously displayed complex modulus data. In Figure 3.2, we plot the storage modulus, G', and loss modulus, G'', as a function of frequency, ω, for the same LDPE as shown in Figure 3.1. Figure 3.2 shows that with the addition of two more modes, we gain an overall improvement in the fit of the model. The relative root-mean-square (RMS) error for the TCMM and MCMM ($N=2$) models were, respectively, 221% and 20%. We see a particular improvement in the fit to the low frequency data. In Table 3.1, one can see that the additional relaxation times added to the MCMM Model correspond to long times or low frequencies. The anomalous decrease observed in the loss modulus at high frequencies in both figures is simply due to the fact that we have no high-

frequency experimental data with which to fit the model, as well as the fact that four modes is still not a sufficient number to fit the linear data over such a large range of frequencies. Note that with θ set to zero in the above examples, the results are equivalent to a system of uncoupled Maxwell modes.

3.4 Experimental methodology

Shear viscosity measurements were performed using the Advanced Capillary Extrusion Rheometer (ACER) and the Advanced Rheometrics Expansion System (ARES) by Rheometrics Scientific™. All data was taken using the same LDPE described earlier. The LDPE samples were obtained from Exxon, prepared using a Ziegler-Nata catalyst and having a wide molecular weight distribution with a value of the polydispersity index that is greater than five (5.15). The value of the melt index was 0.2 g/minute, with a density of 0.923 g/cm^3. The weight-average molecular weight, according to gel permeation chromatography, was 80,350 g/mol. All the experiments were carried out at 175°C.

A variety of experimental data were obtained, all taken on the equipment described above at The University of Tennessee. The ARES was used to perform a dynamic frequency sweep in the range of about 0.01s^{-1}-100 s^{-1}. From this, we obtained the storage modulus (G') and loss modulus (G'') data in small-amplitude oscillatory shear flow (SAOSF). We gathered shear viscosity data over a wide range of shear rates (0.001 s^{-1}-40000 s^{-1}). To cover this range of shear rates, we used ARES at low shear rates, ACER at higher shear rates, and complex viscosity measurements (on ARES) to cover the range between 1 to 10 s^{-1}. Steady-state first normal stress difference data covering a

fraction of this shear rate range was also obtained using ARES, along with transient shear stress data (start up and relaxation) and first normal stress difference data. Transient elongational viscosity measurements were made with ACER using four semi-hyperbolically converging dies of Hencky strains 4, 5, 6, and 7 in the manner described in Ref. [3.8].

3.5 Numerical methodology

In the TCMM Model, six (for shear flow) coupled, ordinary differential equations (ODEs) quantify the time evolution of the independent, non-vanishing elements of the mode stress tensors in shear flows [3.6]. If we know all five of the TCMM Model parameters, then we can solve this set of ODEs to obtain the transient behavior of the polymer. At steady-state, the Newton-Raphson Method is applied to solve the resulting non-linear algebraic equations to obtain the steady-state stress. With this stress, we can calculate the steady-state shear viscosity as a function of shear rate. We can calculate the complex modulus analytically from Eq. (3.3).

In order to evaluate the transient behavior of the TCMM Model, we use the classical fourth-order Runge-Kutta method to solve the set of six coupled ODEs. This numerical solution delivers the transient behavior of the TCMM Model under an applied shear rate. In the case of uniaxial elongational flow, only four elements of the mode stress tensors are independent and non-zero, two for each tensor. The resulting four ODEs are solved in a similar manner to obtain the transient behavior of the mode stress tensors. Analogous numerical methods are used in the solution of the MCMM Model, which is simply the superposition of multiple TCMM Model results.

The technique we use to optimize the MCMM Model parameters is the Nelder and Mead Downhill Simplex Method (NMDSM), which requires only functional evaluations, not derivative evaluations [3.5]. Although this optimization technique is not very efficient in terms of the number of functional evaluations and computational effort required, the NMDSM will always find a minimum, provided that one exists. However, the NMDSM is not guaranteed to find the global minimum, which creates a challenge for its users. Insight into the physical significance of the parameters and an understanding of the underlying polymer physics is thus crucial to obtaining a good initial guess to the optimization problem. Multiple initial guesses are required in order to test whether the resulting minimum is indeed the global minimum. As the dimensions of the parameter space increase when the number of mode pairs increases, optimization using this method can require substantial computational time.

The constraints on the parameters have been discussed in Section 3. In this work, we restrict θ to the range [0, 1], and we also add a constraint such that the elongational viscosity, η_e, in uniaxial extensional flow monotonically increases with time, $\frac{\partial \eta_e}{\partial t} \geq 0$, for each TCMM pair. This constraint is a physically reasonable assumption and prohibits some aphysical results that can occur for outlying parameter values.

We used the following expression for the objective function, F_{obj}, which is the function minimized by the NMDSM:

$$F_{obj} = \sqrt{\frac{\sum_{j=1}^{n_{type}} \sum_{i=1}^{n_j} w_{i,j} \left(\frac{R_{i,j,\exp} - R_{i,j,\text{model}}}{R_{i,j,\exp}} \right)^2}{\sum_{j=1}^{n_{type}} n_j \sum_{i=1}^{n_j} w_{i,j}}} \tag{3.7}$$

In this expression, n_{type} is the number of data types (our data include complex modulus, steady-state shear viscosity, first normal stress difference, and transient elongational viscosity), n_j is the number of data points of a specific type of data, $w_{i,j}$ is the weight factor of the corresponding data, and R is the result from either the experiment or model.

Since the dimension of solution space (the number of parameters) is not less than five for the MCMM Model, the method used to obtain a reasonable initial guess is vital to the optimization code. Generally, we fit the complex modulus data from the SAOSF experiment by varying λ_1, λ_2, n_1, and n_2, while holding $\theta = 0$ with $N = 1$. If this was unable to obtain a satisfactory fit, we increased the number of mode pairs, one pair at a time. Our initial guess for N mode pairs used the converged solution for $N-1$ mode pairs, plus new values for the parameters of the additional mode pair. We believe that the relaxation times should not overlap, so we always used initial guesses for the relaxation times with different orders of magnitude than those already represented in the $N-1$ mode pairs. Furthermore, for initial guesses of the modal concentrations, n_1 and n_2, we chose null values. When fitting the complex modulus data, we set $\theta = 0$ for all modes.

Once we had the complex modulus data fit well, we then used the converged values of the parameters as an initial guess to simultaneously fit both steady-state shear viscosity and complex modulus data. Finally, we also used the optimized parameter set from the previous step as the initial guess to fit simultaneously four sets of experimental data, including: (i) complex modulus, (ii) steady-state shear viscosity, (iii) steady-state first normal stress difference, and (iv) transient elongational viscosity. We did not

include the experimental data for the transient shear stress or first normal stress difference among the data that we fit.

Over the past few decades, several different methods have been put forth for fitting rheological models (typically composed of uncoupled Maxwell modes) to linear viscoelastic data; e.g., see Refs. [3.9-3.14]. Over time, these methods have generally become more sophisticated as computational capabilities have increased, and have done a better job of fitting parameters with smaller RMS error. These methods are, however, not easily generalizable to cases involving nonlinear viscoelastic data and more complicated rheological models. Such methods that do exist for fitting nonlinear viscoelastic data suffer from a lack of sophistication. We are not addressing the issue of sophistication in this article; we want to employ a crude optimization methodology in order to examine what is possible for the average industrial polymer engineer to achieve with a given rheological model.

In order to examine whether or not our optimization technique is sufficiently utile for this application, we must compare it with one of the sophisticated methods mentioned above. Those methods, as discussed above, are only for linear viscoelastic data. Although there is no basis of comparison for nonlinear viscoelastic data, we can compare our methodology to prior optimization methods for linear data. In Figure 3.3, the same experimental data of Figures 3.1 and 3.2 is presented, along with a fit with six uncoupled Maxwell modes using the Padé-Laplace methodology of Simhambhatla and Leonov [3.10, 3.14] as represented by the authors' *PADLAP* program. The RMS error of this sophisticated fit is 6%, which is quite good. We believe that six modes is the minimum number needed by this method to get a very good fit of the experimental data. The

parameter values obtained from the optimization routine are presented in Table 3.2, which were actually generated first by Dr K.F. Wissbrun for the experimental data [3.15]. Suffice it to say that the exact same fit can be obtained using the optimization routine developed in this work, but it takes considerably more computational time. With contemporary desktop computers, however, this is not a serious issue; less than a minute of computational time is required on a machine running a single Pentium 4™ processor. Furthermore, if the coupling parameters in the (six-modes, pair-wise coupling) MCMM Model are set to null values (i.e., the special case of uncoupled Maxwell modes), then not only is the fit the same as in the more sophisticated code, but the parameter values obtained are exactly the same as well (within 1% RMS error). Thus we conclude that, at least as far as the linear viscoelasticity data is concerned, our optimization methodology is sufficient to the task under consideration.

3.6 Discussion of optimization results

Consistent fits for the data of complex modulus, shear viscosity, elongational viscosity, and first normal stress difference were obtained with the MCMM Model using four pairs of modes. Although the linear data of Figure 3.2 could be fit well with only six modes, we are now fitting more experimental data and nonlinear data at that. This nonlinear data was taken in deformation rate regimes that do not necessarily correspond to the frequency range of the SAOSF experiment. Consider this example: the SAOSF frequency range was roughly from 0.01 to $100s^{-1}$. This experiment thus excites relaxation modes that correspond to this range of frequencies. However, the steady shear viscosity data, as seen below, extends up to shear rates of about $10^5 s^{-1}$. These higher

shear rates excite shorter relaxation times than appear in the SAOSF experiment, and thus cannot be fit from the linear data alone. Consequently, we add two more modes in order to capture the high shear rate dynamics not represented in the SAOSF data.

After fitting the data in the manner described above, theoretical predictions from the model were then obtained for the transient shear stress and transient first normal stress difference. The parameter values obtained from the optimization routine are listed in Table 3.3. They will be discussed in depth in the next subsection.

3.6.1 The Distribution of Relaxation Times

One might expect that the relaxation time for each mode should be sufficiently distinct from every other relaxation time, separated by perhaps an order of magnitude. In Table 3.3, we see that the relaxation times span six orders of magnitude, from 10^{-5} to 1 s; but with eight modes, it is obvious that some relaxation times will be closely replicated. We can explain this in part by considering a material where the mode with a relaxation time on the order of 10^{-4} s needs to couple with both the 100 s mode and the 10^{-1} s mode. In the MCMM Model, this degree of coupling requires that the 10^{-4} s mode be represented twice, since we have only pair-wise coupling. This situation is represented by the second and third mode pairings in Table 3.3. The more general form of the MCMM Model, allowing for greater than pair-wise coupling, might rectify this situation. Still, this does not explain the full story since the first and fourth mode pairs in Table 3.3 have the same order of magnitude of relaxation times, 10^{-5} s and 10^{-3} s, for both modes in the pair. The distinction here is in the modal concentrations. In the fourth pair, the concentrations are in the same order of magnitude, meaning both modes are present and

active. In the first pair, the concentration of the 10^{-3} s mode is fifteen orders of magnitude smaller than that of the 10^{-5} s mode. Thus in the first pair, we have the 10^{-3} s mode acting in a virtually uncoupled manner. In order to include the action of an uncoupled mode in the formalism of the MCMM Model, the mode is paired with another mode with zero concentration.

We settled on four pairs of modes in this preliminary work, so as to obtain reasonable fits with as few parameters as possible. We felt that this was enough to allow decent fits without unduly sacrificing the ability to understand how the model works. Of course, additional modes would reduce the error of the model in matching the experimental data, but the enhancement is quantitative in nature, rather than qualitative, and was deemed unnecessary at this stage. The uncertainty of locating the global minimum in the numerical methodology allows for the possibility that fewer modes are actually required to fit the rheological data. Furthermore, we must acknowledge the limitations of the model, which restrict the full generality of the MCMM Model to pair-wise coupled modes. Also limiting the model are the assumption of Maxwell modes, which have the artificial feature of linear, infinitely extensible springs and linear relaxation terms. More realistic models, incorporating FENE springs and/or Giesekus-type relaxation mechanisms, would probably lead to better results with fewer relaxation modes. Future work will address these issues.

In Figure 3.4, we plot the experimental data and the model fit with $N = 4$ for the complex modulus versus frequency in the SAOSF experiment. The model "Result_1" stands for the parameters values listed in Table 3.3, whereas "Result_2" stands for the fit with the parameters of Result_1 when the smallest concentration (n_i) and the

corresponding coupling parameter (θ) are set to zero. (We will explain the rationale behind this designation momentarily.) In this figure, we display the same experimental data as in Figures 3.1-3.3. We know that by increasing the number of modes, we can fit the data more accurately; however, whereas in Figures 3.1 and 3.2 we fit only to the experimental complex modulus data, in Figure 3.4 we fit the model (with $N = 4$) simultaneously to data for the complex modulus, steady-state shear viscosity, first normal stress difference, and transient elongational viscosity data. Thus, if we only compare Figures 3.2 and 3.4, we cannot observe a visual alteration of the fit. There is a 16% relative RMS error in Figure 3.4 (Result_1) compared to 20% in Figure 3.2. This indicates that the fit to the SAOSF data is only marginally better with four pairs of modes (Figure 3.4) than with only two pairs (Figure 3.2). It is definitely not as good as the six-mode fit in Figure 3.3, where the RMS error was 6%. Furthermore, in Figure 3.4, we also observe some small waves or fluctuations in the model description of the modulus that do not appear in the experimental data. The reason for both of these artifacts is due to the fact that the fit in Figure 3.4 was obtained using more experimental data than the fit in Figure 3.2. Hence, the additional mode pairs for $N = 4$ were required to fit relaxation modes outside of the dynamical range excited by the SAOSF. (Notice, for instance, that the shear-viscosity data of Figure 3.5 span seven orders of magnitude in applied shear rate.) Additionally, even some of the original six modes used in the SAOSF fit of Figure 3.3 had to be pulled outside of that frequency range to fit the additional data.

Also in Figure 3.4, there is no noticeable difference between model Result_1 and Result_2. The relative RMS error for Result_2 is 16%, compared with 16% for Result_1. This indicates that at least one mode in the MCMM Model with $N = 4$ is redundant,

implying that the mode to which it is coupled acts in a virtually independent manner. Thus we could just as accurately use a MCMM Model with three pairs of modes instead of four, and one independent UCMM for the seventh mode. Other modes with relatively small values for the mode concentration, n_i, could also be eliminated similarly.

It is instructive to compare the relaxation spectrum of Table 3.3 with that of eight uncoupled Maxwell modes, which can be computed by letting the four coupling parameters vanish and fitting to the SAOSF data only. This uncoupled spectrum is presented in Table 3.4. Note that in this case, the fit of the data is very good, even better than the six-mode case depicted in Figure 3.3 (although the graph is not shown here). Comparing the relaxation time spectra of Tables 3.3 and 3.4, several interesting features emerge. First, the uncoupled spectrum spans a much smaller range of relaxation times. This is to be expected since no nonlinear data was considered in the optimization fit leading to the parameter values displayed in Table 3.4. Thus relaxation times not excited in the SAOSF experiment are not considered in the fit. Upon consideration of the nonlinear data, some of these relaxation times must be pulled out of the window of the SAOSF experiment. Second, the largest relaxation time of the uncoupled spectrum is several multiples of the largest relaxation time of the coupled spectrum. This is explainable due to that fact that, as mentioned earlier, the characteristic time scales of a rheological experiment (in this case, the false, uncoupled spectrum) can be quite different than the relaxation time constants inherent to the material under investigation (in this case, the true, coupled spectrum) [3.6]. Indeed, according to Ref. [3.6], the longer characteristic time of a pair will be significantly larger than its associated relaxation time constant.

The above discussion illustrates the dramatic consequences ensuing from the neglect of mode coupling, should it actually occur. If one assumes uncoupled modes, the relaxation time constant spectrum obtained from an optimized fit to SAOSF data can be drastically different from the one obtained allowing for coupling between the modes. Of course, the issue then reduces to determining whether or not the modes do actually couple, and to what degree. This question can only be answered by examining nonlinear data, since, as mentioned earlier, the coupling only manifests overtly in nonlinear experiments. If mode coupling can explain dynamical trends observed in nonlinear data when uncoupled-modes models cannot do so, then this is a good indication that mode coupling is actually occurring.

3.6.2 The Steady-State Behavior

In Figure 3.5, we plot the experimental data and model fit of the steady-state shear viscosity as a function of shear rate. The experimental data were obtained using the ACER at high shear rates, and the ARES at low shear rates. Data at intermediate shear rates were inferred from the dynamic viscosity measurements made during the SAOSF experiment. At the highest values of shear rate, there is a strong possibility that viscous heating could be corrupting the measurements. Fortunately, the dynamic viscosity data overlap the ACER data up to shear rate values of $100s^{-1}$; this gives us an indication that, up this point, viscous heating is not occurring. For higher values of the shear rate, we have no conclusion about whether or not viscous heating could have been playing a role in the rheological response.

The MCMM Model parameters used in this figure and in all remaining figures in this work are the same as those used in Figure 3.4 (see Table 3.3). The MCMM Model fit is, qualitatively and quantitatively, fairly accurate at low and intermediate shear-rate values. The relative RMS error is approximately 20%. We still observe abnormal fluctuations in the curve as a result of the unnatural limitations of pair-wise coupling and Maxwell relaxation modes. This problem can be corrected (with fewer modes!) by either allowing full coupling between modes, or by incorporating nonlinear relaxation mechanisms into the MCMM Model [3.16].

In Figure 3.6, we plot the experimental data and model fit for the first normal stress difference as a function of shear rate. The experimental data for the first normal stress difference is available from the ARES at low shear rates only. In this shear-rate range, the fit is reasonable, with a 24% relative RMS error. Figure 3.6 displays similar waves, again due to the limitation of pair-wise coupled Maxwell modes.

We have no experimental data for the second normal stress difference; however, the MCMM Model offers us the opportunity to make a prediction of this rheological characteristic function. The predicted value of the ratio of the second and first normal stress differences takes the value –0.106 at low shear rates, and is practically constant over the range of shear rates where the first normal stress difference was measured experimentally. We have no way of knowing if this prediction is correct, however, the value cited is very reasonable based on experiments with other polymer melts.

3.6.3 Transient Uniaxial Extensional Viscosity

In Figure 3.7, we display the elongational viscosity as a function of time for different elongational rates. We also check Trouton's viscosity rule, which states that the limit of the elongational viscosity at low elongational rates is three times the zero shear-rate viscosity, η_0. Figure 3.7 shows that the general trends of the model are consistent with the experimental data. We see that (i) the elongational viscosity strictly increases with time, (ii) that as the elongational rate increases, the slope of the elongational-viscosity curve increases, and (iii) that the Trouton's Rule is obeyed extremely well.

There is, however, one difference between the theoretical and experimental results, especially in the case of higher elongational rates. First, the theoretical elongational viscosity predicted by the MCMM Model increases more steeply with time than does the experimental data. This discrepancy is due to the fact that Maxwell modes are capable of infinite elongation, which is an approximation that becomes more pronounced at longer times. This approximation results in huge relative RMS errors. In Figure 3.7, the RMS error is about 16400%. Despite this large error, we feel that the qualitative nature of the fit is important. As mentioned in Section 4, this data was taken using the ACER with semi-hyperbolically converging dies. According to Ref. [3.8], this data must be shifted to the left in Figure 3.7 due to entrance effects associated with these dies. The problem is, we do not yet know how much to shift the data. Ongoing research extraneous to this project is attempting to address this issue. In the meantime, therefore, we do not place much emphasis on quantitatively fitting the elongational viscosity, but remain intrigued by the reasonable qualitative behavior of the model as displayed in Figure 3.7.

3.6.4 Transient Shear Behavior

The parameters obtained for the MCMM Model by fitting the experimental data just discussed were used in unsteady shear flow to examine the transient experimental data. (As a reminder, the transient data was not included within the fitting of the parameters.) Figures 3.8-3.11 show the comparison of the results from the MCMM Model with the experimental data taken using ARES.

In Figures 3.8-3.11, we show the shear stress and first normal stress difference as functions of time for four transient experiments with steady-state shear rates of $0.07s^{-1}$, $0.1s^{-1}$, $0.5s^{-1}$, and $1.0s^{-1}$. In this experiment, a given shear rate is applied at time zero, and held constant until the shear stress and first normal stress difference have attained well-defined steady-state values. The shear rate is then set to zero, and the relaxational behavior is monitored. At the two lowest values of the shear rate, the experimental values of the first normal stress difference is prone to large errors as its absolute magnitude is a small fraction of the transducer response range. Consequently, a small amount of error in the transducer reading is a significant portion of the magnitude of N_1. The N_1 data at the higher values of the shear rate are quite monotonic.

At low shear rates, the theoretical predictions for the transient shear stress, Figure 3.8, are in good qualitative and quantitative agreement with the experimental data. The relative errors for the steady-state shear stress at these shear rates were 1.2% and 2.6%. The time required to reach steady state, and even the very slight overshoot for $0.1s^{-1}$, are described well by the model. Clearly, however, one (or more) long-time relaxation mode has not been accounted for, as evident from the discrepancy between the data and model at long times. These long-time relaxation modes are not excited during the SAOSF

experiments, and are only evident in the upper Newtonian plateau in the steady shear experiments. Consequently, they are not obtainable by fitting the SAOSF data, and get washed out of the Newtonian plateau from the steady-state viscosity fitting due to the fact that several modes can contribute to the plateau value of the viscosity. Thus one cannot distinguish the long-time modes from the data used to fit the parameters.

At the intermediate shear rates shown in Figure 3.9, the steady-state model values are not very close to the experimental values, with RMS errors of -20% and 24% in order of increasing shear rate. The time required to reach steady state is still the same in the model as in the experiments, but, again, at least one long-time relaxation mode has not been accounted for. Most annoying, however, are the oscillations that appear in the shear stress at these intermediate shear rates. This explanation of this behavior is offered in Section 3.7, below.

The transient first normal stress difference (N_1) data was also predicted using the MCMM Model. The same shear rates as in case of the shear stress data were used here. As seen in Figure 3.10, at low shear rates the MCMM Model offers good predictions overall, both qualitatively and quantitatively, except for the long-time relaxational behavior. The relative errors for the first normal stress difference for the steady-state shear rates examined were -3.9%, -8.4%, 7.2%, and -2.4% in order of increasing shear rate. In the case of intermediate shear rates, shown in Figure 3.11, a similar problem of damped oscillations is observed in the start-up of the experiment.

3.6.5 The Minimum Essential Experimental Data

Apparently, we can obtain consistent results through fitting four types of data: the complex modulus, steady-state shear viscosity, steady-state first normal stress difference, and transient uniaxial elongational viscosity. The question then arises as to what is the minimum amount and types of data necessary to fix the model parameters. This is not so easy to answer at this point, since we obviously have not yet examined enough model types. Thus, more detailed work to follow [3.16] will allow a more fulfilling answer to this question than is offered below. Nevertheless, we can get some idea about this issue by examining more closely the case studied thus far.

In Table 3.5, we list the experiments that we used to fit the model parameters. The result labeled No. 3 is our global minimum obtained by fitting four types of data stated before; although we cannot guarantee that it is the absolute global minimum with the NMDSM. The parameters for Result No. 3 are given in Table 3.3. These parameters were used as the initial guess in the optimization for Results Nos. 1 and 2, but excluding the indicated type of experimental data from the fitting. Result No. 1* was obtained by fitting only the indicated data, but using a random initial guess, as opposed to Result No. 1. The parameters from Result No. 1 were then used as the initial guesses for obtaining Results Nos. 2* and 3*.

In Table 3.6, we list the relative errors corresponding to Table 3.5. If we compare the results between Nos. 1, 2, and 3, there is practically no difference, suggesting that there is a consistency in the MCMM Model among complex modulus, shear viscosity, first normal stress difference, and elongational viscosity. Our final "global minimum" of No. 3 exists at least as a local minimum of Nos. 1 and 2. We could not tell whether it

exists as a global minimum of Nos. 1 and 2, due to the crude nature of our optimization technique. Comparing between Result Nos. 1*, 2*, and 3*, it is seen that by starting with less experimental data, only slightly worse model descriptions are obtained, although the elongational viscosity paradoxically improves. (The absolute value of the RMS error associated with this viscosity is so high, however, that this apparent paradox is meaningless. Again, the large error in the elongational viscosity might be due to the time shift from the ACER experiment, discussed above and in Ref. [3.8]).

From these arguments, initial evidence suggests that the minimal amount of experimental data necessary to fit the model parameters includes: SAOSF data over a wide range of frequencies for intermediate-time relaxation modes, steady-state viscosity measurements at high values of shear rate for small-time relaxation modes, and transient shear relaxation for long-time relaxation modes. With this minimal set of experimental data, all easily obtainable, we hope in the future to obtain quantitative model descriptions of other rheological behavior in more complicated experiments and with better rheological models.

3.7 Analysis of the modal contributions of the rheological behavior

Several unnatural features of the MCMM Model results described in the preceding section can be rationalized by examining the dynamical behavior of the individual modes, which superimpose to provide the overall system response. The first unnatural feature is the sinusoidal nature of the theoretical curve in Figures 3.5 and 3.6, associated with the steady-shear behavior of the shear stress and first normal stress difference. The second is the oscillatory behavior of the transient start-up behavior of

these same two quantities. Finally, there is an unnatural waviness to the SAOSF model results presented in Figure 3.4. We examine in this section each of these cases in turn, and reach some tentative conclusions about the origins of these phenomena, but total clarity will not be achieved until we remove the restriction of Maxwell-type relaxation behavior in subsequent work [3.16].

Before we begin this examination, it is necessary to understand the behavior of the uncoupled Maxwell modes model under these same circumstances. For the steady-state properties, the predictions of the eight uncoupled Maxwell modes model is that the shear viscosity is independent of shear rate, as is the first normal stress coefficient. This prediction is quite bad. For the SAOSF experiment, the prediction is essentially that presented in Figure 3.3, but with even less RMS error than the six-mode case presented there. This prediction is quite good. In particular, there is no sign of any waviness to the model predictions. For the transient shear behavior, the stress rises monotonically to its steady-state value, and remains there until flow cessation, at which point it decays monotonically back to zero. This prediction can be good or bad, depending on whether or not the experimental shear stress displays an overshoot at the particular value of the shear rate under investigation. Our task now is to understand why the MCMM Model predictions are different from those just described. It is instructive to examine this issue with reference to the dimensionless mode stress tensor evolution equations of Eq. (3.5).

3.7.1 The Steady-State Behavior

In Figure 3.12, we have broken down the composite shear viscosity versus shear rate curve of Figure 3.5 into the contributions from each mode, and each pair of modes. The parameters of the MCMM Model corresponding to these modes are given in Table 3.3. This figure explains why we observe the unnatural sinusoidal behavior evident in Figure 3.5: it is a direct result of the use of Maxwell modes in the model. The model contains no inherent shear-thinning behavior in any one of its modes—recall the steady-state prediction of the uncoupled Maxwell modes model (constant viscosity). Consequently, the only way that the model can display a shear-thinning behavior is by having non-vanishing values of the coupling parameters, θ_i.

In order to fit the shear-thinning experimental data of Figure 3.5, one of each pair of mode stresses must be set orders of magnitude smaller than the other. Then each mode of a given pair has its own shear viscosity value, but only the larger one contributes directly to the measurable viscosity of Figure 3.5, while the other one is negligible. This then allows the coupling parameter to describe the shear-thinning region between the large and small stress values. In order to make one mode stress orders of magnitude smaller than its conjugate, it must have a mode concentration that is orders of magnitude smaller than its conjugate. Recall from Eq. (3.5) that, when one concentration value is much greater than its conjugate, the smaller concentration mode affects the stress of the larger concentration mode, but not vice versa. Hence the greater mode viscosity value in each case of Figure 3.12 shows shear thinning, while the lesser mode viscosity value is constant. This is not true for Pair 4, as displayed in Figure 3.12d, where both viscosities

are constant, but in this case, Table 3.3 reveals that the corresponding coupling parameter value is approximately zero; thus both modes behave as uncoupled Maxwell modes.

This explains why the composite theoretical prediction displayed in Figure 3.5 shows the unnatural sinusoidal behavior. It is a direct result of the use of Maxwell modes in the MCMM Model. Had more reasonable modes been assumed that allowed for nonlinear behavior such as shear thinning even in the uncoupled model, this problem would not have arisen—see Ref. [3.16] for more proof.

3.7.2 Oscillatory Shear Behavior

Now we must explain why the SAOSF curve of Figure 3.4 shows the unnatural waviness apparent there, whereas the uncoupled Maxwell modes of Figure 3.3 do not. The reason for this is tied up with the reasoning of the preceding section. Recall that Figure 3.4 was produced while fitting the steady-shear viscosity data at the same time as fitting the SAOSF data, whereas Figure 3.3 was produced fitting only the SAOSF data. In order to obtain a reasonable fit of the steady-shear data, i.e., to obtain shear thinning of the viscosity, it was necessary in the MCMM Model to have one mode stress of each pair be orders of magnitude smaller than the other one. Because of this, the optimization program is fitting in reality only four modes to the SAOSF data, because the other four are contributing negligible amounts to the complex modulus. Hence the eight-mode prediction of Figure 3.4 is essentially no better than the four-mode coupled or uncoupled fit of Figure 3.2. Thus the waviness in the SAOSF curve predicted by the eight-mode MCMM Model is also directly attributable to the linear nature of the Maxwell modes.

3.7.3 Transient Shear Stress Behavior

The last question is with regard to the cause of the oscillations in the transient shear stress response exhibited at intermediate shear rates in Figures 3.9 and 3.11. The behavior of each of the eight modes, and for all four pairs, is displayed in Figure 3.13. As evident, only one mode of each pair contributes meaningfully to the shear stress, since the concentrations of the two modes differ by many orders of magnitude, except for the fourth pair where the coupling parameter is so small that the modes are effectively uncoupled—see Table 3.3. As seen in Figure 3.13, only one mode causes all of these oscillations. Inspecting the parameter values of Table 3.3, it is evident that the difference in modal concentrations of each pair cannot be the entire cause of this phenomenon. The difference between the behavior of Pair 2 and Pairs 1, 3, and 4, is that the ratio of the relaxation times for Pair 2 is on the order of 10^4, whereas for the remaining pairs it is only at most of order 10^2.

The problem with Pair 2 is apparent again from an examination of Eq. (3.5). The smaller stress mode of Pair 2, with the smaller concentration value, has also the smaller relaxation time. According to Eq. (3.5), this mode receives little effect then from the larger stress mode. The contribution to the smaller stress mode's evolution equation from the larger stress mode is negligible, and its own contribution is amplified. Hence the evolution equation for the smaller stress mode is like an uncoupled Maxwell mode. However, the evolution equation for the larger stress mode receives an augmented contribution from the smaller stress mode, and a reduced contribution from itself. Due to this double effect, the evolution equation for the larger stress mode is so severely

constrained that a complex interplay is forced between these two contributions, since they become of comparable magnitude but opposite effect.

Again, the linear behavior of the aphysical Maxwell modes is to blame for this behavior. Due to the fitting of the steady-state shear data, i.e., with one concentration value necessarily much greater than that of the conjugate mode, such a complicated transient behavior can become a factor in the analysis (if the ratio of the relaxation times of the two modes is lopsided in the same direction as the concentration ratio of the two modes). Thus the only way to avoid such unnatural occurrences in data fitting and predicting polymeric fluid rheological behavior seems at this point is to use more realistic modal behavior that goes beyond simple Maxwell modes. Full coupling, as opposed to pair-wise coupling, might also help to alleviate some of the difficulties described above [3.16].

3.8 Summary

The discussion above indicates that the MCMM Model, limited to pair-wise coupling between modes, can describe some of the many aspects of polymer melt rheology. The MCMM Model displays a consistent fitting of the data for the complex modulus, shear viscosity, first normal stress difference, and elongational viscosity, although some of this fitting has unnatural characteristics caused by the incorporation of unrealistic Maxwell modes. There are still unknown points to explore. Primarily, the restriction to pair-wise coupling and Maxwell-type relaxation behavior prevents us from using as few modes as possible to describe our system. This restriction also leads to the

strange oscillations observed under some conditions. Also, what is the benefit of replacing Maxwell modes with FENE-P modes or a more realistic nonlinear relaxation behavior? Future work will be directed at examining the data prediction capabilities of a whole range of viscoelastic fluid models under similar circumstances as presented herein.

Acknowledgements

The authors are very grateful to Dr. Kurt Wissbrun for sharing his knowledge of optimization methods for linear viscoelasticity data with us, and for performing the initial calculations with these methods. Drs. Simhambhatla and Leonov are also appreciated for allowing us to use their Padé-Laplace program *PADLAP*. Financial support was provided by the Chemical Engineering Department at The University of Tennessee.

References

3.1 A.N. Beris, B.J. Edwards, *Thermodynamics of Flowing Systems*. Oxford University Press, New York, 1994.

3.2 T.C.B. McLeish, R.G. Larson, *J. Rheol.* 42 (1998) 81-110.

3.3 H.C. Öttinger, *Rheol. Acta* 40 (2001) 317-321.

3.4 C.D. Chodankar, J.D. Schieber, D.C. Venerus, *J. Rheol*. 47 (2003) 413-427.

3.5 W.H. Press, S.A. Tevkolsky, B.P. Flannery, *Numerical Recipes in Fortran 77*. Cambridge University Press, Cambridge, 1992.

3.6 B.J. Edwards, A.N. Beris, V.G. Mavrantzas, *J. Rheol*. 40 (1996) 917-942.

3.7 B.J. Edwards, D.J. Keffer, C.W. Reneau, J. Appl. Polym. Sci. 85 (2002) 1714-1735.

3.8 K. Feigl, F.X. Tanner, B.J. Edwards and J.R. Collier, *J. Non-Newtonian Fluid Mech.,* 115 (2003) 191-215.

3.9 J. Honerkamp, *Rheo. Acta* 28 (1989) 363-371.

3.10 M Simhambhatla, A.I. Leonov, *Rheol. Acta* 32 (1993) 589-600.

3.11 N. Orbey, J.M. Dealy, *J. Rheol.* 35 (1991) 1035-1049.

3.12 R. Fulchiron, V. Verney, P. Cassagnau, A. Michel, P. Levoir, J. Aubard, *J. Rheol.* 37 (1993) 17-34.

3.13 W. Thimm, C. Friedrich, M. Marth, J. Honerkamp, J. Rheol. 43 (1999) 1663-1672.

3.14 L. He, R. Ding, A.I. Leonov, H. Dixon, R.P. Quirk, J. Appl. Polym. Sci. 71 (1999) 1315-1324.

3.15 K.F. Wissbrun, personal communication.

3.16 B. Jiang, D.J. Keffer, and B.J. Edwards, J. Appl. Polym. Sci., accepted in April 2004.

Appendix

Tables

Table 3.1: Parameter values for all modes (the TCMM and MCMM Models) used to fit only the data of complex modulus.

Model	No. of Pair	λ_i (sec)	λ_j (sec)	n_i (mol/m^3)	n_j (mol/m^3)	θ
TCMM	1	4.005E-01	7.188E-03	1.820E+01	4.594E-03	0.0
MCMM	1	1.960E-01	8.058E-03	3.761E+00	1.686E+01	0.0
	2	6.898E+00	1.544E+00	2.247E-01	3.049E-01	0.0

Table 3.2: Parameter values for fitting six uncoupled Maxwell modes to the complex modulus data according to the method of Ref. [3.10].

Mode No.	λ_i (sec)	λ_j (sec)	n_i (mol/m^3)	n_j (mol/m^3)
1,2	3.981E+01	7.586E+00	4.959E-03	1.781E-01
3,4	1.445E+00	2.754E-01	6.880E-01	2.208E+00
5,6	5.248E-02	1.000E-02	4.260E+00	1.441E+01

Table 3.3: Parameter values for all modes used to fit the data of complex modulus, shear viscosity, elongational viscosity, and first normal stress difference.

Model	No. of Pair	λ_i (sec)	λ_j (sec)	n_i (mol/m^3)	n_j (mol/m^3)	θ
MCMM	1	8.318E-05	5.854E-03	3.544E-16	2.651E+01	1.574E-09
	2	4.981E+00	2.462E-04	5.837E-01	1.178E-21	1.373E-09
	3	8.046E-04	2.520E-01	9.207E-19	4.532E+00	7.142E-10
	4	7.421E-03	2.010E-05	8.185E-01	2.514E-01	3.330E-14

Table 3.4: Parameter values for fitting eight uncoupled Maxwell modes to the complex modulus data according to the method of Ref. [3.10].

Mode No.	λ_i (sec)	λ_j (sec)	n_i (mol/m^3)	n_j (mol/m^3)
1,2	3.981E+01	1.218E+01	9.077E-03	6.680E-02
3,4	3.727E+00	1.141E+00	2.480E-01	7.269E-01
5,6	3.490E-01	1.068E-01	1.756E+00	3.708E+00
7,8	3.268E-02	1.000E-02	7.086E+00	1.247E+01

Table 3.5: List of data types that were included in the optimization fittings to determine the minimum amount of essential data necessary for obtaining the best parameter fit.

No.	Complex modulus	Shear viscosity	First normal stress difference	Elongational viscosity	Initial guess
1	Fitted	Fitted	Predicted	Predicted	See Table 3.2
1*	Fitted	Fitted	Predicted	Predicted	Method of Section 5
2	Fitted	Fitted	Fitted	Predicted	See Table 3.2
2*	Fitted	Fitted	Fitted	Predicted	Result from 1*
3	Fitted	Fitted	Fitted	Fitted	Method of Section 5
3*	Fitted	Fitted	Fitted	Fitted	Result from 1*

Table 3.6: RMS errors for the model predictions used to determine the minimum amount of essential data necessary for the best parameter fit.

	Relative root-mean-square (RMS) error (%)			
No.	Complex modulus	Shear viscosity	First normal stress difference	Elongational viscosity
1	15	20	23	16400
1*	19	24	30	8300
2	15	20	23	16400
2*	15	31	29	6300
3	16	20	23	16400
3*	15	31	29	6300

Figures

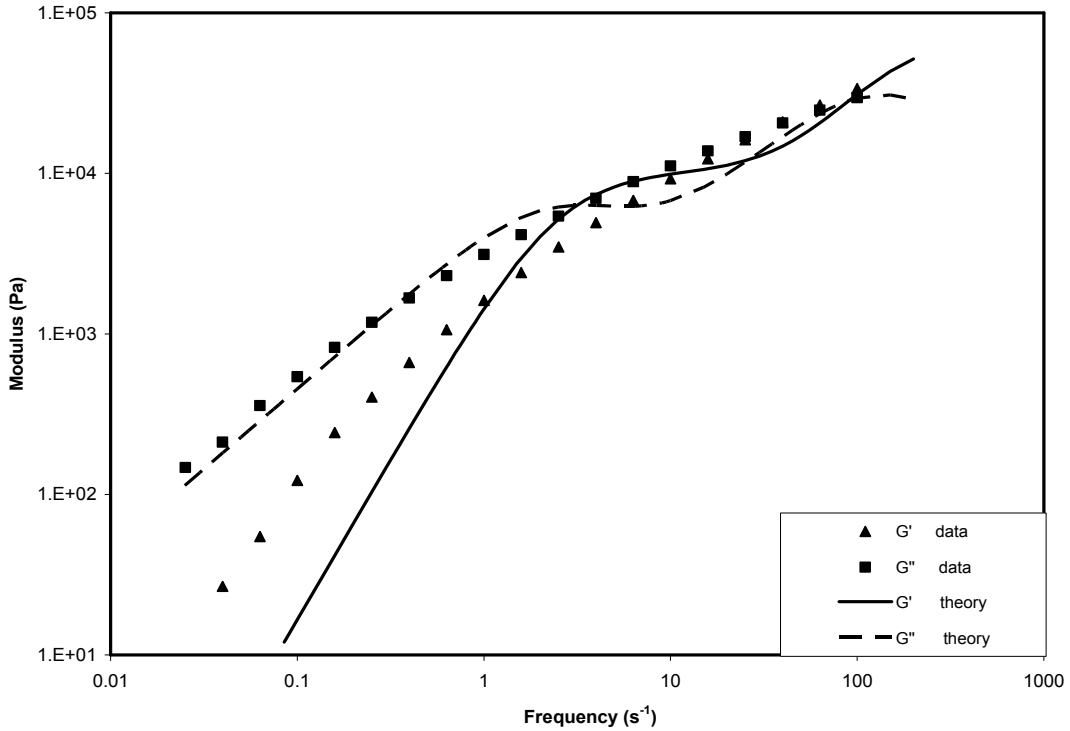

Figure 3.1: Complex modulus as a function of angular frequency, ω, fitted to the TCMM Model for a LDPE with $MW = 80{,}350\,\text{g/mol}$ at a temperature of $175^{\circ}C$.

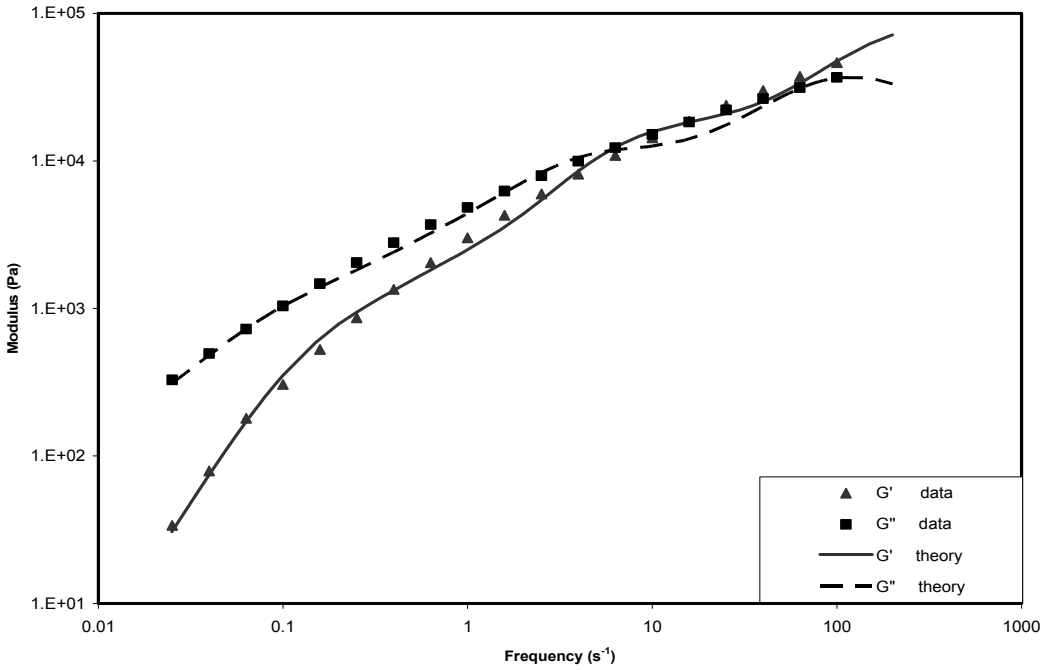

Figure 3.2: Complex modulus as a function of angular frequency, ω, fitted to the MCMM Model ($N = 2$).

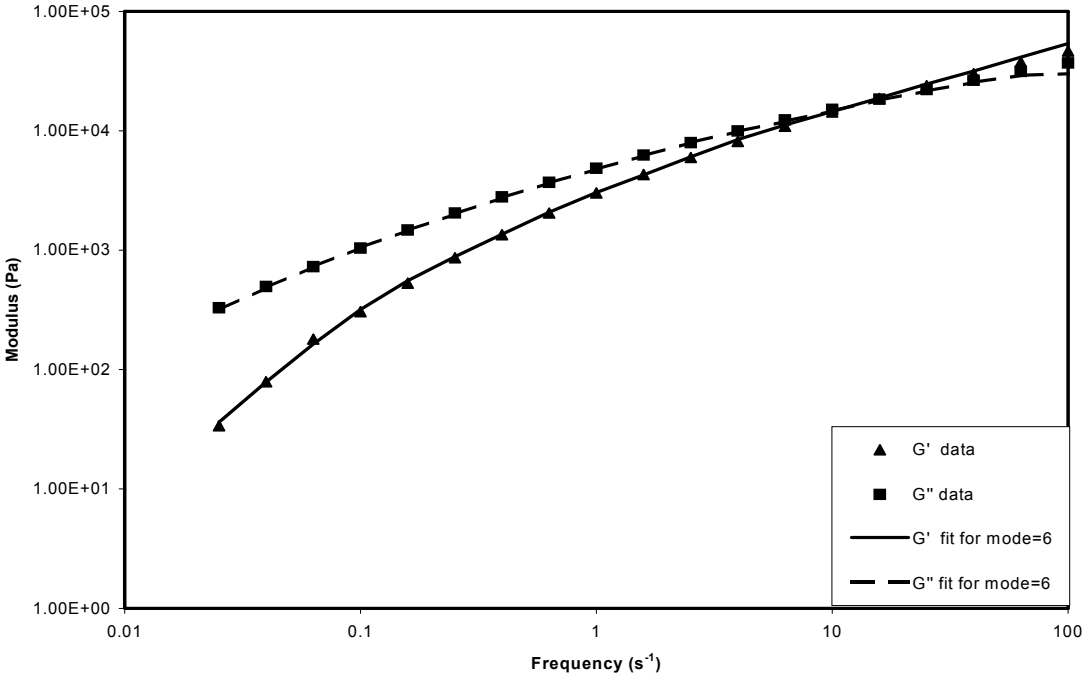

Figure 3.3: Complex modulus as a function of angular frequency fitted using six uncoupled Maxwell modes according to the method of Ref. [3.10].

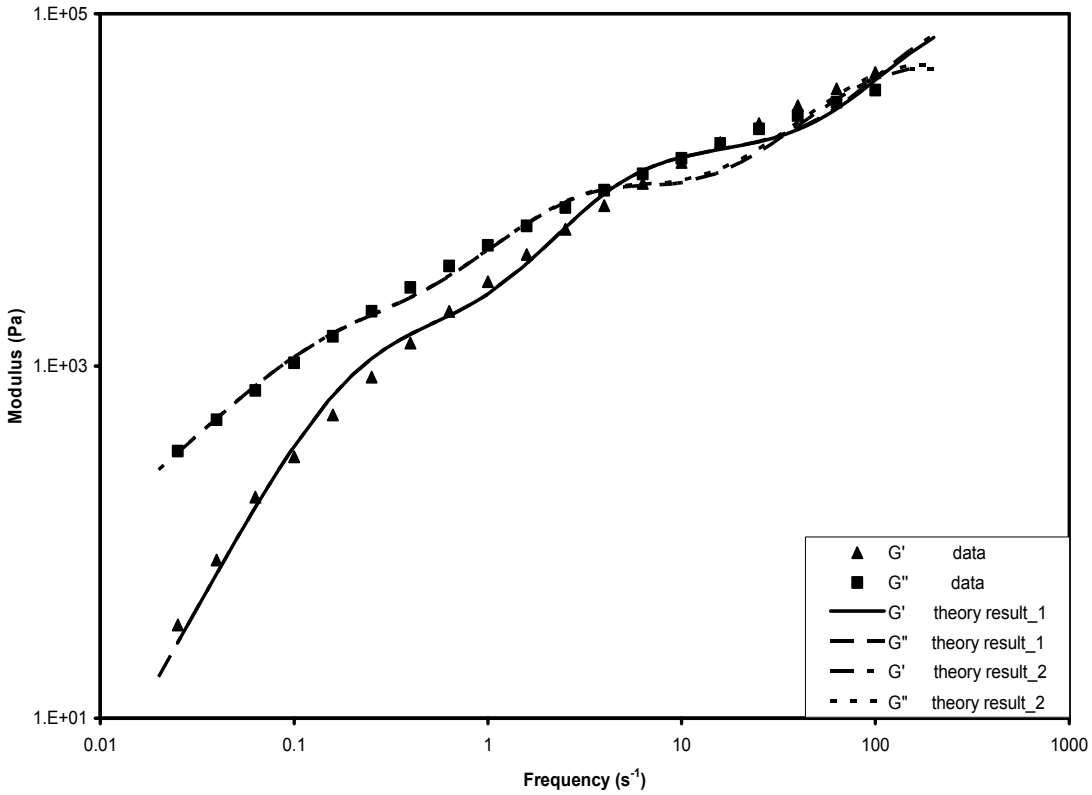

Figure 3.4: Complex modulus as a function of angular frequency, ω, fitted to the MCMM Model ($N = 4$) using four types of data for the LDPE melt.

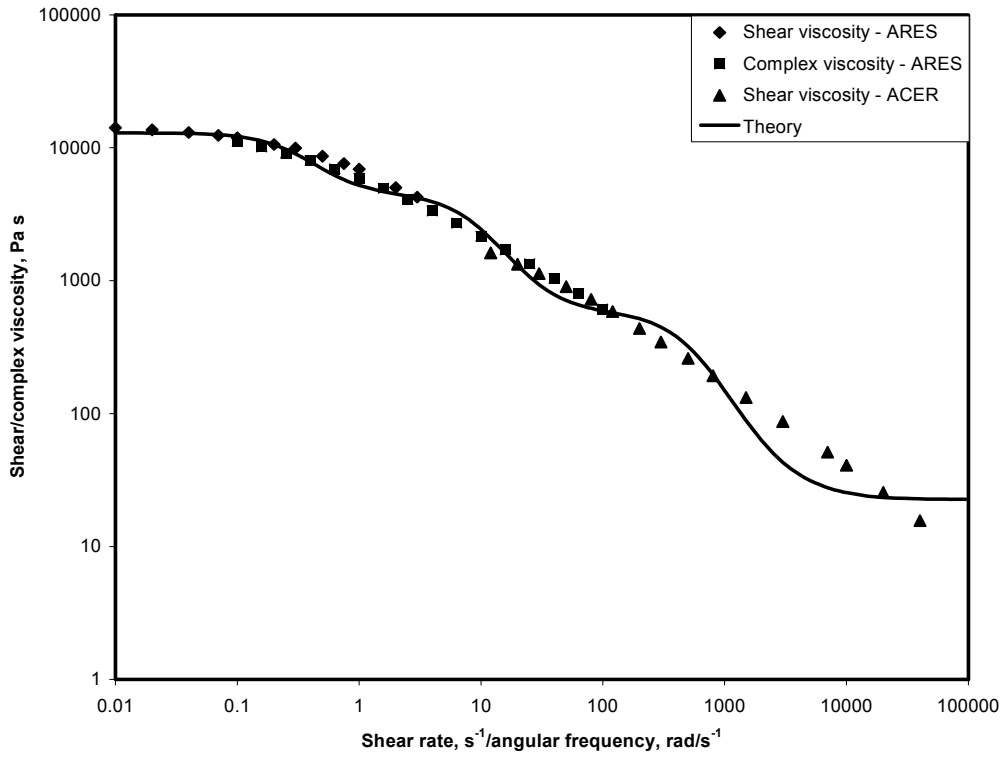

Figure 3.5: Steady-state shear viscosity versus shear rate, fitted to the MCMM Model ($N = 4$).

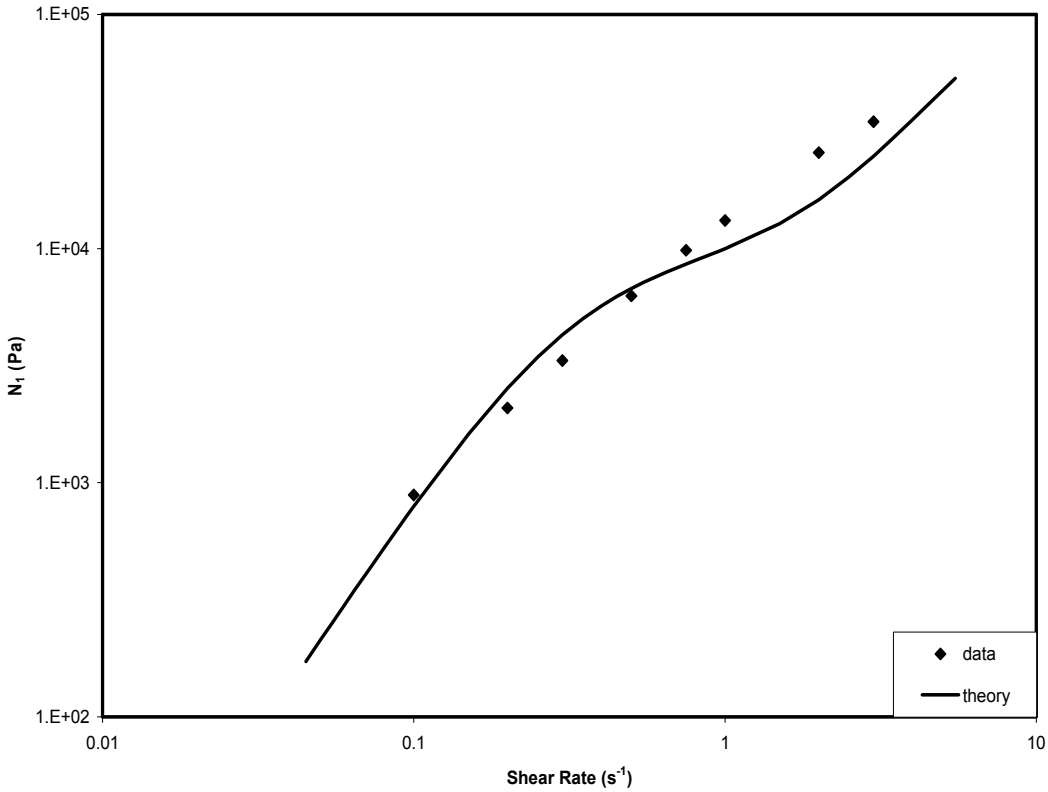

Figure 3.6: Steady-state first normal stress difference versus shear rate, fitted to the MCMM Model ($N = 4$).

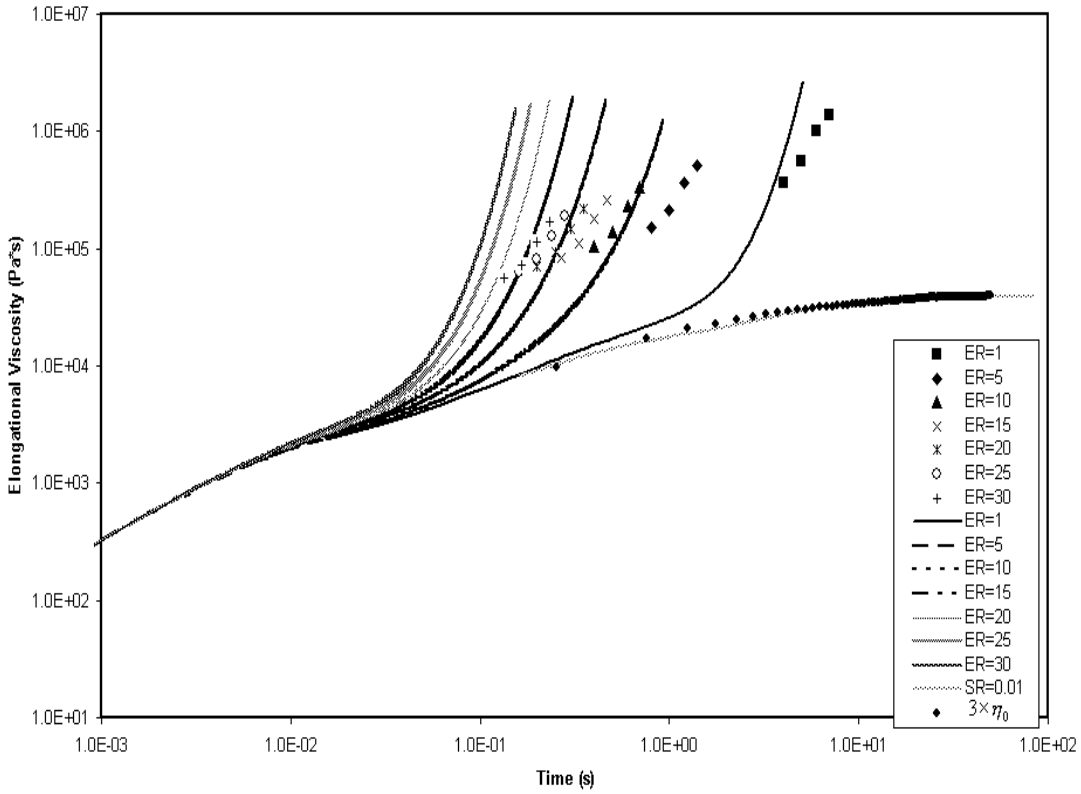

Figure 3.7: Elongational viscosity as a function of time, fitted to the MCMM Model ($N = 4$). "ER" refers to the strain rate, in units of reciprocal seconds.

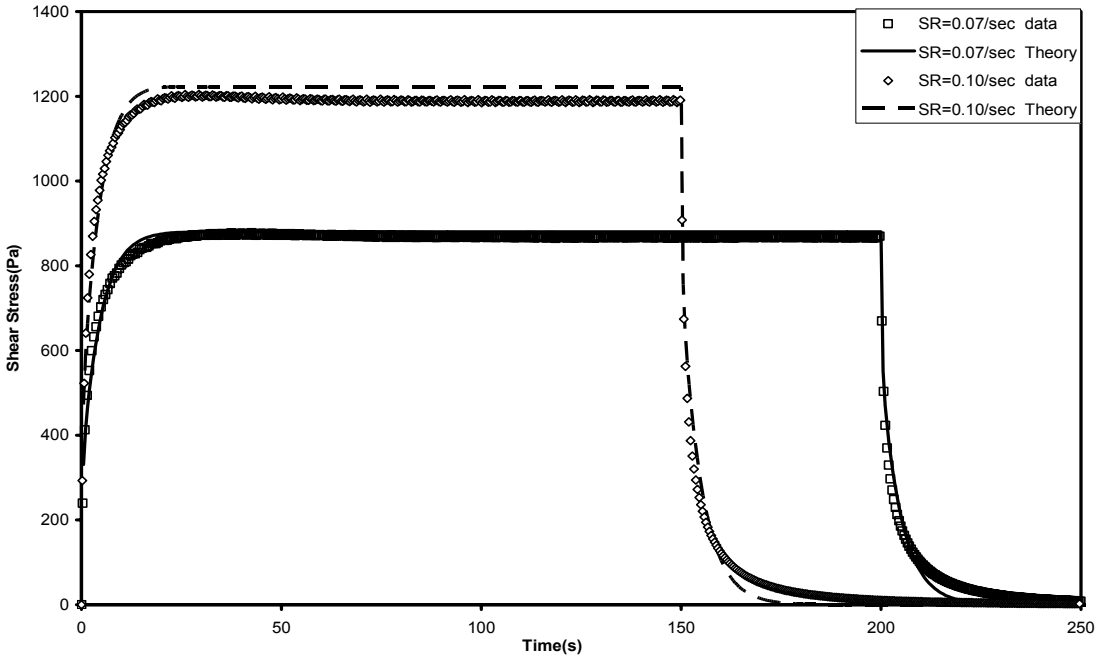

Figure 3.8: Transient shear stress as a function of time, predicted with the MCMM Model ($N = 4$) for the LDPE melt at shear rate 0.07 and 0.10sec^{-1}. "SR" refers to the applied shear rate.

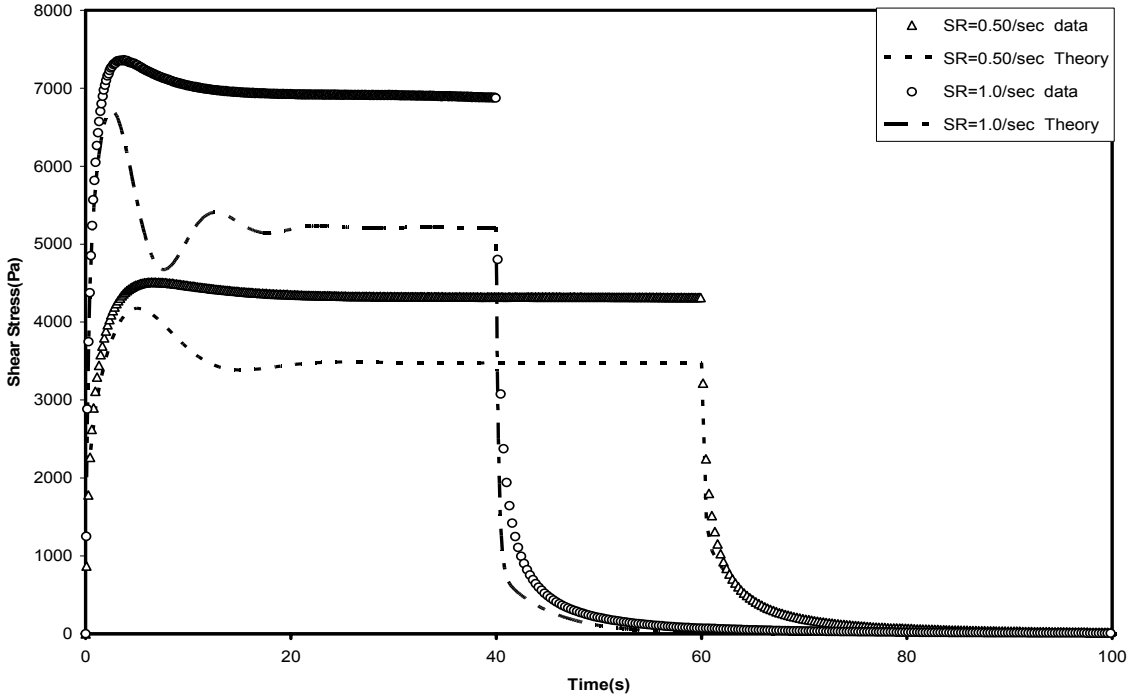

Figure 3.9: Transient shear stress as a function of time, predicted with the MCMM Model ($N = 4$) for the LDPE melt at shear rate 0.5 and 1.0sec^{-1}. "SR" refers to the applied shear rate.

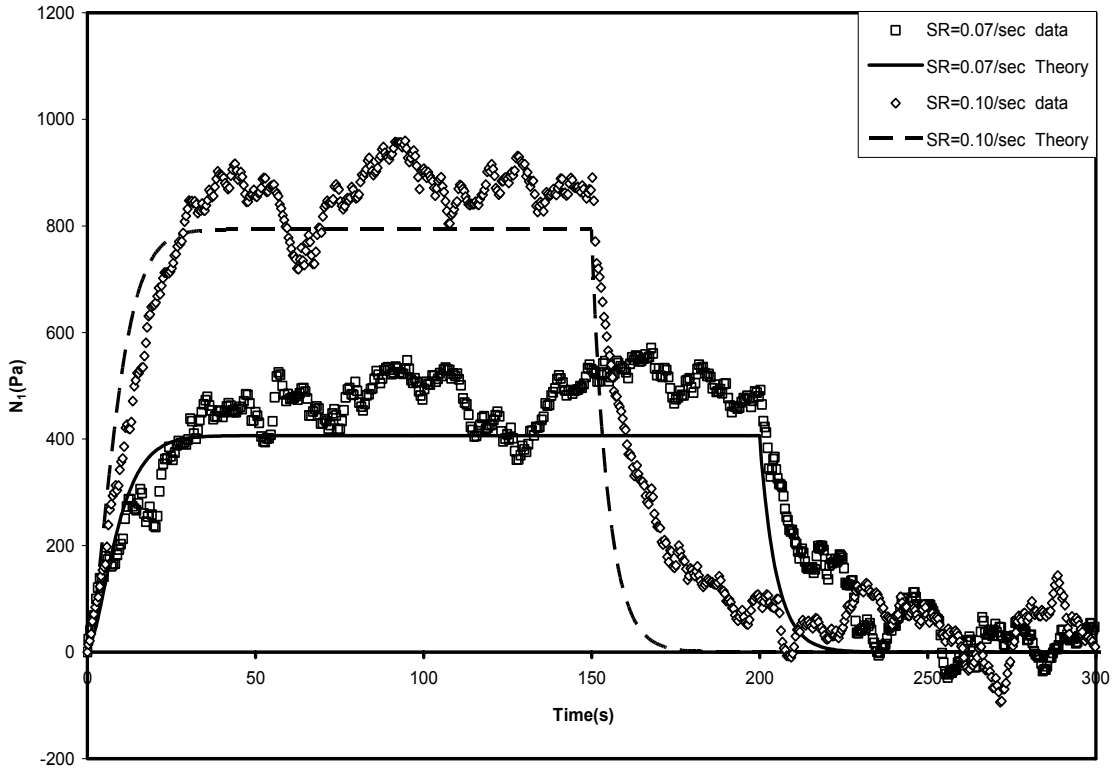

Figure 3.10: Transient first normal stress difference as a function of time, predicted with the MCMM Model ($N = 4$) for the LDPE melt at shear rate 0.07 and 0.1sec^{-1}. "SR" refers to the applied shear rate.

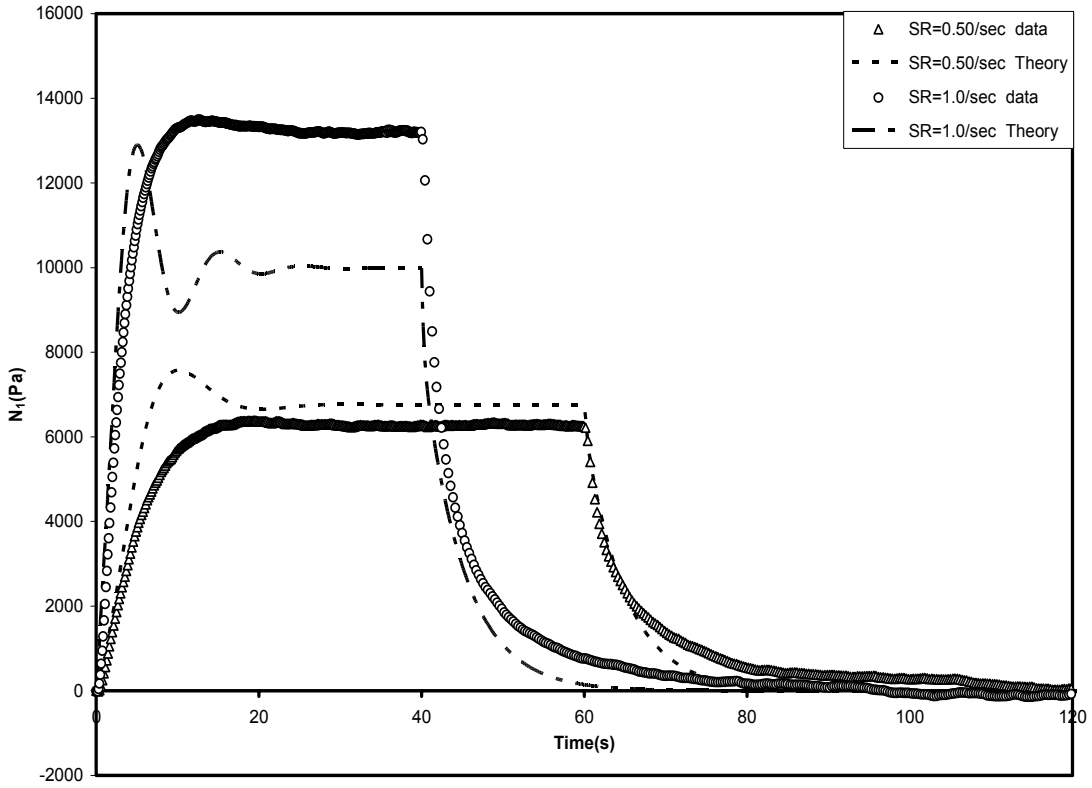

Figure 3.11: Transient first normal stress difference as a function of time, predicted with the MCMM Model ($N = 4$) for the LDPE melt at shear rate 0.5 and 1.0sec^{-1}. "SR" refers to the applied shear rate.

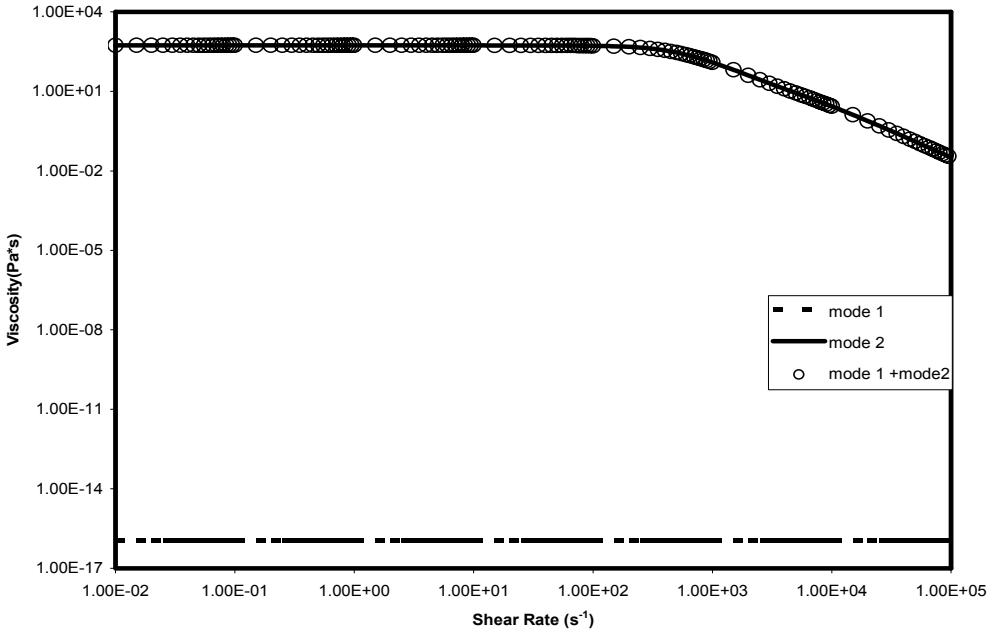

Figure 3.12: Plots of shear viscosity versus shear rate for each mode, and for each mode pair for the parameter values of Table 3.3: a) Pair 1.

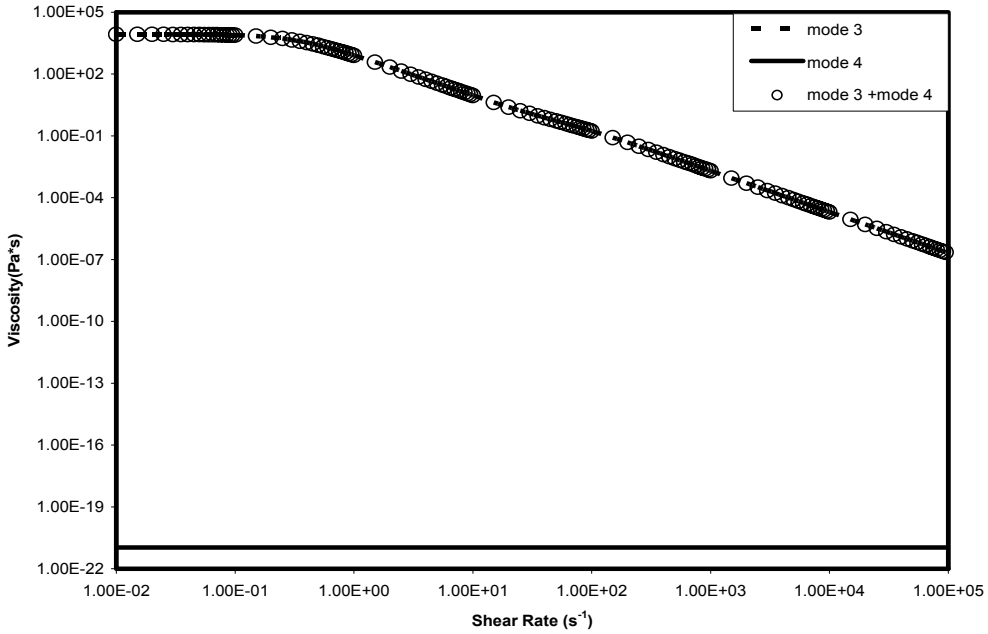

Figure 3.12: Continued b) Pair 2.

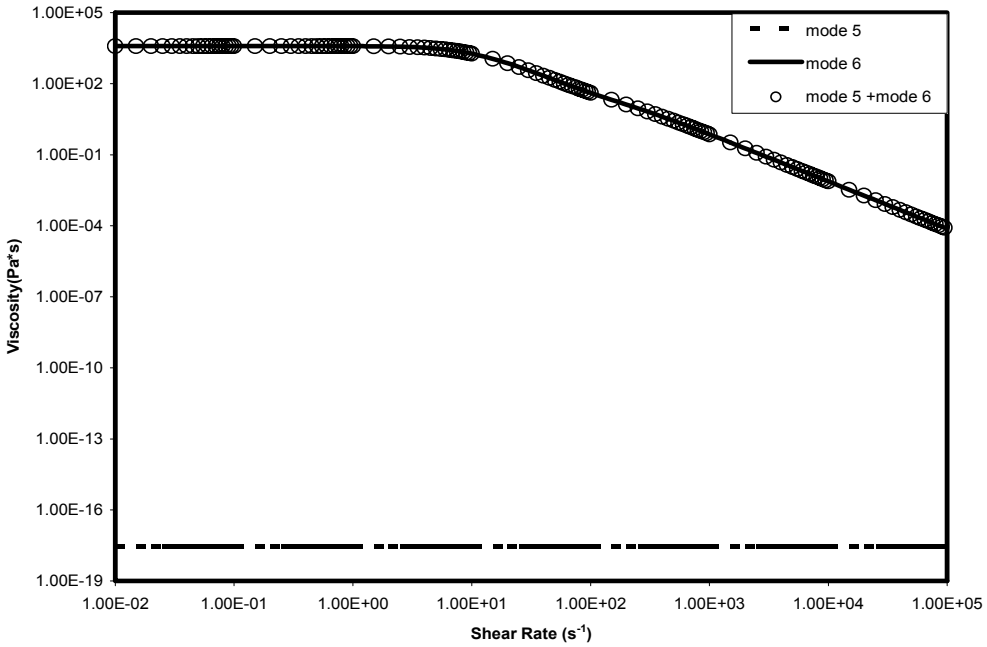

Figure 3.12: Continued: c) Pair 3.

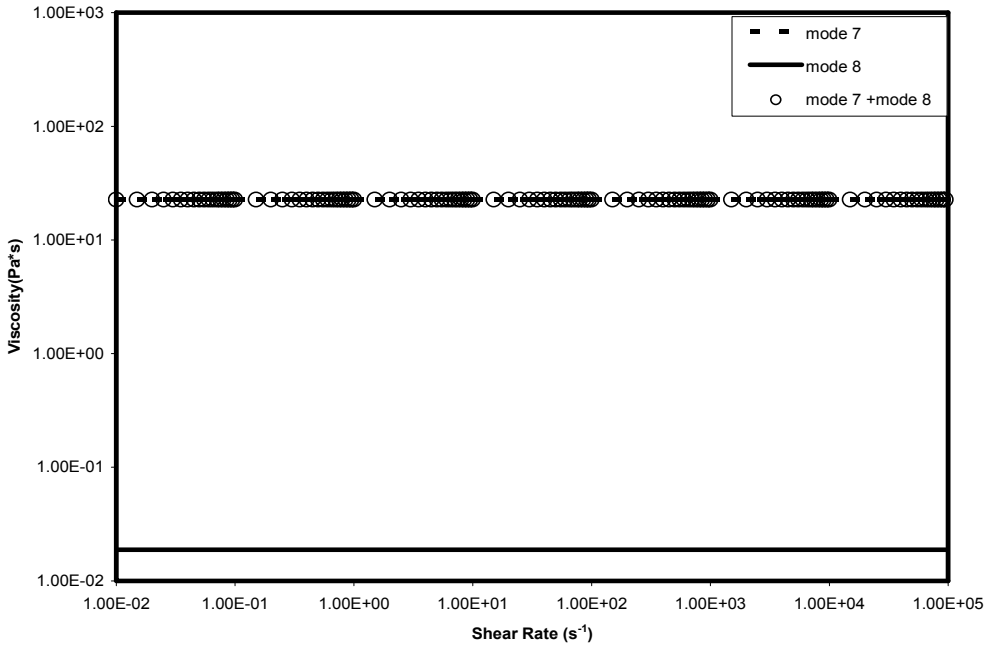

Figure 3.12: Continued: d) Pair 4.

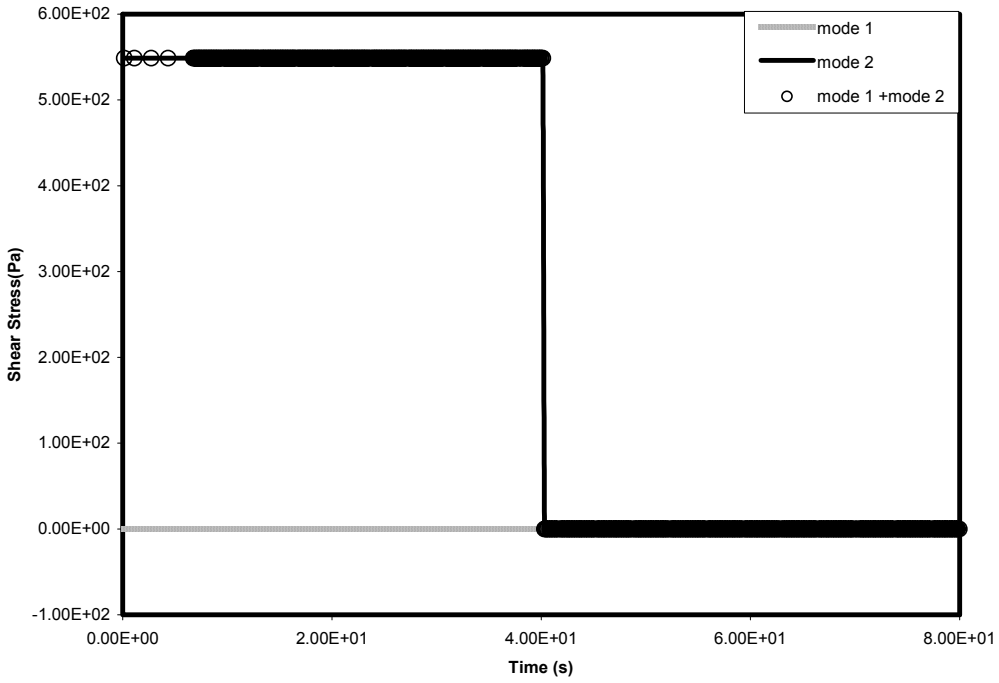

Figure 3.13: Plots of shear stress versus time for each mode, and for each mode pair at a shear rate value of 1 s^{-1} for the parameter values of Table 3.3: a) Pair 1.

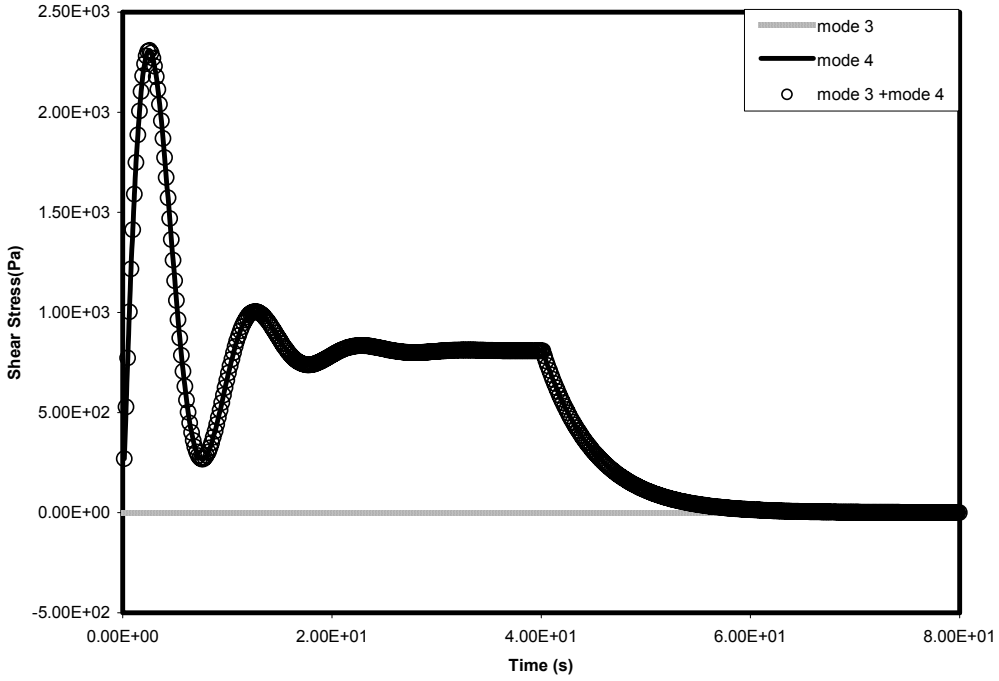

Figure 3.13: Continued: b) Pair 2

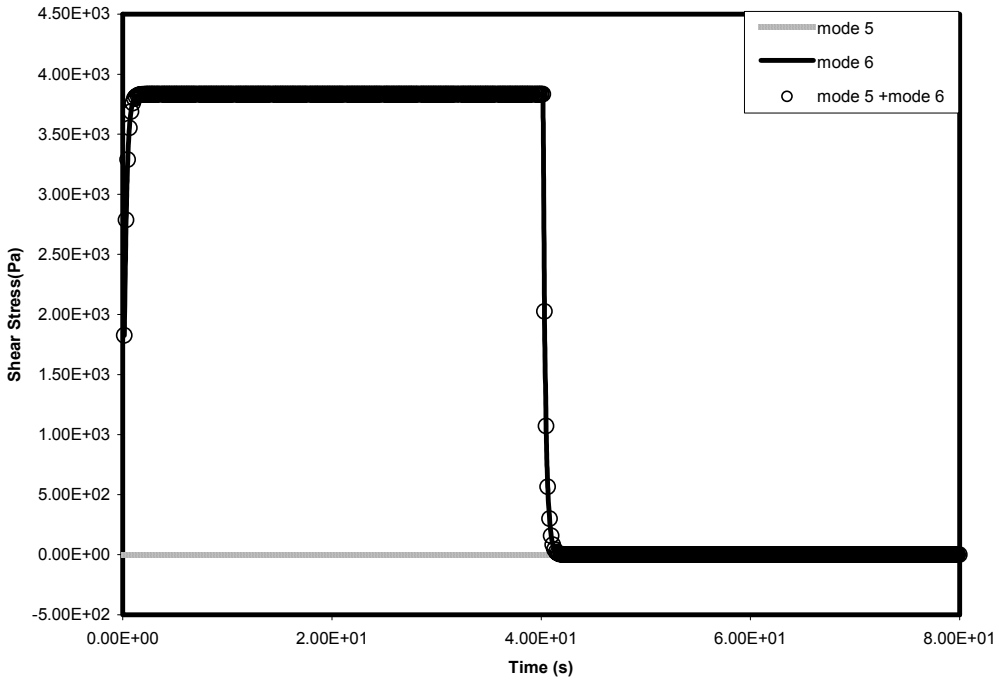

Figure 3.13: Continued: c) Pair 3.

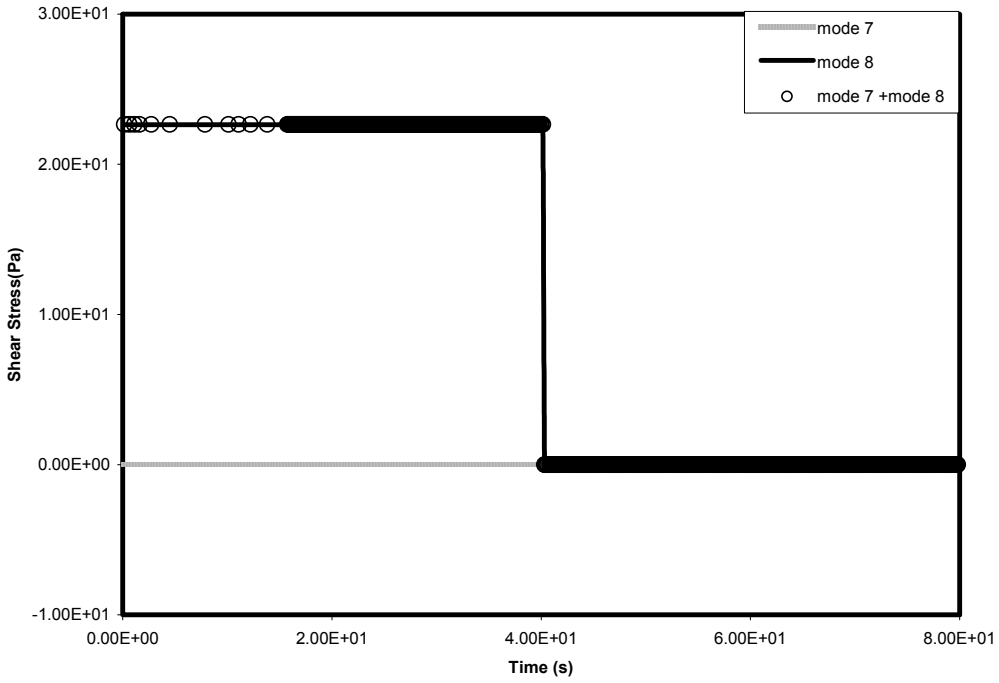

Figure 3.13: Continued: d) Pair 4.

PART 4

Using Multiple-Mode Models for Fitting and Predicting the Rheological Properties of Polymeric Melts

This part is revised slightly from a paper by the same name accepted by the "Journal of Applied Polymer Science" in April 2005, by Bangwu Jiang, Prajakta Kamerkar, David J. Keffer, and Brian J. Edwards.

In this part, "we" refers to my co-authors and myself. My primary contributions include: (1) development of the computational methods and model equations; (2) development of the data-fitting strategy; (3) all of the computational work and analysis; (4) most of the writing.

4.1 Introduction

For many years, one overall goal of theoretical rheologists has been to obtain a level of understanding of material behavior sufficient to allow for the prediction of viscoelastic properties in arbitrary flow fields. After approximately 75 years of effort spent in pursuit of this goal, it is still largely unachieved, even for isothermal cases. In recent years, modeling efforts have intensified as theoretical developments, such as reptation theory, mature, and as computational power has increased. It is now time to assess, in general terms, how close rheologists are to achieving this goal.

In this article, we offer a current assessment of the potential predictive capabilities of viscoelastic fluid models. Rather than focusing on the particular models popular today

(which might not be popular a decade from now), we examine instead semi-phenomenological models (i.e., models involving empirical parameters) that characterize a certain class of model types. This allows us to judge the capabilities of the class using the simplest possible methodology; i.e., without getting caught up in model-specific peculiarities and complexities. Suffice it to mention that all of today's popular models fall into one of the model classes examined herein, with one caveat: since we are examining polymer melts, which have a spectrum of relaxation times, we are only examining multiple-mode versions of viscoelastic fluid models. We see no point in trying to fit and predict nonlinear viscoelastic properties if the linear ones cannot be fit accurately. Since single-mode models are incapable of matching linear viscoelastic data from polymer melts in a quantitative fashion, it is apparent that we need only consider herein multi-mode versions of the chosen model classes.

The strategy of the research reported in this article is to fit the models examined herein to a limited amount of easily obtained experimental data of a typical polymer melt, and then to test how well each quantitatively predicts experimental data to which the inherent model parameters were not explicitly fit. The methodology used to fit the model parameters to the requisite amount of experimental data is now easily implemented using standard desktop computers. This methodology was described in detail in a prior publication [4.1], so only a brief summary will be included below. In the prior publication, only a single model class was examined, as the point of that article was to develop the methodology. Here, we wish to apply this methodology in order to draw more general conclusions.

The model classes examined in the succeeding sections are the following. The most basic semi-phenomenological model class is that of the uncoupled (i.e., no coupling between the various relaxation modes), linear relaxation models with constant relaxation times. The most well known and widely used of these is the multi-mode Upper-Convected Maxell Model, and thus we examine it herein. Of course, this model has no hope of fitting any nonlinear viscoelastic properties; however, we examine it as a basis for the linear viscoelastic response exhibited by many other models in the linear limit. The second class is that of uncoupled, linear relaxation models with variable relaxation times. Examples of models falling into this group are the Phan-Thien/Tanner Model [4.2], the Modified Upper-Convected Maxwell Model [4.3], and the Extended White/Metzner Model [4.4] (EWMM). Herein, we examine a version of the EWMM (as defined below) as an apt representation of this class. The third class is that of uncoupled, non-linear relaxation models. The example of this class studied herein is the most well-known model of this type, the Giesekus Model [4.5].

The remaining two classes of viscoelastic fluid models examined herein are those that involve coupled relaxation modes; i.e., the modes are no longer taken to be independent of each other, as was the case in all examples considered above. The first remaining class is that of the pair-wise coupled relaxation modes models; i.e., when each mode is taken to couple to one, and only one, other relaxation mode. The second remaining class is that in which each mode of a given model is allowed to interact with every other mode. Although it seems obvious that the first class is merely a special case of the second, we make the distinction between these two classes for the following reason: many recently developed viscoelastic fluid models were written in terms of two

relaxation modes, and these modes are coupled with each other. In order to fit experimental data, more than two modes are needed; hence, these models are generally duplicated the requisite number of times, thus producing a pair-wise coupled model. (As an example, the fitting capabilities of the Pom-pom Model [4.6-4.8] were investigated recently using 12 modes [4.9-4.10]. The multiple-mode version of this model falls into the class of pair-wise coupled modes with non-linear extensions—see below.) Obviously, this is just a special case of the more general fully-coupled models, but it is interesting to examine pair-wise coupling as an entity unto itself because this class possesses some striking peculiarities [4.1]—see below for more details. The models examined herein for both of these classes are the semi-phenomenological multiple-mode models introduced by Beris and Edwards [4.11]; these were chosen as the simplest possible representations of this class of models.

4.2 Literature overview

Of course, this is not the first study aimed at fitting and predicting rheological properties of polymeric fluids. One of the first and most extensive tests of rheological constitutive equations was that of Quinzani et al. [4.12], who examined the fitting capabilities of several multiple-mode rheological models (using 4 modes), including the Giesekus Model, for a vast array of experimental measurements of polyisobutylene solutions. Results of this study were encouraging for the future, but were limited by the simplicity of the models examined therein.

With regard to polymer melts, an international consortium has recently undertaken the task of matching experimental polymer processing flows to numerical

simulations [4.13]. Efforts with multiple-mode Giesekus and Phan-Thien/Tanner Models (with 4-9 modes) have yielded reasonable predictions of process flow characteristics [4.14-4.15]. As already mentioned, several investigations of the predictive capabilities of the Pom-pom Model (with 8-12 models) have also already been published, with impressive results [4.8-4.10].

4.3 Experimental data

All experimental data used in this investigation were taken using standard rheological testing equipment and procedures at the University of Tennessee. Results presented below are for a typical, industrially relevant, low-density polyethylene (LDPE) sample at $175°C$. The LDPE sample was obtained from Exxon, having been prepared using a Ziegler-Nata catalyst. It has a wide molecular weight distribution, with a value of the polydispersity index of 5.15. The value of the melt index was 0.2 g/minute, with a density of 0.923 g/cm^3. The weight-average molecular weight, according to gel permeation chromatography, was 80,350 g/mol.

A variety of experimental data were obtained, as described in a preceding article [4.1]. A dynamic frequency sweep was performed in the range of $0.01 s^{-1}$-$100\ s^{-1}$. From this, the storage modulus (G') and loss modulus (G'') data in small-amplitude oscillatory shear flow (SAOSF) were obtained. Shear viscosity data were taken over seven decades of shear rates ($0.01\ s^{-1}$-$100{,}000\ s^{-1}$). Steady-state first normal stress difference data covering a fraction of this shear-rate range were also obtained, along with transient shear stress data (start up and relaxation) and first normal stress difference data. Transient elongational viscosity measurements were made using four semi-hyperbolically

converging dies of Hencky strains 4, 5, 6, and 7, in the manner described in Ref. 16. We would expect this elongational viscosity data to be accurate for this particular polymer melt at this temperature and strain rate regime [4.17].

4.4 Optimization methodology

In order to place all models on an even footing, we take the number of modes used in each model as six. This number was chosen because it allowed a fit of the storage and loss moduli of the polymer melt used in this study to about 5% relative root-mean-square (RMS) error using the *PADLAP* program of Simhambhatla and Leonov [4-18]; thus we hypothesize (as rationalized below) that six modes should be sufficient for fitting most non-linear properties for this particular polymer melt as well. (See below for more details concerning the *PADLAP* fit to the experimental data.)

The overall optimization strategy of this investigation is to fit exactly six modes of a given model to the dynamic moduli (in SAOSF) and steady-state viscosity and first normal stress coefficient (in steady shear flow), and then to check whether the model predicts well the remaining experimental data. Each model examined below contains a definite number of parameters, which must be fit to the specified data set. The number of parameters fitted for each model investigated herein is listed in Table 4.1[3]. (See below for acronym definitions.)

For each model investigated, a set of coupled, ordinary differential equations (ODEs) quantifies the time evolution of the independent, non-vanishing elements of the mode stress tensors in homogeneous flow fields. For fixed values of the model

[3] All the table and figure are located in the appendix at the end of the part

parameters, a fourth-order Runge-Kutta method is used to solve the set of coupled ODEs. At steady state, the Newton-Raphson Method is applied to solve the resulting non-linear algebraic equations. For all models examined herein, the dynamic moduli in SAOSF can be calculated analytically.

The technique used to optimize the model parameters was the Nelder and Mead Downhill Simplex Method (NMDSM), which requires only functional evaluations, not derivative evaluations [4-19]. Although this optimization technique is not very efficient in terms of the number of functional evaluations and computational effort required, the NMDSM will always find a minimum, provided that one exists. However, the NMDSM is not guaranteed to find the global minimum, which creates a challenge for its users. Insight into the physical significance of the parameters and an understanding of the underlying physics is thus crucial to obtaining a good initial guess to the optimization problem. Multiple initial guesses are required in order to test whether the resulting minimum is indeed the global minimum. As the dimensions of the parameter space increase when the number of mode pairs increases, optimization using this method can require substantial computational time. As reported in Ref. 1, this method appears to give adequate results for this type of parameter fitting. Thus we continue to use it in this investigation. It has the further benefit of being very simple to implement, thus making this methodology available to any engineer with basic programming skills.

The constraints on the parameters have already been discussed [4.1]. For the parameters common to all models, that is, the relaxation times, $\lambda_i(s)$, and the concentrations, n_i (mol/m^3), of each mode, the constraints are that each quantity is a

positive entity. Constraints on parameters that are peculiar to the various models investigated herein are discussed later.

We used the following expression for the objective function, F_{obj}, which was the function minimized by the NMDSM:

$$F_{obj} = \sqrt{\frac{\sum_{j=1}^{n_{type}} \sum_{i=1}^{n_j} w_{i,j} \left(\frac{R_{i,j,\exp} - R_{i,j,\text{model}}}{R_{i,j,\exp}} \right)^2}{\sum_{j=1}^{n_{type}} \sum_{i=1}^{n_j} w_{i,j}}} \tag{4.1}$$

In this expression, n_{type} is the number of data types (types of data for the present article are the dynamic moduli, as well as the steady-state shear viscosity and first normal stress coefficient), n_j is the number of data points of a specific type of data, $w_{i,j}$ is the weight factor of the corresponding data, and $\mathbf{R}$ is the value of either the experiment or model.

Since the dimension of solution space can be quite large, the method used to obtain a reasonable initial guess is vital to the optimization code. Generally, we fit the dynamic moduli data from the SAOSF experiment by varying λ_i and n_i for $i = 1,...,6$. We used initial guesses for the relaxation times with incremental orders of magnitude. Furthermore, for initial guesses of the modal concentrations, we chose values that were very close to zero. Once the dynamic moduli data were fit well, we then used the converged values of the parameters as an initial guess to fit simultaneously both steady-state shear viscosity and dynamic moduli data. Finally, we also used the optimized parameter set from the previous step as the initial guess to fit simultaneously three sets of experimental data, including: dynamic moduli, steady-state shear viscosity, and steady-state first normal stress coefficient. We did not include the experimental data for the

transient shear stress or first normal stress difference among the data that we fit, nor the transient uniaxial elongational viscosity data.

Over the past few decades, several different methods have been put forth for fitting rheological models (typically composed of uncoupled Maxwell modes) to linear viscoelastic data [4.18,4.20-4.24]. Over time, these methods have generally become more sophisticated as computational capabilities have increased, and have done a better job of fitting parameters with smaller RMS error. These methods are, however, not easily generalized to cases involving non-linear viscoelastic data and more complicated rheological models. Such methods that do exist for fitting non-linear viscoelastic data suffer from a lack of sophistication. We are not addressing the issue of sophistication in this article; we want to employ a crude optimization methodology in order to examine what is possible for the average industrial polymer engineer to achieve with a given rheological model.

In order to examine whether or not our optimization technique is sufficient for this application, we must compare it with one of the sophisticated methods mentioned above. Those methods, as discussed above, are only for linear viscoelastic data. Although there is no basis of comparison for non-linear viscoelastic data, we can compare our methodology to prior optimization methods for the linear data. In Figure 4.1, we present the dynamic moduli data of the LDPE sample described above in the SAOSF experiment, along with a fit of six uncoupled Maxwell modes using the Padé-Laplace methodology of Simhambhatla and Leonov [4-18], according to the authors' *PADLAP* program. The RMS error of this sophisticated fit is less than 5%, which is quite good. We believe that six modes is the minimum number needed by this method to get a very

good fit of the experimental data. The parameter values obtained from the optimization routine are presented in Table 4.2. Suffice it to say that the exact same fit can be obtained using the optimization routine developed in this work. Furthermore, for the six-mode version of the Upper-Convected Maxwell Model used herein, not only is the fit the same as in the more sophisticated code, but the parameter values obtained are essentially the same as well (within 1% RMS error). Thus we conclude that, at least as far as the linear viscoelasticity data is concerned, our optimization methodology is sufficient to the task under consideration.

4.5 Uncoupled linear relaxation models with constant relaxation times

The example tested under this class of viscoelastic fluid models is the Uncoupled Maxwell Modes (UMM) Model, which is composed of six Upper-Convected Maxwell Modes. Beforehand, we are aware of the well-known deficiencies of this model for fitting non-linear viscoelasticity data, but we examine its behavior here as a base case, since all other models tested herein reduce to it in the linear, uncoupled modes limit.

The UMM Model equations are expressed in terms of six uncoupled evolution equations for the six mode stress tensors, σ^i, $i = 1,\ldots,6$:

$$\sigma^i_{\alpha\beta} + \lambda_i \hat{\sigma}^i_{\alpha\beta} = 2 n_i N_A k_B T \lambda_i A_{\alpha\beta} \tag{4.2}$$

where the upper-convected derivative is defined as

$$\hat{\sigma}^i_{\alpha\beta} \equiv \frac{\partial \sigma^i_{\alpha\beta}}{\partial t} + v_\gamma \nabla_\gamma \sigma^i_{\alpha\beta} - \sigma^i_{\alpha\gamma} \nabla_\gamma v_\beta - \sigma^i_{\beta\gamma} \nabla_\gamma v_\alpha \tag{4.3}$$

In the above expressions, k_B is Boltzmann's constant, T is the absolute temperature, N_A is Avogadro's number, and $A_{\alpha\beta} = \left(\nabla_\alpha v_\beta + \nabla_\beta v_\alpha\right)/2$ is the symmetric part of the velocity gradient tensor field. The total extra stress in the fluid is then expressed as the sum over all of the mode stress tensors:

$$\sigma_{\alpha\beta} = \sum_{i=1}^{6} \sigma_{\alpha\beta}^{i} \tag{4.4}$$

This equation set can be used to calculate the rheological properties of the polymer following standard definitions. The storage and loss moduli in SAOSF can be expressed as

$$G'(\omega) = \sum_{i=1}^{6} \frac{\eta_i \lambda_i \omega^2}{1 + \left(\lambda_i \omega\right)^2} \tag{4.5}$$

$$G''(\omega) = \sum_{i=1}^{6} \frac{\eta_i \omega}{1 + \left(\lambda_i \omega\right)^2} \tag{4.6}$$

respectively, where ω is the angular frequency of the SAOSF and $\eta_i = n_i N_A k_B T \lambda_i$.

In steady shear flow, the shear viscosity (η) of the UMM Model is independent of shear rate, as is the first normal stress coefficient (Ψ_1). Consequently, we have no hope of fitting the shear-thinning behavior exhibited by this LDPE, and therefore we perform the optimization by fitting the model parameters to the SAOSF data and the Newtonian plateau for η at low shear rates. The parameter values thus obtained are reported in Table 4.3. They are significantly different than those found using the *PADLAP* program, which is due to the fact that we have used the steady-shear data in the optimization as well as the SAOSF data. This is also an indication that the *PADLAP* parameters cannot be used to model accurately steady shear flow. It raises the question

as to whether or not the relaxation times determined using only SAOSF have any meaning outside of SAOSF: it is well-known that the parameterization of linear viscoelastic flow data is an ill-posed mathematical problem [4.20].

The fit of the UMM Model to the experimental data for the dynamic moduli (G' and G'') versus frequency in the SAOSF experiment is virtually indistinguishable from that displayed in Fig. 1. The fit is very good, and the RMS error is less than 5%.

In Figure 4.2, we plot the experimental data and the fit with UMM Model for the steady-state shear viscosity versus shear rate. With this model, we can only fit the Newtonian plateau at low shear rates; however, the figure indicates that it is possible to do this simultaneously with fitting the SAOSF data. Also in Figure 4.2, the model prediction is given for the first normal stress coefficient as a function of shear rate. As well known, the UMM Model predicts a constant value of Ψ_1. Therefore, we have no hope of predicting anything other than the Newtonian plateau value of this quantity at low shear rates; perhaps surprisingly, the value predicted is not too far off from the experimental value. Of course, the value of Ψ_2 predicted by this model is zero for all shear rates.

Since the UMM Model cannot fit the shear-thinning behavior of either η or Ψ_1, there is no point in trying to predict the transient steady-shear data in this regime. Our conclusion is thus that the UMM Model cannot be used to predict non-linear rheological behavior in shear flow, although it is possible to get good results within the linear regime.

In Figure 4.3, we plot UMM Model predictions for the uniaxial elongational viscosity versus time for different elongational strain rates. For comparison purposes, the experimental Trouton curve (3η at $\dot{\gamma} = 0.01 s^{-1}$) and its UMM Model prediction in

steady shear flow are plotted as well. This figure demonstrates that the UMM Model generally reflects the trend of change of elongational viscosity versus time and strain rate in the region studied, although the errors between theoretical results and experimental data are huge. Furthermore, the steady-state values of the viscosity predicted by the UMM Model are obviously going to be way too high.

4.6 Uncoupled linear relaxation models with variable relaxation times

The Uncoupled Extended White/Metzner (UEWM) Model is a variation of the UMM Model wherein the mode relaxation times are no longer treated as constants. In this model, each mode relaxation time is taken as a function of the corresponding mode stress tensor. Here we choose the following relationship to express this functional dependency:

$$\lambda_i = \lambda_{0,i}\left(\mathrm{tr}(\frac{\sigma^i}{n_i K_B T}) + 1 \right)^{k_i} \tag{4.7}$$

where, $k_i \le 0$, which is similar in spirit and practice to the relationship of Souvaliotis and Beris [4.4]. We chose this slightly different functional form of Eq. (4.7) because it seems to give a somewhat smoother description of steady shear flow properties than the one originally proposed by the former authors. Note that other than this small change, all other equations from the preceding section carry over to this case. Consequently, the UEWM Model will reduce to the UMM Model when all of the k_i are equal to zero.

As described in the section on optimization, we fit the parameters of the UEWM Model to experimental data of SAOSF, steady-shear viscosity, and first normal stress coefficient. Then we predict the rheological properties of polymer melts in transient

shear and uniaxial elongational flows using the corresponding parameters acquired through the data fitting. The parameter values obtained through the fitting are reported in Table 4.4.

As for the SAOSF experimental data, the fit achieved here is not quite as good as in the previous two cases, but is still less than 10% RMS error. (See Table 4.5 for a compilation of RMS errors for this study.) Figure 4.4 displays the fits to the steady shear viscosity and first normal stress coefficient. The fits are quite decent, with associated RMS errors of roughly 8 and 6 percent, respectively. Note that the steady shear viscosity is fitted over seven decades of shear rate. Obviously, this model does a much better job of fitting steady shear data than the UMM Model, which is strictly linear. The prediction for the second normal stress coefficient is again zero, since the UEWM Model does nothing to correct this inadequacy of the UMM Model. (See Table 4.6 for zero shear-rate values of Ψ_2 / Ψ_1.)

We plot the shear stress (SS) and first normal stress difference (N_1) versus time for transient shear flow at $0.5s^{-1}$ and $1.0s^{-1}$, respectively, in Figures 4.5 and 4.6. These plots are presented logarithmically, which accentuates the differences between the theoretical predictions and the experimental data at very short and very long times. Data was taken at shear rates ranging from 0.01 to $5s^{-1}$, with similar results obtained as those reported herein. In both cases, the shear stress transients at flow start-up and cessation are predicted fairly well, with only a slight underprediction of the overshoot upon start-up. The prediction of the first normal stress difference fairs well over most of the time range examined, but fails quantitatively at both short and long times. The model overpredicts N_1 at low times, and underpredicts it at long times. This seems to indicate that the

relaxation times fitted to the SAOSF data and steady shear data only do not capture the full range of characteristic time scales for the transient shear behavior. This is probably due to the limited range of the SAOSF experiment (0.01 to $100s^{-1}$), or else due to the fact that the SAOSF experiment does not probe N_1.

In Figure 4.7, we plot the elongational viscosity versus time for different elongation rates. The plot shows that the elongational viscosity increases with increasing time and then reaches a steady-state value. Unfortunately, the theoretical predictions underestimate the experimental results, and actually fall below the Trouton curve (at a shear rate $0.01s^{-1}$); this is possible because the UEWM Model exhibits both thickening and thinning behavior of the elongational viscosity, depending on the choice of parameters [4.4]. The prediction obtained is actually better than the UMM Model prediction from an RMS perspective (see Table 4.5), but still cannot be considered as a success.

4.7 Uncoupled non-linear relaxation models

The next class of rheological models examined is that of uncoupled, non-linear relaxation models. The example of this class studied here is the Uncoupled Giesekus Modes (UGM) Model. The constitutive equation for each mode stress tensor is taken as[4.5]

$$\sigma^i_{\alpha\beta} + \lambda_i \hat{\sigma}^i_{\alpha\beta} + \frac{\alpha_i}{G^i_0}\sigma^i_{\alpha\gamma}\sigma^i_{\gamma\beta} = 2\eta_i A_{\alpha\beta} \tag{4.8}$$

where $G^i_0 = n_i N_A k_B T$ and $\eta_i = n_i N_A k_B T \lambda_i$. The additional parameter, α_i, is the mobility factor, lying within the range $0 \le \alpha_i \le 1$. The total extra stress tensor is again given by

the sum of the mode stress tensors, Eq. (4.4). The dynamic moduli in SAOSF are still given by Eq. (4.5) and (4.6), since the non-linear terms in the UGM Model do not contribute to the linear viscoelastic behavior.

Consistent fits for the data of dynamic moduli, shear viscosity, and first normal stress coefficient were obtained with this model; the parameter values thus obtained are reported in Table 4.7. Plots of these fits are quite similar to those of Figures 4.1 and 4.4. The RMS errors associated with these fits are reported in Table 4.5.

The zero shear rate value of $\Psi_2 / \Psi_1 \approx -0.1$ predicted by the model is quite reasonable. (See Table 4.6 for the exact value.) The transient shear stress under start-up and cessation of shear flow is also described well, as seen in Figures 4.8 and 4.9. The overshoot upon start-up of shear is quantitatively predicted in magnitude and duration. The relaxation behavior is quantitatively predicted at all but the longest times and highest shear rates for which data was obtained. At low values of shear rate (not presented in this paper), the first normal stress difference predictions are also quite good. At higher values of the shear rate, as shown in Figures 4.8 and 4.9, the problems of the UEWM Model remain with regard to the very short and very long time behavior. Furthermore, the overshoot in N_1, barely apparent in the experimental data, is quite prominent in the model predictions. The magnitude of the predicted overshoot is roughly three times the magnitude of the experimental overshoot. As the shear rate is increased beyond $1s^{-1}$, this discrepancy tends to disappear as the experimental overshoot gains magnitude quickly. Unfortunately, measurements could not be obtained beyond $5s^{-1}$. One interesting point is that both the predictions and data attain a steady-state value at approximately the same point in time.

In Figure 4.10, we plot the elongational viscosity versus time for the different elongational rates. The predictions for this quantity are much better than those for the UEWM Model, but the steady-state values are still too low. This result is congruent with the generally accepted viewpoint that the Giesekus Model does a relatively good job describing extensional flow characteristics.

4.8 Pair-wise coupled relaxation models

In this section, we begin to examine whether or not coupling between the various relaxation modes can contribute to the rheological response of a polymer melt. Intuitively, it seems evident that such would be the case; however, such a coupling is not going to be apparent in every rheological characterization experiment. For the present section, we limit our examination to models with pair-wise coupling between the various modes; i.e., each mode can couple with one, and only one, additional mode. Our reasons for examining this case are discussed in the introduction. However, we will look at two versions of pair-wise coupled relaxation models, the simplest possible version, the Pair-wise Coupled Maxwell Modes (PCMM) Model, and the Pair-wise Coupled Maxwell Modes Model with the White/Metzner-like extension described above (PCMM-EWM).

4.8.1 The PCMM Model

The constitutive equations for the mode stress tensors in the PCMM Model are given by [4.11, 4.25]

$$\lambda_i \hat{\sigma}^i_{\alpha\beta} + \sigma^i_{\alpha\beta} + \theta_{ij} \frac{n_i}{n_j} \sqrt{\frac{n_i \lambda_i}{n_j \lambda_j}} \sigma^j_{\alpha\beta} + \frac{\theta_{ij}}{2 n_j k_B T} \sqrt{\frac{n_i \lambda_i}{n_j \lambda_j}} (\sigma^i_{\alpha\gamma} \sigma^j_{\gamma\beta} + \sigma^j_{\alpha\gamma} \sigma^i_{\gamma\beta}) = 2 \eta_i A_{\alpha\beta} \tag{4.9}$$

where θ_{ij} is a coupling parameter that quantifies the degree of interaction between modes *i* and *j*. From experience[4.1,4.26], the coupling parameters are required to lie within the interval [0,1], but are typically small positive fractions. The evolution equation for mode *j* is the same as Eq. (4.9) with the indices permuted. For a fluid modeled with six modes, there are three independent pairs of coupled evolution equations of this type. The total extra stress tensor is once again obtained through Eq. (4.4).

The coupling in the PCMM Model affects the linear viscoelastic behavior [4.25]; hence, the complex modulus in SAOSF is no longer that of the UMM Model, but is given by

$$\frac{G_{ij}}{i\omega} = \frac{\eta_i(De_j i + 1) + \eta_j(De_i i + 1) - \sqrt{\eta_i \eta_j}\theta_{ij}\chi_{ij}}{(1 - De_i De_j) + i(De_i + De_j) - \theta_{ij}^2} \tag{4.10}$$

where

$$De_i \equiv \omega \lambda_i \text{ and } \chi_{ij} = \frac{\eta_i De_j}{\eta_j De_i} + \frac{\eta_j De_i}{\eta_i De_j} \tag{4.11}$$

Note that Eq. (4.10) applies to each pair of modes, so that the total complex modulus is given by the sum of three quantities. In the limit of $\theta_{ij} \to 0$, it can be shown that Eq. (4.10) reduces to the complex modulus of the UMM Model, Eq. (4.5) and (4.6).

The PCMM Model was studied extensively by Jiang et al. [4.1], and was found to be a very peculiar model. It was used as the test case for our preliminary study, and so it will only be discussed very briefly here. The fits to the dynamics moduli, steady shear viscosity, and first normal stress coefficient display a characteristic waviness [4.1]. The cause of this is the inherently linear nature of the Maxwell relaxation modes; i.e., without the coupling parameter, the model reduces to the UMM Model, with all of its associated

problems arising from its linear responses. In order for the PCMM Model to fit the shear-thinning behavior of η or N_1, it is necessary for this model to have non-zero values of the coupling parameters, θ_{ij}. Consequently, the model must set the concentration of one mode of each pair (the one with the shorter relaxation time) to zero in order to produce artificially the shear-thinning behavior. Thus one really obtains only a three-mode fit (since only three modes influence the stress tensor) of the complex modulus, thus producing the inherent waviness. For more details as to this phenomenon, please refer to Part 3.

Because of the waviness of the steady shear data, the RMS error of these curves is much greater than the previous cases. Consequently, predictions of the transient shear and elongational behavior are also subject to errors, and nothing is to be gained by presenting them. It is interesting, however, that the prediction for the ratio of normal stress coefficients is approximately –0.09.

4.8.2 The PCMM-EWM Model

One might expect that replacing the constant relaxation times in the PCMM Model with the White/Metzner extension of Eq. (4.7) could alleviate the problems reported in the preceding subsection. This would relieve the smaller relaxation time modes of each pair of the necessity of having a null value for their concentration parameters, since the EWM non-linearity would produce the requisite shear-thinning behavior. This expectation was tested, with the following results.

The constitutive equations for the mode stress tensors in this case are the same as Eq. (4.9) above, with Eq. (4.7) inserted for the mode relaxation times. The equation for the complex modulus, Eq. (4.10), is not affected by this insertion, since it is a linearized expression. Using these equations, the model was fitted to the same data as prior cases, and the parameters reported in Table 4.8 were obtained. Note that the modal concentrations of the shorter relaxation times are not necessarily null-valued now. The fits obtained with these parameter values for the dynamic moduli, shear viscosity, and first normal stress coefficient are very similar to those of Figures 4.1 and 4.4, and are not presented. The RMS errors of the fits are reported in Table 4.5.

Predictions for the transient shear and elongational behavior are presented in Figures 4.11-13. The shear behavior is similar to that of the UGM Model, whereas the elongational prediction has improved over that of the UGM Model. Interestingly, the value of the normal stress ratio has dropped to zero (see Table 4.6). Note that the coupling parameter values in Table 4.8 are all very small, indicating that this model performs similarly to the UEWM Model. The only effect of the coupling thus appears to be on the elongational viscosity. These trends will be considered in greater detail in the discussion below.

4.9 Fully-coupled relaxation models

The obvious generalization of the PCMM Models is to allow full coupling between all of the mode stress tensors. Thus we examine a Fully-Coupled Maxwell Modes (FCMM) Model, as well as a FCMM Model with the White/Metzner-like

extension (FCMM-EWM Model). It is highly likely that such generality will not be necessary, and that only some modes will interact with each other. Here, we allow the optimization methodology to choose the degree of coupling necessary to fit the requisite experimental data. As seen below, many of the coupling parameters turn out to be negligibly small, indicating effectively no interactions between the corresponding relaxation modes.

4.9.1 The FCMM Model

In this model, the constitutive equations for the mode stress tensors are given by [4.11]

$$\lambda_i \hat{\sigma}^j_{\alpha\beta} + \sigma^j_{\alpha\beta} + \sum_{j=1, j\neq i}^{6} \theta_{ij} \frac{n_i}{n_j} \sqrt{\frac{n_i \lambda_i}{n_j \lambda_j}} \sigma^j_{\alpha\beta} + \sum_{j=1, j\neq i}^{6} \frac{\theta_{ij}}{2 n_j k_B T} \sqrt{\frac{n_i \lambda_i}{n_j \lambda_j}} (\sigma^j_{\alpha\gamma} \sigma^j_{\gamma\beta} + \sigma^j_{\alpha\gamma} \sigma^j_{\gamma\beta}) = 2\eta_i A_{\alpha\beta} \qquad (4.12)$$

For a given number of modes, n, the dynamical moduli in SAOSF can be calculated according to the linear equation

$$\left[G'_1, ..., G'_n, G''_1, ..., G''_n\right]^T = \mathbf{M}^{-1} \cdot \left[0, ..., 0, \eta_1 \omega, ..., \eta_n \omega\right]^T \qquad (4.13)$$

where

$$\mathbf{M}=\begin{bmatrix} 1 & \theta_{12}\frac{n_1}{n_2}\sqrt{\frac{n_1\lambda_1}{n_2\lambda_2}} & \cdots & \theta_{1n}\frac{n_1}{n_n}\sqrt{\frac{n_1\lambda_1}{n_n\lambda_n}} & -\lambda_1\omega & 0 & \cdots & 0 \\ \theta_{21}\frac{n_2}{n_1}\sqrt{\frac{n_2\lambda_2}{n_1\lambda_1}} & 1 & \cdots & \theta_{2n}\frac{n_2}{n_n}\sqrt{\frac{n_2\lambda_2}{n_n\lambda_n}} & 0 & -\lambda_2\omega & \cdots & 0 \\ \vdots & \vdots & \vdots & \vdots & \vdots & \vdots & \vdots & \vdots \\ \theta_{n1}\frac{n_n}{n_1}\sqrt{\frac{n_n\lambda_n}{n_1\lambda_1}} & \theta_{n2}\frac{n_n}{n_2}\sqrt{\frac{n_n\lambda_n}{n_2\lambda_2}} & \cdots & 1 & 0 & 0 & \cdots & -\lambda_n\omega \\ -\lambda_1\omega & 0 & \cdots & 0 & 1 & \theta_{12}\frac{n_1}{n_2}\sqrt{\frac{n_1\lambda_1}{n_2\lambda_2}} & \cdots & \theta_{1n}\frac{n_1}{n_n}\sqrt{\frac{n_1\lambda_1}{n_n\lambda_n}} \\ 0 & -\lambda_2\omega & \cdots & 0 & \theta_{21}\frac{n_2}{n_1}\sqrt{\frac{n_2\lambda_2}{n_1\lambda_1}} & 1 & \cdots & \theta_{2n}\frac{n_2}{n_n}\sqrt{\frac{n_2\lambda_2}{n_n\lambda_n}} \\ \vdots & \vdots & \vdots & \vdots & \vdots & \vdots & \vdots & \vdots \\ 0 & 0 & \cdots & -\lambda_n\omega & \theta_{n1}\frac{n_n}{n_1}\sqrt{\frac{n_n\lambda_n}{n_1\lambda_1}} & \theta_{n2}\frac{n_n}{n_2}\sqrt{\frac{n_n\lambda_n}{n_2\lambda_2}} & \cdots & 1 \end{bmatrix} \tag{4.14}$$

The FCMM Model has the same problem as the PCMM Model, namely, the linear Maxwell-type relaxation is not adequate to capture the shear-thinning behavior of the steady shear flow properties. Consequently, a fit of the moduli, shear viscosity, and first normal stress coefficient again reveals that all but one (at most) of the coupling parameters are negligibly small. This is required to reproduce artificially the necessary shear-thinning characteristics. As a consequence, the fits again display the wavy nature of the PCMM Model fits [1]. All other characteristics are similar to the PCMM Model, described above.

4.9.2 The FCMM-EWM Model

The last model examined here is the FCMM-EWM Model, wherein the relaxation times in Eq. (4.12)-(4.14) are replaced with the EWM relaxation time of Eq. (4.7). Parameter fits to the moduli, viscosity, and first normal stress coefficient again are very similar to those presented in Figs. 4.1 and 4.4, and RMS errors are reported in Table 4.5.

Table 4.9 contains the optimized parameter values. Note from Table 4.9b that many of the coupling parameters are still chosen to be zero, although there is a definite trend away from pair-wise coupling.

Predictions for the transient shear and elongational stresses are presented in Figures 4.14-16. RMS errors are collected in Table 4.5. The predictions are quite good for the shear properties, except again for N_1 at very short and very long times. The elongational viscosity predictions display the correct qualitative trends, but are not particularly good. The ratio of the normal stress coefficients is very small.

4.10 Comparison of model performances

RMS errors for the various models in the different experiments are summarized in Table 4.5. Overall, it is evident that the UGM and FCMM-EWM Models provide the best fitting and predictive capabilities of the models tested. Although the UGM Model has a lower RMS error for elongational viscosity than the FCMM-EWM Model, this is probably due simply to the fact that the former model underpredicts the viscosity, whereas the latter model overpredicts it. Qualitatively, the FCMM-EWM Model provides more aesthetically appealing fits of this quantity.

Thus, overall, the UGM and FCMM-EWM Models are the best models examined herein, although the FCMM-EWM Model contains the highest number of parameters (see Table 4.1): the UGM Model has 18 parameters, and the FCMM-EWM Model has 33 parameters. Note, however, that the optimized fit of the FCMM-EWM Model has only 21 non-negligible parameters, whereas the UGM Model has 17 non-negligible parameters.

Hence the FCMM-EWM Model is being fit with only about half of its inherent parameters. This model is also the most complex, and one must wonder at present whether or not this additional complexity is necessary. Unfortunately, the experiments performed herein are probably not the best ones to help answer this question. Double step-strain experiments (currently underway), wherein one might expect to see dramatic mode coupling effects, will provide a more complete picture of this aspect of the modeling.

Another interesting observation regarding the model behavior presented above is that the UGM Model gives a reasonable value of Ψ_2 / Ψ_1, as do the PCMM and FCMM Models. It is noteworthy that the FCMM-EWM Model does not. The source of this inadequacy is most likely due to the use of the White/Metzner (EWM) extension: remember that the UEWM Model still retained a null ratio. It thus seems plausible that having a reasonable value of this ratio is controlled by the non-linear (quadratic) relaxation terms in the UGM Model. In the coupled models without the EWM extension, a reasonable value is obtained because the non-linear relaxation effect is not washed out by the EWM modifications. This gives some minor indication that perhaps coupling effects (which are highly non-linear) can affect steady shear elastic properties such as Ψ_2, assuming that the uncoupled non-linear models are merely mimicking the effects of the coupled models. More investigation will hopefully yield a definitive answer to this puzzle.

4.11 Conclusion

The potential of rheological models to fit and predict experimental data was investigated in this article. For a series of models, parameter fits were generated by a numerical optimization procedure by fitting to experimental data from SAOSF and steady shear flow. Model predictions were then obtained for transient shear and elongational flows, and these were compared with available experimental data. Some models perform very well in one or two types of flows, although none of models can perform perfectly in all types of flows. All of the models examined herein were very simple, semi-phenomenological models, and were only used as representatives of the various classes of rheological models in use today. Nevertheless, the outlook seems bright for addressing the inadequacies of rheological constitutive equations, and potentially describing real materials with unprecedented accuracy. Such an event would be well worth pursuing.

Acknowledgements

We thank Drs. Simhambhatla and Leonov for allowing us to use their Padé-Laplace program, *PADLAP*, for determining the base-case linear viscoelastic parameters. Financial support was provided by the Chemical Engineering Department at the University of Tennessee.

References

4.1 B. Jiang, P.A. Kamerkar, D.J. Keffer, B.J Edwards, *J Non-Newtonian Fluid Mech* 2004, 120, 11.

4.2 N. Phan-Thien, R.I. Tanner, *J Non-Newtonian Fluid Mech* 1977, 2, 353.

4.3 M.R. Apelian, R.C. Armstrong, R.A. Brown, *J Non-Newtonian Fluid Mech* 1988, 27, 299.

4.4 A. Souvaliotis, A.N. Beris, *J Rheol* 1992, 36, 241.

4.5 H. Giesekus, *J Non-Newtonian Fluid Mech* 1982, 11, 69.

4.6.T.C.B. McLeish, R.G. Larson, *J Rheol* 1998, 42, 81.

4.7 N.J. Inkson, T.C.B McLeish, O.G. Harlen, D. J. Groves, *J Rheol* 1999, 43, 873.

4.8 K. Lee, M.R. Mackley, T.C.B McLeish, T.M Nicholson, O.G. Harlen, *J Rheol* 2001, 45, 1261.

4.9 C. D. Chodankar, J. D. Schieber, D.C. Venerus, *Rheol Acta* 2003, 42, 123.

4.10 C.D. Chodankar, J.D. Schieber, D.C Venerus, *J Rheol* 2003, 47, 413.

4.11 A.N. Beris, B.J. Edwards, *Thermodynamics of Flowing Systems*; Oxford University Press: New York, 1994.

4.12 L.M. Quinzani, G.H. McKinley, R.A. Brown, R.C. Armstrong, *J Rheol* 1990, 34, 705.

4.13 J.F. Agassant, F. Baaijens, H Bastian, A. Bernnat, A.C.B. Bogaerds, T. Coupez, B. Debbaut, A.L. Gavrus, A. Goublomme, M. van Gurp, R.J. Koopmans, H.M. Laun, K. Lee, O.H. Nouatin, M.R. Mackley, G.W.M Peters, G. Rekers, W.M.H. Verbeeten, B. Vergnes, M.H. Wagner, E. Wassner, W.F. Zoetelief, *Intern Polym Process* 2002, 17, 3.

4.14 L. Langouche, B. Debbaut, *Rheo Acta* 1999, 38, 48.

4.15 B. Debbaut, J. Dooley, *J Rheol* 1999, 43, 1525.

4.16 K. Feigl, F.X. Tanner, B.J. Edwards, J.R. Collier, *J Non-Newtonian Fluid Mech* 2003, 115, 191.

4.17 B.J. Edwards, S. Petrovan, J.R. Collier, K. Feigl, and F.X. Tanner, *7th World Congress of Chemical Engineering*, [CD-ROM], Glasgow, Scotland, July 10-14, 2005.

4.18 M. Simhambhatla, A.I. Leonov, *Rheol Acta* 1993, 32, 589.

4.19 W.H. Press, S.A. Tevkolsky, B.P. Flannery, *Numerical Recipes in Fortran 77*; Cambridge University Press: Cambridge, 1992.

4.20 J. Honerkamp, *J. Rheo Acta* 1989, 28, 363.

4.21 N. Orbey, J.M. Dealy, *J Rheol* 1991, 35, 1035.

4.22 R. Fulchiron, V. Verney, P. Cassagnau, A. Michel, P. Levoir, J. Aubard, *J Rheol* 1993, 37, 17.

4.23 W. Thimm, C. Friedrich, M. Marth, J. Honerkamp, *J Rheol* 1999, 43, 1663.

4.24 L. He, R. Ding, A.I. Leonov, H. Dixon, R.P. Quirk, *J Appl Polym Sci* 1999, 71, 1315.

4.25 B.J. Edwards, A.N. Beris, V.G. Mavrantzas, *J Rheol* 1996, 40, 917.

4.26 B.J. Edwards, D.J. Keffer, C.W. Reneau, *J Appl Polym* Sci 2002, 85, 1714.

Appendix

Tables

Table 4.1: Number of fitting parameters for each model investigated in this study. (See text for acronym definitions.)

Model	UMM	UEWM	UGM	PCMM	PCMM-EWM	FCMM	FCMM-EWM
Number of parameters	12	18	18	15	21	27	33

Table 4.2: Parameter values determined by the Padé-Laplace method using the *PADLAP* program.

Mode No.	1	2	3	4	5	6
λ_i (s)	1.000E-2	5.248E-2	2.754E-1	1.445	7.586	3.981E+1
n_i (mol/m^3)	1.441E+1	4.260	2.208	6.880E-1	1.781E-1	4.959E-3

Table 4.3: List of parameters for all modes of the UMM Model used to fit the data of SAOSF and shear viscosity at low shear rates.

Mode No.	1	2	3	4	5	6
λ_i (s)	1.108E-3	4.237E-3	4.082E-2	2.487E-1	1.435	9.583
n_i (mol/m^3)	7.456E-9	2.455E+1	5.995	2.337	7.862E-1	1.448E-1

Table 4.4: List of parameters for all modes of the UEWM Model used to fit the experimental data of dynamic moduli, shear viscosity, and first normal stress coefficient.

Mode No.	1	2	3	4	5	6
$\lambda_{0,i}$ (s)	1.000E-8	9.288E-3	1.854E-2	1.191E-1	1.054	8.978
n_i (mol/m^3)	6.925E-10	1.811E+1	8.782E-19	4.649	1.067	2.206E-1
k_i	-7.573E-7	-2.004	-6.184E-16	-1.994E+1	-1.492	-4.796E-1

Table 4.5: The relative root-mean-square (RMS) error (%) of different fits and predictions attained by different models. Note that the first three columns are fits, and the last three columns are predictions.

Model	Complex Modulus	Steady-state shear viscosity	Ψ_1	Elongational Viscosity	Transient shear stress ($\dot{\gamma}$ =0.5 & 1.0s^{-1})	Transient N_1 ($\dot{\gamma}$ =0.5 & 1.0s^{-1})
UMM	2.20	16,000	1,200	63,300	271	482
UEWM	9.38	8.04	6.25	94.8	18.5	51.2
UGM	4.78	8.59	7.68	49.3	7.60	130
PCMM	24.4	26.1	26.5	6,670	41.2	128
PCMM-EWM	11.5	6.28	7.11	51,400	24.1	54.1
FCMM	23.4	26.2	26.7	7,230	31.5	124
FCMM-EWM	2.71	5.47	12.7	841	11.8	126

Table 4.6: Ratio of the second normal stress coefficient to the first normal stress coefficient at low shear rates for the different models.

Model	UMM	UEWM	UGM	PCMM	PCMM-EWM	FCMM	FCMM-EWM
Ψ_2 / Ψ_1	0	0	-9.82E-2	-9.15E-2	-4.52E-17	-9.20E-2	-1.34E-9

Table 4.7: List of parameters for all modes of the UGM Model used to fit the data of dynamic moduli, shear viscosity, and first normal stress coefficient.

Mode No.	1	2	3	4	5	6
λ_i (s)	4.006E-4	9.481E-3	3.291E-2	8.672E-2	7.070E-1	7.795
n_i (mol/m^3)	7.714E+1	1.251E+1	1.354E-3	4.792	1.603	2.281E-1
α_i	1.862E-1	8.930E-1	3.375E-20	3.926E-1	9.193E-1	1.540E-1

Table 4.8: List of parameters for all modes of the PCMM-EWM Model used to fit the data of complex modulus, shear viscosity, and first normal stress coefficient.

Mode No.	1	2	3	4	5	6
$\lambda_{0,i}$ (s)	1.013E-5	4.313E-1	5.314E-4	3.284E-2	3.569E-3	6.933
n_i (mol/m^3)	1.313E-6	2.538	4.728E-11	8.428	2.180E+1	3.331E-1
k_i	-1.073E-14	-3.605	-1.797E+1	-4.690E-4	-1.866	-5.236E-1
θ_{ij}	3.909E-18		3.000E-18		4.196E-18	

Table 4.9: List of parameters for all modes of the FCMM-EWM Model used to fit the data of complex modulus, shear viscosity, and first normal stress coefficient.

a) Parameters for each mode.

Mode No.	1	2	3	4	5	6
$\lambda_{0,i}$ (s)	1.637E-4	2.391E-2	3.153E-2	1.015E+1	1.585	2.346E-1
n_i $(\mathrm{mol/m^3})$	7.076E-4	3.461E+1	7.329	1.347E-1	7.747E-1	2.693
k_i	-9.009E-2	-2.670	-1.320E2	-4.564E-1	-9.662E-1	-4.049

b) Coupling factors between the modes.

θ_{ij}	1	2	3	4	5	6
1	-	2.215E-12	1.284E-20	1.781E-20	1.122E-10	1.787E-10
2	2.215E-12	-	1.082E-19	1.212E-20	1.316E-20	2.408E-20
3	1.284E-20	1.082E-19	-	1.236E-20	1.185E-20	4.121E-12
4	1.781E-20	1.212E-20	1.236E-20	-	1.854E-20	8.720E-9
5	1.122E-10	1.316E-20	1.185E-20	1.854E-20	-	6.446E-20
6	1.787E-10	2.408E-20	4.121E-12	8.720E-9	6.446E-20	-

Figures

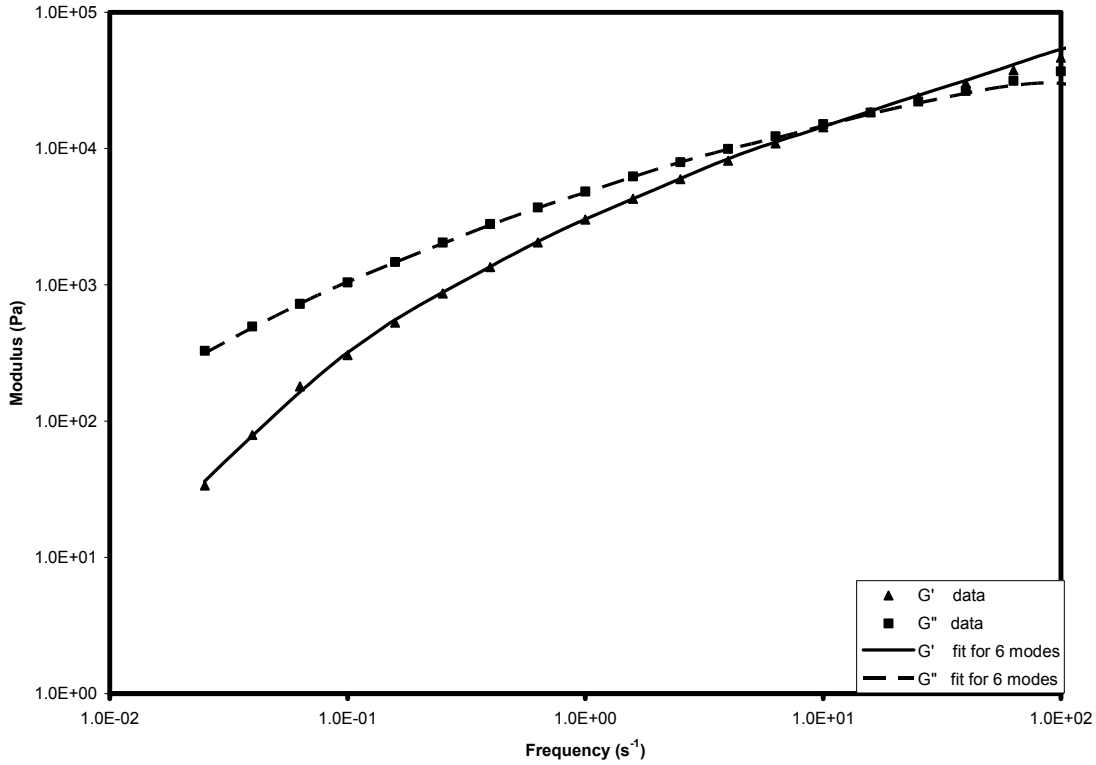

Figure 4.1: Fit of the Padé-Laplace program *PADLAP* to experimental data of the dynamic moduli in SAOSF. See Table 4.2 for parameter values.

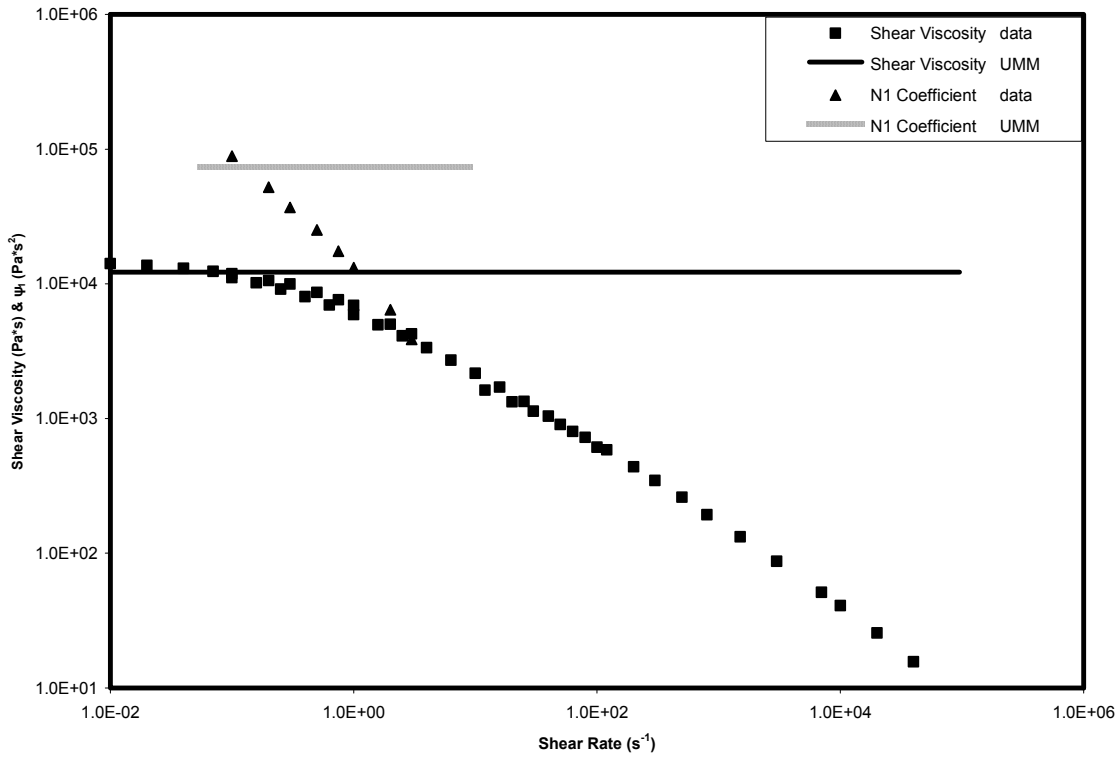

Figure 4.2: Steady-state shear viscosity and first normal stress coefficient versus shear rate, as fitted with the UMM Model.

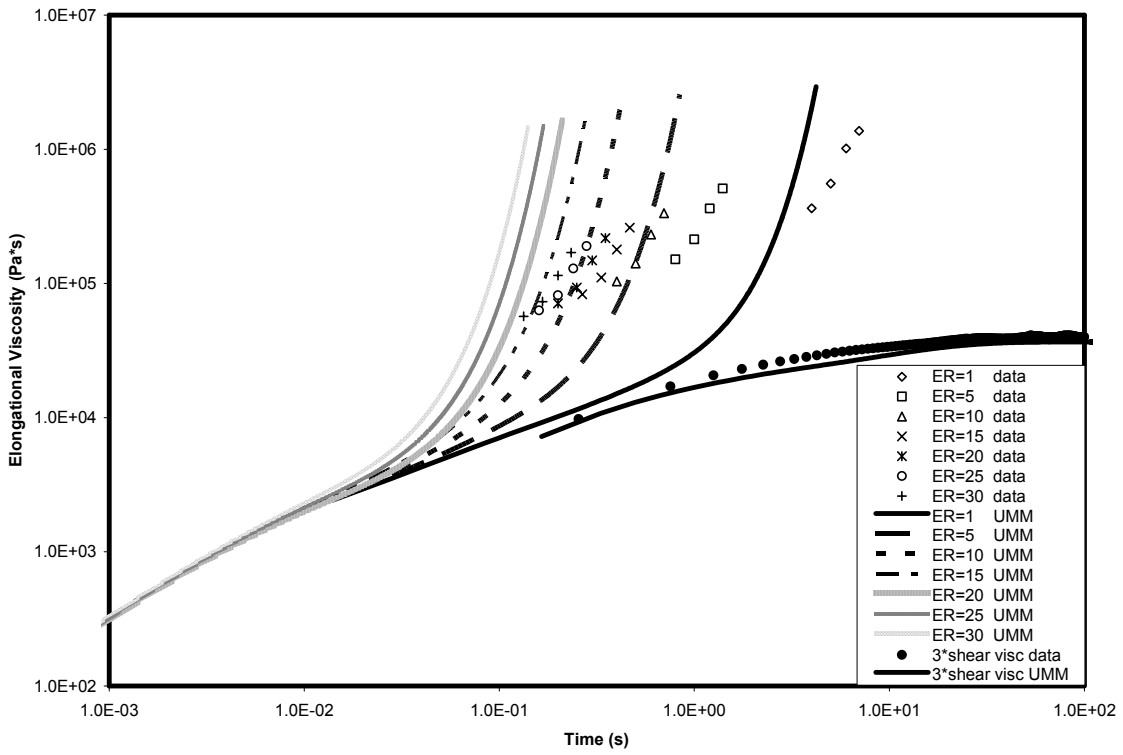

Figure 4.3: Elongational viscosity as a function of time, as predicted with the UMM Model. "ER" refers to the strain rate, in units of reciprocal seconds.

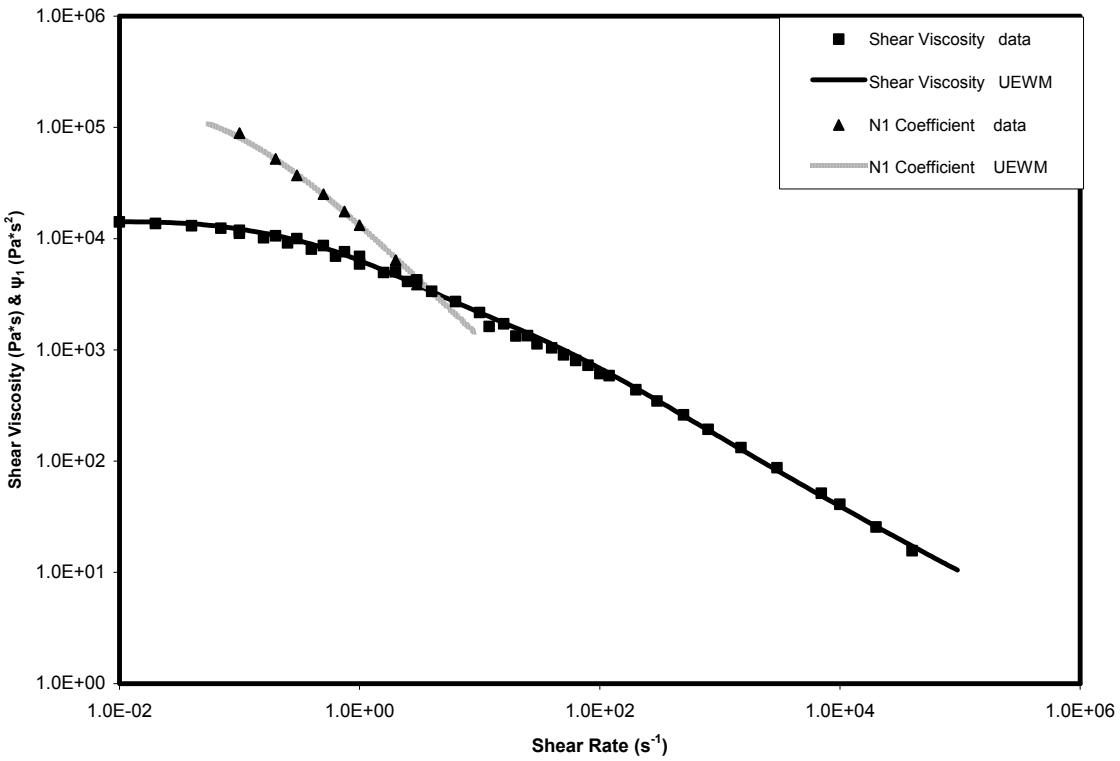

Figure 4.4: Steady-state shear viscosity and first normal stress coefficient versus shear rate, fitted with the UEWM Model.

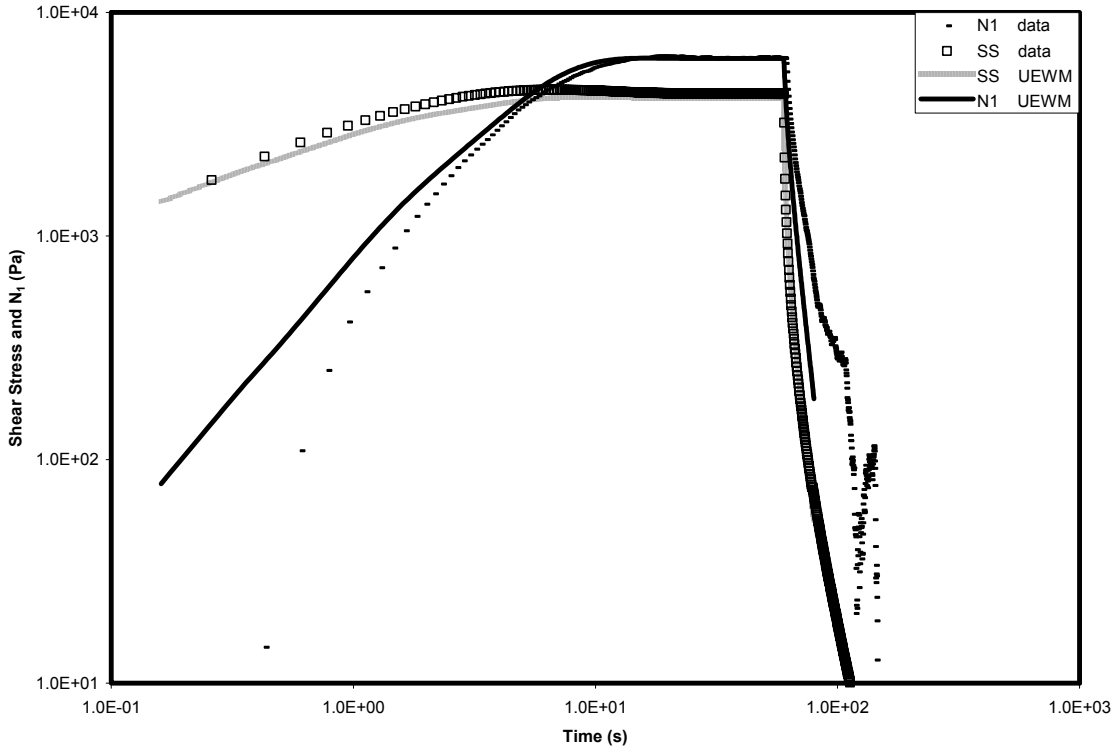

Figure 4.5: Transient stress as a function of time, predicted with the UEWM Model for the LDPE melt ($\dot{\gamma} = 0.5 s^{-1}$). "SS" refers to shear stress, and "N1" refers to the first normal stress difference.

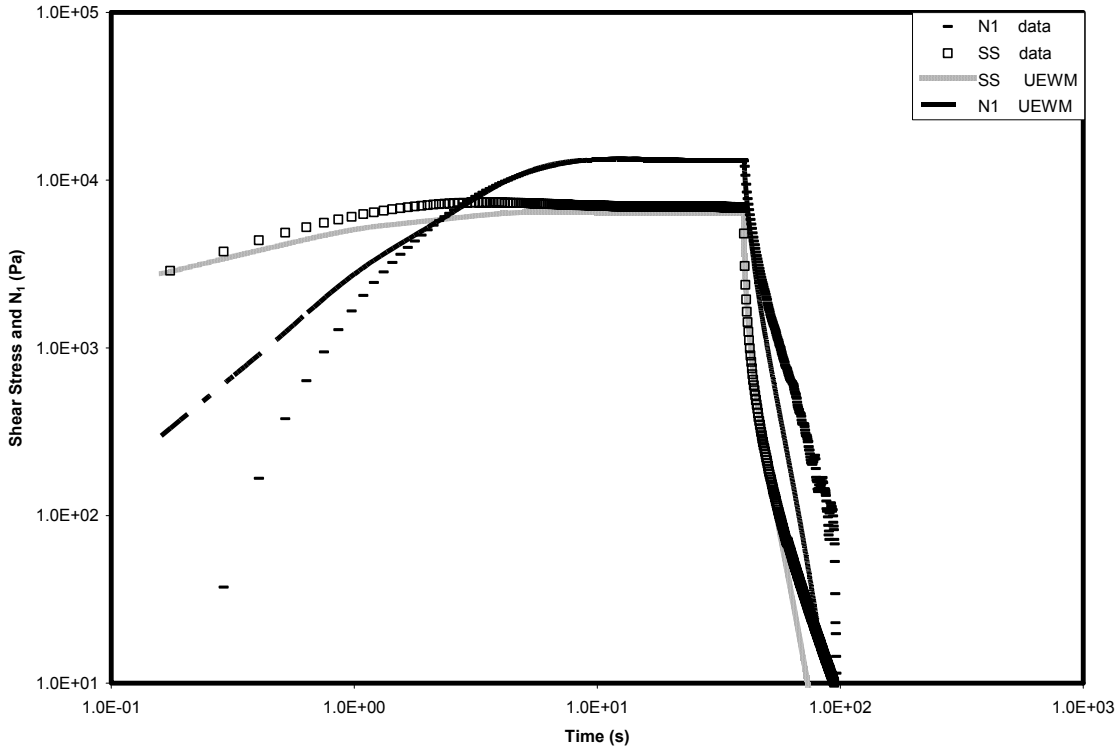

Figure 4.6: Transient stress as a function of time, predicted with the UEWM Model ($\dot{\gamma} = 1.0\,s^{-1}$). "SS" refers to shear stress, and "N1" refers to the first normal stress difference.

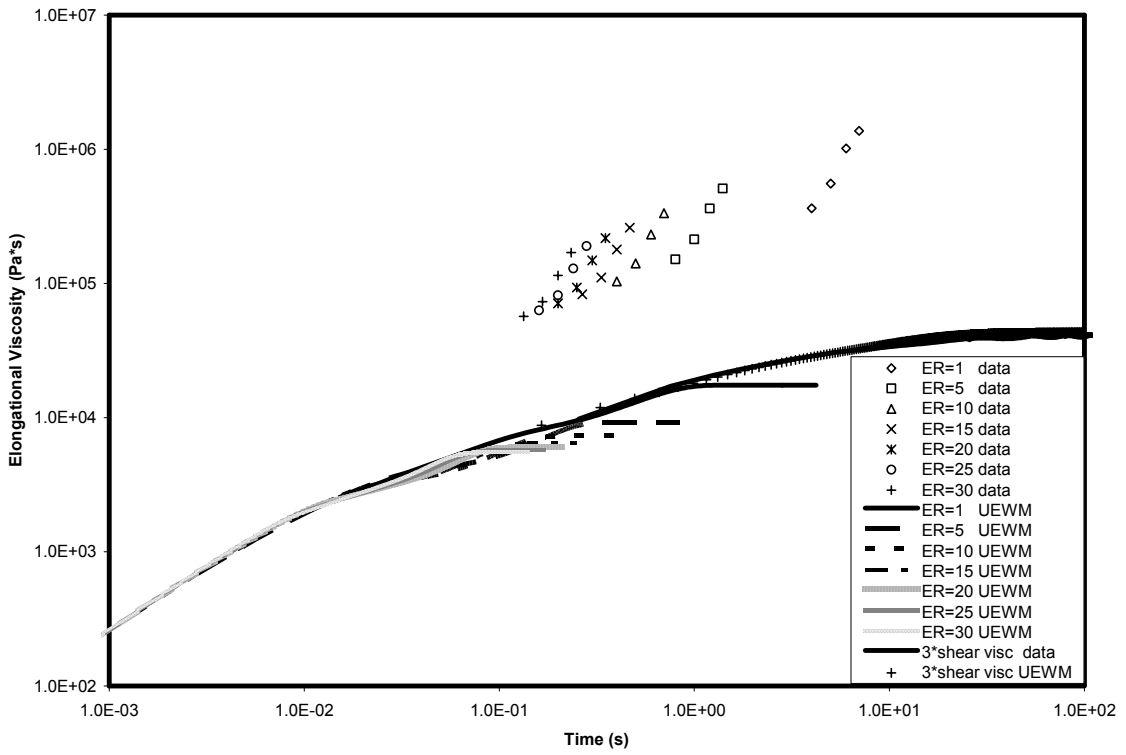

Figure 4.7: Elongational viscosity as a function of time, predicted with the UEWM Model. "ER" refers to the strain rate, in units of reciprocal seconds.

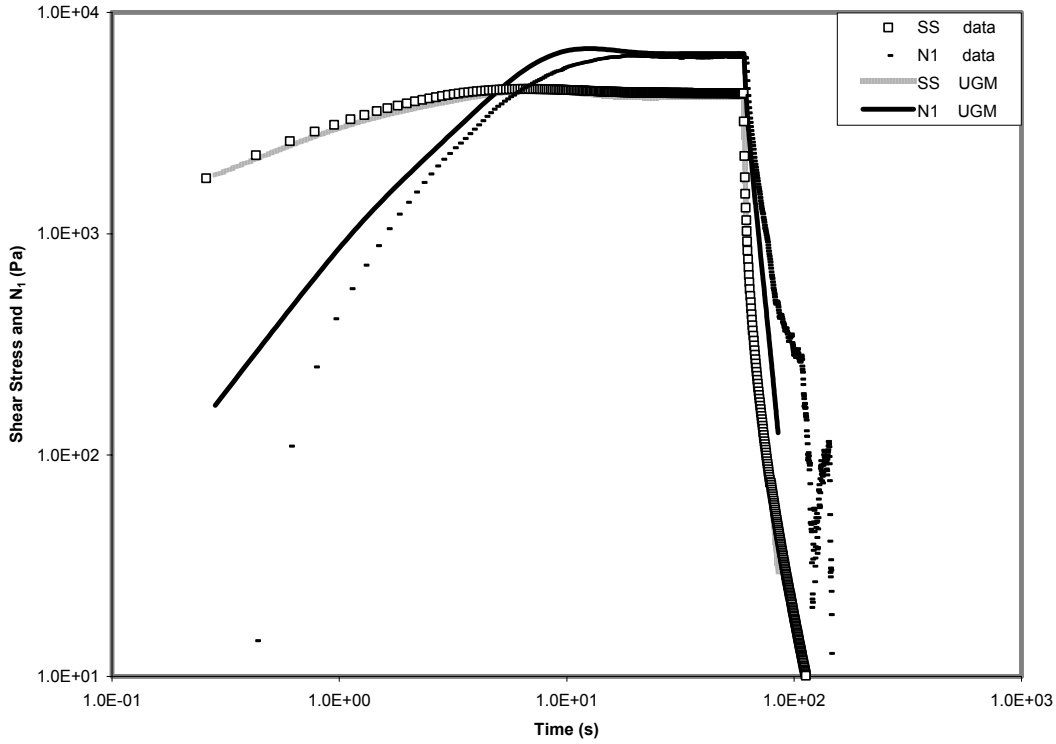

Figure 4.8: Transient stress as a function of time, as predicted with the UGM Model ($\dot{\gamma} = 0.5 s^{-1}$).

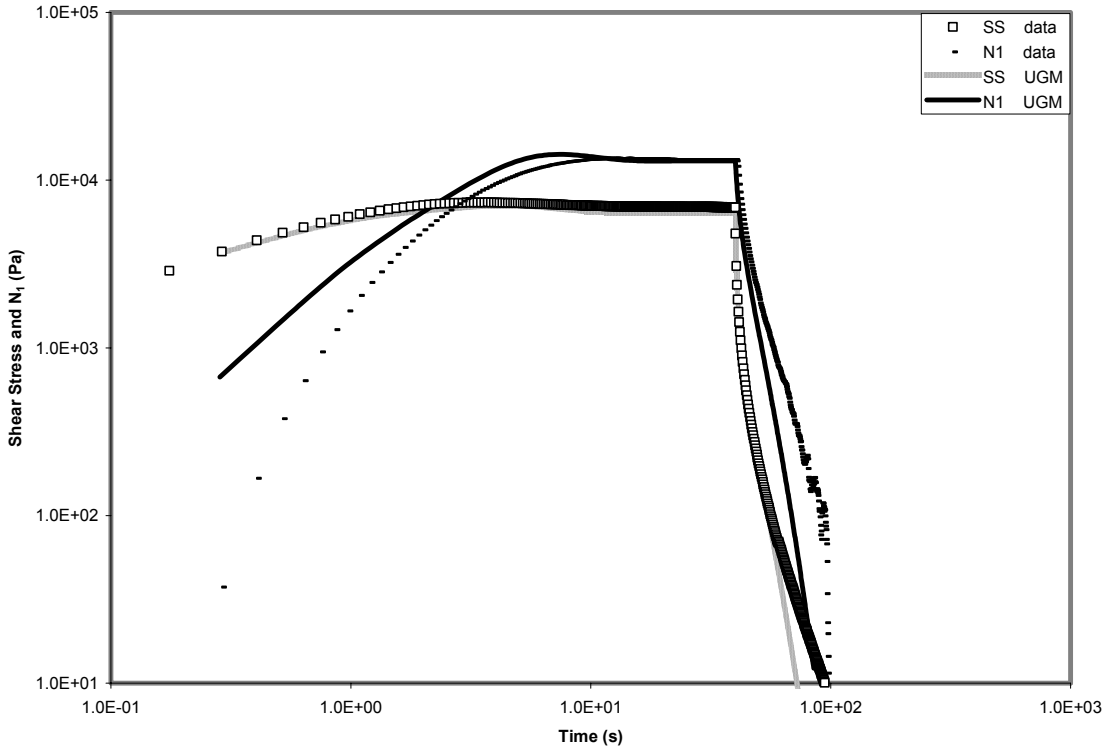

Figure 4.9: Transient stress as a function of time, as predicted with the UGM Model ($\dot{\gamma} = 1.0\, s^{-1}$).

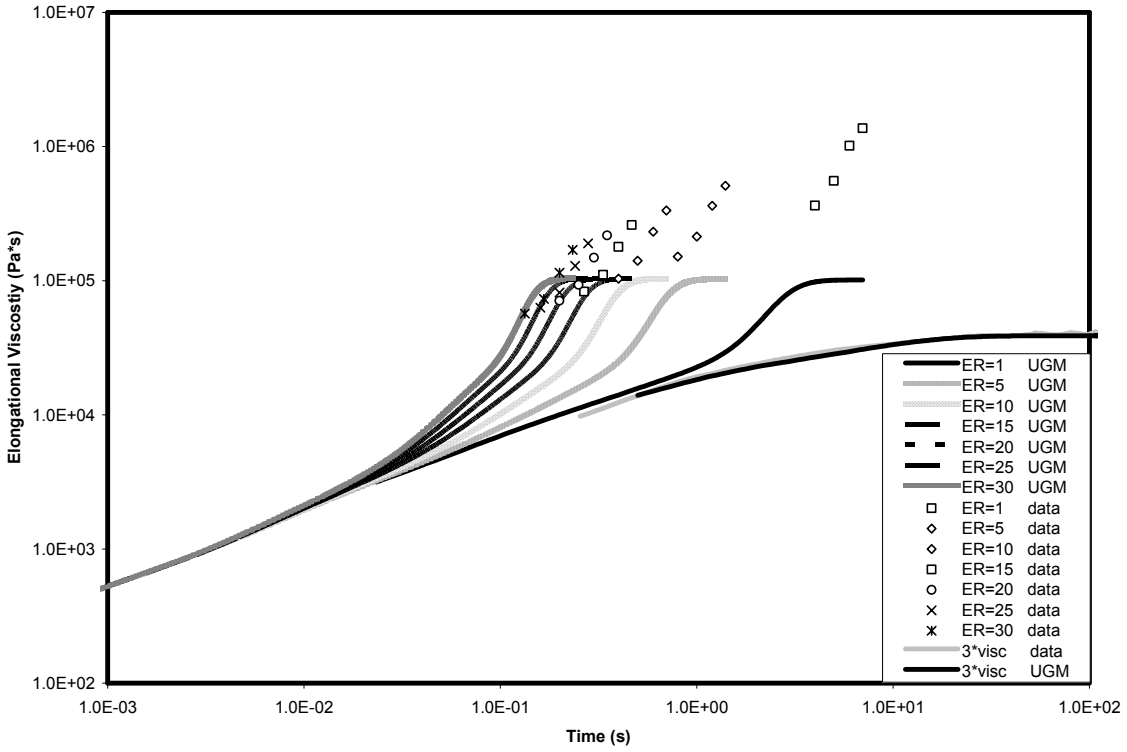

Figure 4.10: Elongational viscosity as a function of time, as predicted with the UGM Model.

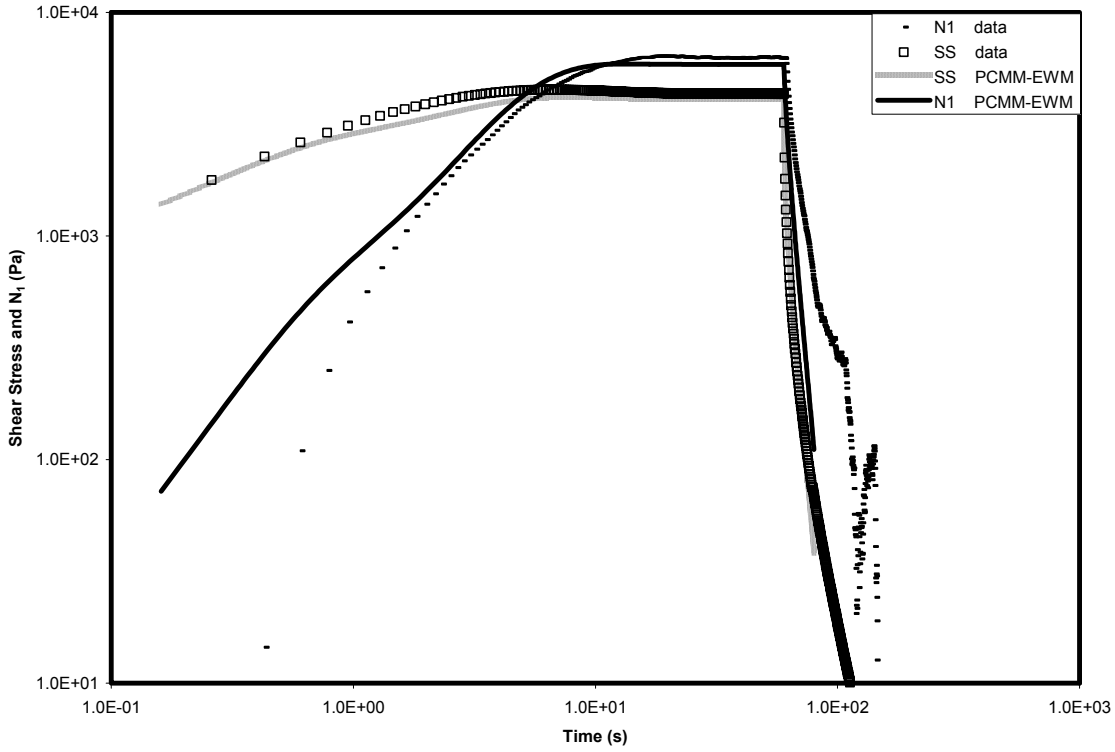

Figure 4.11: Transient shear stress as a function of time, as predicted with the PCMM-EWM Model ($\dot{\gamma} = 0.5 s^{-1}$).

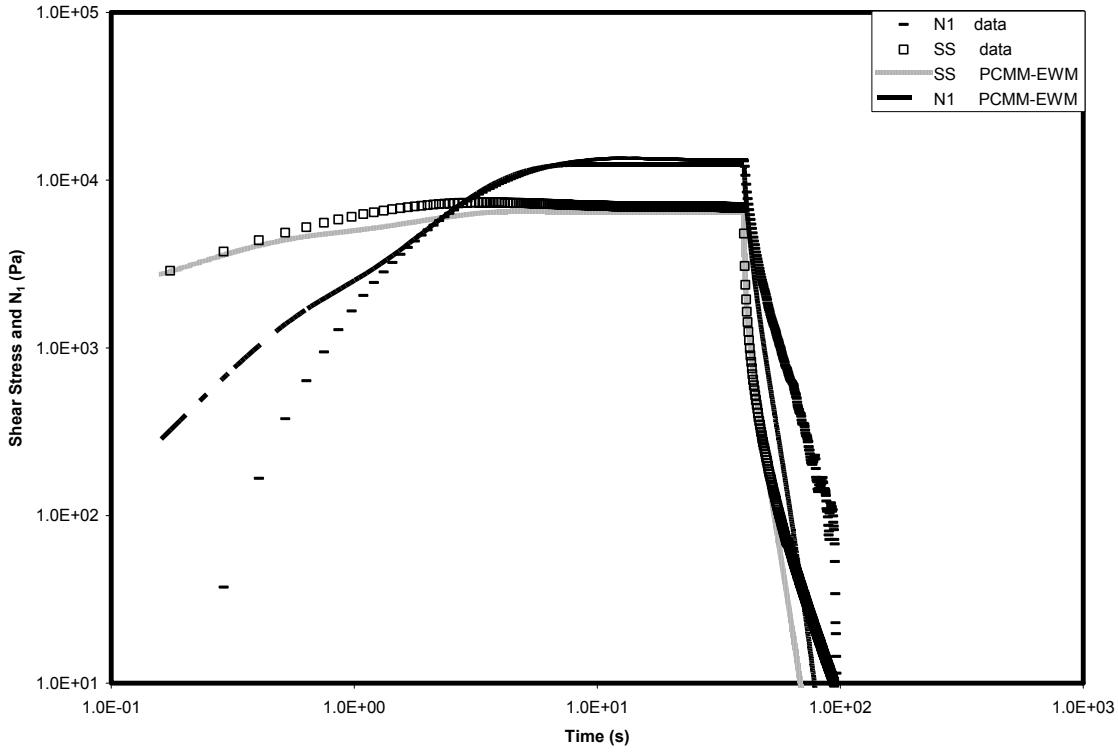

Figure 4.12: Transient shear stress as a function of time, as predicted with the PCMM-EWM Model ($\dot{\gamma} = 1.0\, s^{-1}$).

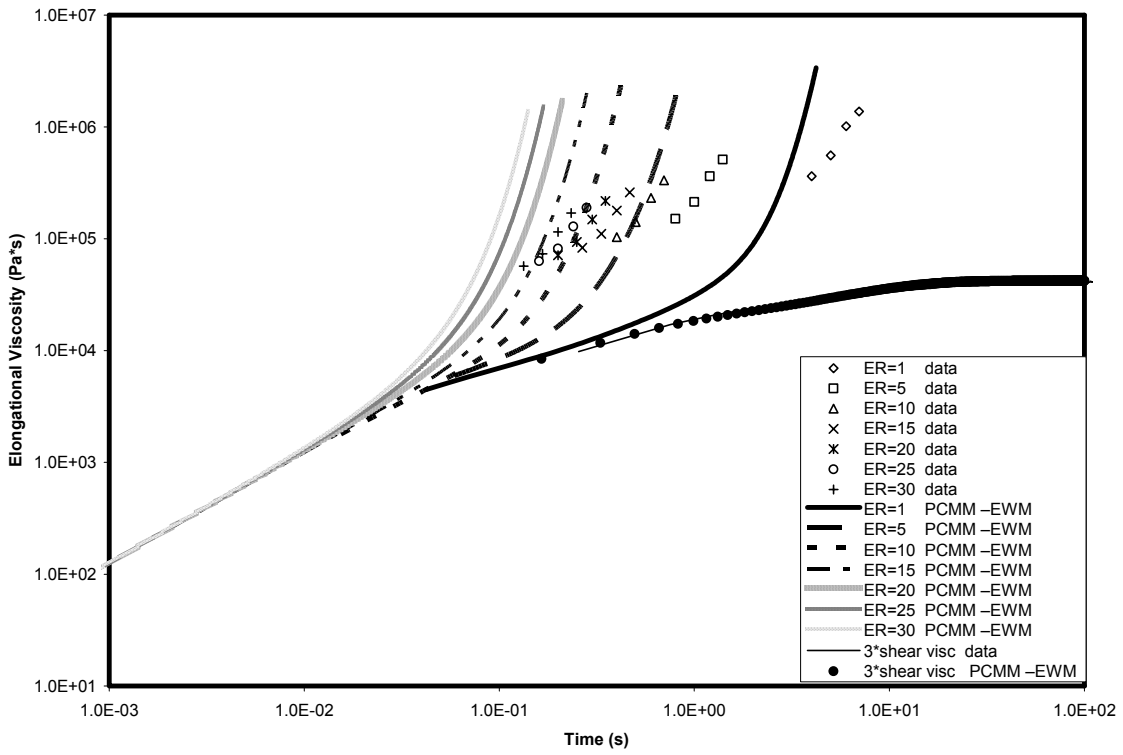

Figure 4.13: Elongational viscosity as a function of time, as predicted with the PCMM-EWM Model.

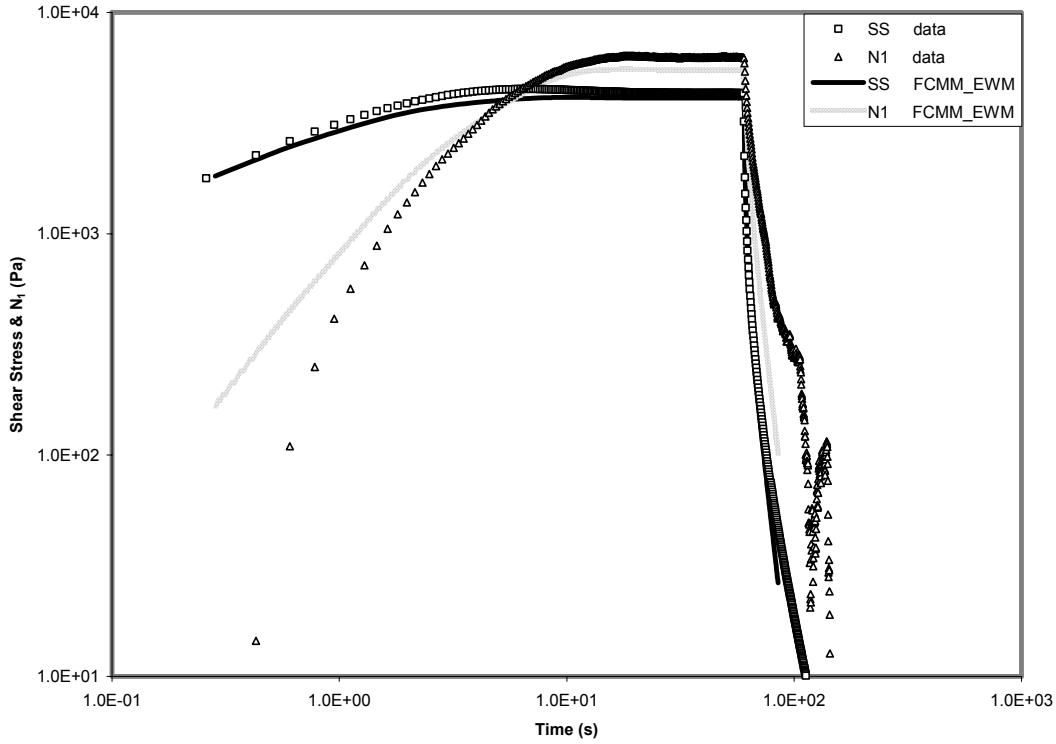

Figure 4.14: Transient stress as functions of time, as predicted with the FCMM-EWM Model ($\dot{\gamma} = 0.5 s^{-1}$).

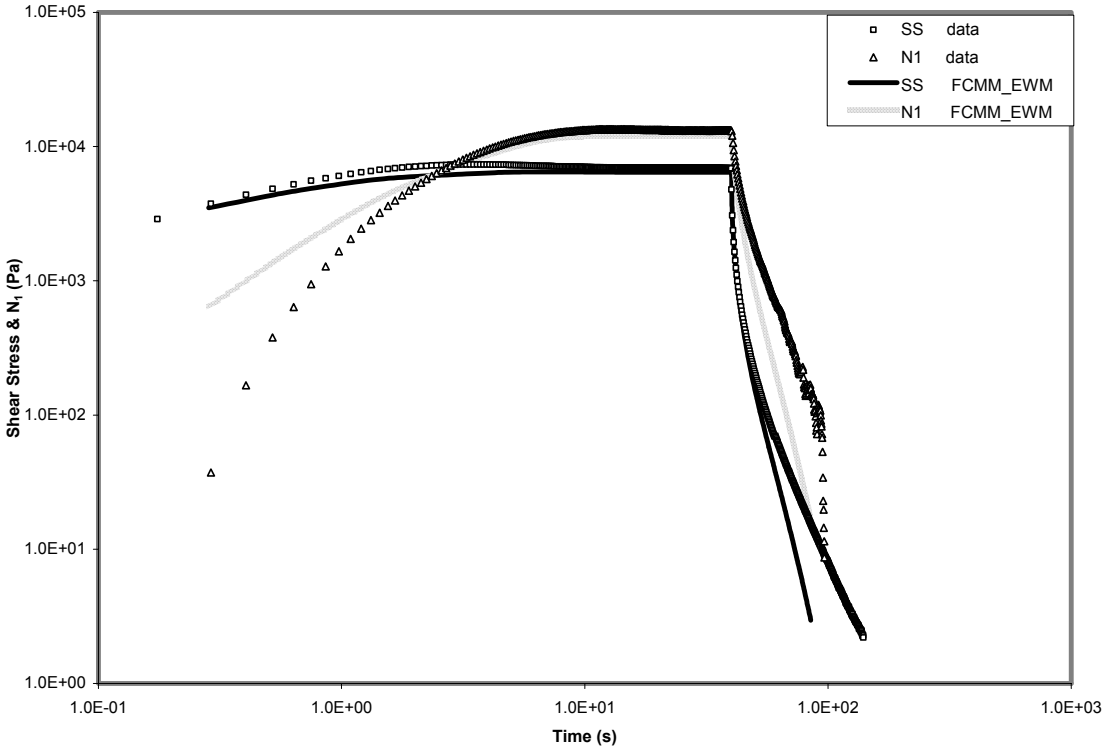

Figure 4.15: Transient stress as a functions of time, as predicted with the FCMM-EWM Model ($\dot{\gamma} = 1.0\, s^{-1}$).

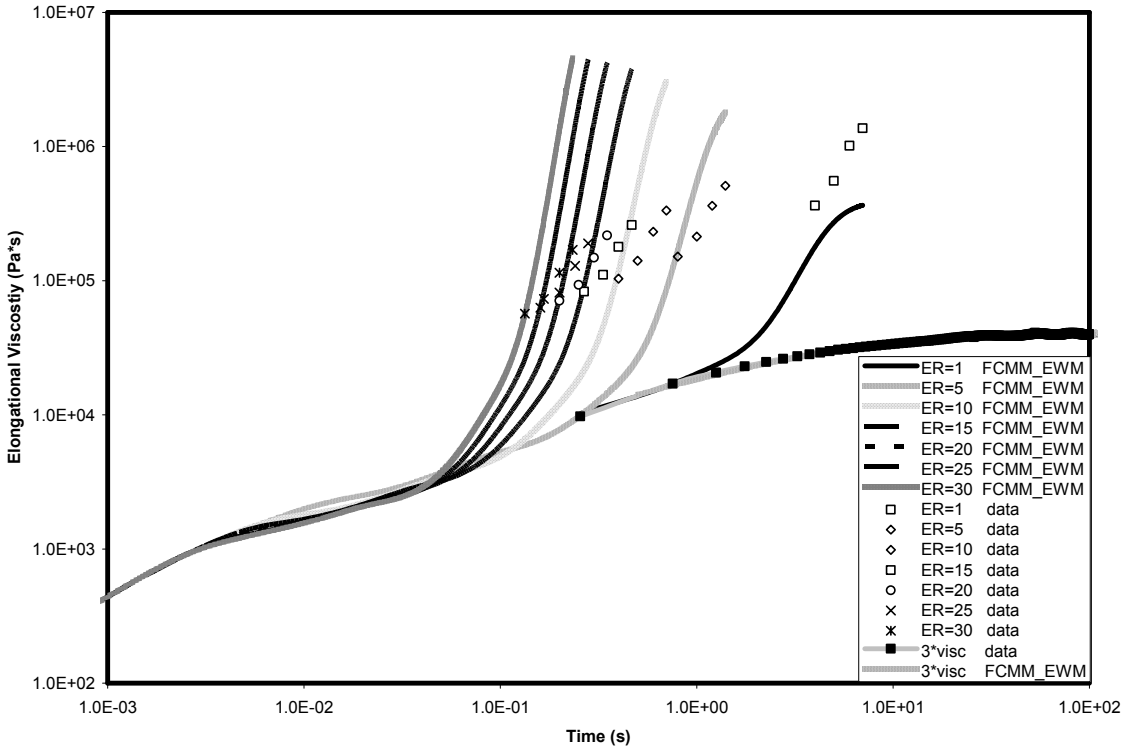

Figure 4.16: Elongational viscosity as a function of time, predicted with the FCMM-EWM Model.

PART 5

Using Multiple-Mode Models for Fitting and Predicting the Rheological Properties of Polymeric Melts: Single and Double Step-Strain Flows

5.1 Introduction

Single and double step-strain flows are convenient and powerful methods to evaluate rheological constitutive equations [5.1,5.2]. In a single step-strain experiment, a shear strain of γ is imposed on the test sample at $t = 0$, on the condition that $\gamma = 0$ for $t < 0$. The shear stress, $\sigma(\gamma, t)$, is measured as a function of time. As for a double step-strain experiment, a shear strain of γ_1 is imposed on the test sample at $t = 0$, on the condition that $\gamma = 0$ for $t < 0$; then a second step of strain γ_2 is imposed at $t = t_1 > 0$. The extra stress $\sigma(\gamma_1, \gamma_2, t_1, t)$ is monitored as a function of time.

Descriptions of double step-strain data have focused on the well-known non-linear and time-dependent BKZ model proposed by Bernstein et al. [5.3] and the reptation model of Doi and Edwards (DE) [5.4]. Many studies have lead to the similar conclusion that the BKZ model cannot describe quantitatively reversing flows for entangled linear polymers [5.5]. Venerus and Kahvand [5.6] carried out a thorough evaluation of DE Theory using double step-strain flow of monodisperse polystyrene (PS) solutions. Also, predictions of several models in reversing shear flows were given by Wagner and Ehrecke [5.7]. Chodankar, Schieber, and Venerus [5.8] examined the integral and differential Pom-pom Model in single and double step-strains about the behavior of a low-density polyethylene (LDPE) melt in double-step strain flows. Semi-analytic model predictions were obtained for the stresses in double step-strain shear flows [5.8].

In Part 4 [5.9], we examined the performance of several multi-mode constitutive equations in small-amplitude oscillatory shear flow (SAOSF), steady-state and transient

shear flow, and elongational flow. Further information is expected to be attained through single and double step-strain flows. The main premise of a double step-strain experiment is the following: a given step strain is applied to a sample, after which the sample begins to relax; after is has partially, but not fully, relaxed, a second step strain is applied to the sample. Hence, right before application of the second step strain, some of the modes (with short relaxation times) will have completely relaxed, while those modes with long relaxation times will not have done so. If all modes are independent, then the long time modes will have no effect on the short time modes. However, if mode coupling occurs, some unusual hysteresis phenomena might be observed under certain conditions.

In this part, we predict the stress of step-strain experiments through the strain data using the parameters attained by fitting the data of SAOSF and steady-state shear flows in Part 4 [5.9]. The performance of different models in step-strain experiments is examined herein. Keep in mind that all theoretical results presented in this paper are predictions of experimental data; i.e., all parameter fitting was performed in Part 4 [5.9] for SAOSF and steady-shear flow.

5.2 Experiment

The system studied herein was the same polymer described in the previous Part [5.9]. It was a typical, industrially relevant, low-density polyethylene (LDPE) sample. The LDPE sample was obtained from Exxon. It was prepared using a Ziegler-Nata catalyst. This sample has a wide molecular weight distribution. (The value of the polydispersity index is 5.15.) Its melt index was 0.2 g/minute, with a density of 0.923

g/cm^3. The weight-average molecular weight was 80,350 g/mol, as measured by gel permeation chromatography.

The experiments were conducted using standard rheological testing equipment and procedures at the University of Tennessee. Step-strain measurements of relaxation stress and the corresponding strain were made on the Advanced Rheometrics Expansion System (ARES) by Rheometrics Scientific™ at 175°C. The cone and plate fixture with 25mm plate diameter and 0.1rad cone angle was used for both single and double step-strain experiments.

5.3 Computational methods

A number of multiple-mode rheological models were discussed and examined for the same sample in Part 4 [5.9], which presented the corresponding constitutive equations for the rheological models examined: the Uncoupled Maxwell Modes (UMM) Model, the Uncoupled Extended White/Metzner (UEWM) Model, the Uncoupled Giesekus Modes (UGM) Model, the Pair-wise Coupled Maxwell Modes (PCMM) Model, the Pair-wise Coupled Maxwell Modes Model with the White/Metzner-like extension (PCMM-EWM), the Fully-Coupled Maxwell Modes (FCMM) Model, and the FCMM Model with the White/Metzner-like extension (FCMM-EWM Model). The parameters of all models were attained by fitting experimental data of storage and loss moduli in SAOSF and steady-state shear viscosity simultaneously. All the parameters for each model are listed in Part 4 [5.9].

A schematic diagram of strain versus time is shown in Figure 5.1[4], which demonstrates that, theoretically, an instantaneous strain, γ_0, is applied at time $t = 0$. However, experimentally, the rheometer needs a certain amount of time (about 0.07 s) to reach the strain required. The corresponding shear rate can be attained through the strain data; therefore, the shear stress can be computed theoretically through the constitutive equations of the different models mentioned above.

In Refs. [5.5, 5.10], the stress relaxation modulus, $G(t,\gamma)$, is defined as the ratio of the resulting stress to theoretical step-strain: $G(t,\gamma) = \sigma(t,\gamma)/\gamma_0$. We defined the stress relaxation modulus, $G(t,\gamma)$, as the ratio of the resulting stress to experimental step-strain: $G(t,\gamma) = \sigma(t,\gamma)/\gamma$, since we must consider the initial time for the instrument to reach the applied strain, as discussed later.

5.4 Results and discussion

5.4.1 Single Step-Strain Experiments

Figure 5.2 shows the time dependence of shear stress and stress relaxation modulus under various step-strains. For the applied strains (γ=0.01, 0.08, 0.20), the value of stress increases quickly and reaches a maximum in less than 0.1s, then decreases as the polymer melt relaxes after the strain reaches the value applied. The value of the stress relaxation modulus decreases right after the strain is applied. Moreover, the values of the various stress relaxation moduli overlap, which means that the stress relaxation

[4] All the tables and figures are located in the appendix at the end of the part

moduli obey time-strain factorability. Furthermore, the stress relaxation moduli are not related to strain in the region of strain examined.

Theoretical results of stress and stress relaxation moduli were computed through the various models defined in Ref. [5.9]: the UMM, UGM, UEWM, PCMM, FCMM, PCMM-EWM and FCMM-EWM Models. Predictions of these models for the stress modulus are presented along with experimental data for three different strains in Figures 5.3-5.9. Figure 5.3 demonstrates that the UMM Model can predict the stress and stress relaxation modulus fairly well for the different strains, except that this model underpredicts them in the long time region ($t > 19.5\,\mathrm{sec}$). This implies that the UMM Model does not have a large enough relaxation time, as discussed in Part 4 [5.8]. The UMM Model shows the same time-strain factorability as the experimental data.

Figures 5.4 and 5.5 present the PCMM and FCMM Models, which predict the stress and stress relaxation modulus with noticeable waves in the curve. These waves can be explained as a further example of the coupling effects in these models, as explained in Part 3 [5.10]. Recall that the waviness in Part 3 was associated with the unrealistic Maxwell-type relaxation behavior. Both the PCMM and FCMM Models underpredict stress and modulus in the long time region ($t > 1.2\,\mathrm{sec}$), and show the same time-strain factorability.

Figure 5.6 presents the theoretical results of stress and modulus predicted by the UGM Model. This figure shows that the UGM Model can describe the time-variation of the stress and stress relaxation modulus fairly well for the different strains, although some small deviations exist around 10s. The UGM Model also demonstrates time-strain factorability.

Figure 5.7 shows the UEWM Model can predict the time-variation for stress and stress relaxation modulus fairly well for the different strains, although some small deviations exist again around 10s; however, the UEWM Model shows some noticeable deviations from time-strain factorability.

In Figure 5.8, predictions for the stress and stress relaxation modulus from the PCMM-EWM Model are compared to the experimental data. Good consistency is found between the prediction from this model and the experimental data for the different strains, although again some small deviations exist around 10 s. The PCMM-EWM Model also demonstrates time-strain factorability. Figure 5.9 shows the prediction of the stress and stress relaxation modulus from the FCMM-EWM Model and the experimental data. From this figure, we see that the FCMM-EWM Model gives a very good prediction, and also shows time-strain factorability. The FCMM-EWM Model outperforms the other models examined in this subsection.

From Figures 5.3-5.9, we can conclude that: 1) all the models examined herein can generally describe the evolution of the relaxation moduli with time; 2) all the models except the UEWM Model demonstrate time-strain factorability, as in the experiments, but the different models do perform in peculiar ways; 3) the FCMM-EWM Model predicts the experimental data the best of these models, and 4) all the models with the White/Metzner extension (UEWM, PCMM-EWM, and FCMM-EWM) give a better prediction for the stress and modulus than the corresponding models without this extension (UMM, PCMM, and FCMM). This demonstrates that non-linearity of the relaxation modes is very important for describing polymer melts.

5.4.2 Double Step-Strain Experiments

Generally there are two types of double step-strain experiments: Type I is when the total strain, γ_2, after the second strain is larger than the first applied strain, γ_1; Type II is when γ_2 is smaller than γ_1. The latter case is often called a "reversing double step-strain experiment." We examined both types of experiments. Since the performance of each model after the first step is virtually the same as in single step-strain experiment, except that the time for relaxation of the polymer melt is much shorter, we will focus our attention on times after the application of the second step.

5.4.2.1 Result of Type I ($\gamma_2 > \gamma_1$) Double Step-Strain Experiments

Results for the stress computed using the UMM, PCMM, FCMM, and UGM Models for the Type I experiment ($\gamma_1 = 0.15$ and $\gamma_2 = 0.30$) are shown in Figure 5.10. Theoretical results from the UEWM, PCMM-EWM, and FCMM-EWM Models are shown in the Figure 5.11. These two figures show: 1) all the models can give a good prediction for the highest stress values, which appear right after the second strain is applied; 2) all the models can generally describe the time variation of the second-step stress; 3) both the PCMM and FCMM Models demonstrate some noticeable waves in the curves; 4) the corresponding PCMM-EWM and FCMM-EWM Models give a better prediction than the PCMM and FCMM Models; 5) the PCMM-EWM, UEWM, and UGM Models overpredict the stress in the time region ($6 < t < 18$); 6) the UMM Model gives a fairly good prediction; and 7) the FCMM-EWM Model gives the best prediction among these models.

5.4.2.2 Results of Type II ($\gamma_2 < \gamma_1$) Double Step-Strain Experiments

Results predicted using the UMM, PCMM, FCMM, and UGM Models for the Type II experiment ($\gamma_1 = 0.30$ and $\gamma_2 = 0.15$) are shown in Figure 5.12, and the corresponding results using the UEWM, PCMM-EWM, and FCMM-EWM Models are shown in Figure 5.13. Since the stress value right after the application of the second strain in Type II experiment changes sign, we present the absolute values of the stress as functions of time on a log-log scale. It is noted that the values of stress are negative between the start of the application of the second strain, and the point where the values of stress revert to positive sign at longer times.

Figures 5.12 and 5.13 demonstrate that: 1) all the models can give a good prediction for the largest absolute values of the stress, which appear right after the second strain is applied (as identified by the summit in the curves); 2) all the models can generally describe the trend of the second-step stress evolution in time; 3) the stress values from the PCMM and FCMM Models revert to positive sign much sooner than the experimental data, and those from the UEWM Model revert to positive sign slightly before the experimental data. These three models underpredict the absolute values of the stress in the regions before the stress reverts to positive sign. The predictions of the UGM and PCMM-EWM Models revert to positive sign after the experimental data. The UMM and FCMM-EWM Models give very good predictions for the time when the stress values change sign. All the models examined give a higher prediction for the largest positive value of the stress, except for the FCMM-EWM Model. The performance of the models for predicting the time for the stress to achieve its maximum positive value is similar to the performance for the time the stress values change sign. Overall, the UMM

and FCMM-EWM Models give a fairly good prediction for the double step-strain experiment.

5.4.2.3 Results of a Special Case ($\gamma_2 = 0$) in Type II Double Step-Strain Experiments

In the special case ($\gamma_2 = 0$) of the Type II double step-strain experiment, most polymeric fluids satisfy the consistency relation (called the "Osaki-Kimura Relation") $\frac{N_1(\gamma_1, t, t_1)}{\sigma(\gamma_1, t, t_1)} = -\gamma_1$, where $N_1(\gamma_1, t, t_1)$ is the first normal stress difference and $\sigma(\gamma_1, t, t_1)$ is the shear stress after the second strain is applied [5.11, 5.12]. Here, we checked this consistency relationship for our polymer melt. Unfortunately, we could not obtain the experimental data for the first normal difference in the double step-strain experiment due to device limitations. What we could do, however, was to check whether the predictions of the different models obey this consistency relation.

Results of the stress predicted using the UMM, PCMM, FCMM, and UGM Models for the Type II experiment ($\gamma_1 = 0.30$ and $\gamma_2 = 0$) are shown in Figure 5.14. The corresponding results using the UEWM, PCMM-EWM, and FCMM-EWM Models are shown in Figure 5.15. The shear stress is plotted as the absolute values of stress as functions of time in Figures 5.14 and 5.15. It is noted that the values of stress are negative after the application of the second strain. Figures 5.14 and 5.15 demonstrate that all the models can give a good prediction for the largest absolute value of the negative stress. Also, all the models can generally describe the trend of the stress evolution with time. The stress from the PCMM and FCMM Models demonstrates some waviness, as usual: the PCMM and FCMM Models first underpredict for $t = 1.2 - 2.0$,

then overpredict for $t = 2.0 - 10$, and then underpredict the stress for all later times. The PCMM-EWM Model demonstrates some waviness, as do the PCMM and FCMM Models. The FCMM-EWM Model overpredicts the stress for $t > 2.7$. The UMM, UEWM, and UGM Models give very good predictions at all other times.

In Figure 5.16, the ratio $\frac{N_1(\gamma_1,t,t_1)}{\sigma(\gamma_1,t,t_1)}$ is shown as a function of time. From the Osaki-Kimura Relation, this ratio should be $-\gamma_1$, and in this case it is -0.3. From Figure 5.16, we see that the UMM, UEWM, and UGM Models give fairly good predictions for $\frac{N_1(\gamma_1,t,t_1)}{\sigma(\gamma_1,t,t_1)}$, which are very close to -0.30. (Note that the curves for the UGM and UEWM Models overlap.) The FCMM Model gives a close prediction, -0.29, but the PCMM and PCMM-EWM Models give a lower value, around -0.24. The FCMM-EWM Model gives the lowest value, -0.13, among the models examined. The graph also shows that the value of $\frac{N_1(\gamma_1,t,t_1)}{\sigma(\gamma_1,t,t_1)}$ increases and then reaches a steady-state value after the application of the second strain for some models (UMM, UEWM, UGM, and FCMM), which all give a good prediction; on the other hand, the value of $\frac{N_1(\gamma_1,t,t_1)}{\sigma(\gamma_1,t,t_1)}$ increases and then reduces to a steady-state value after the application of the second strain for the remaining models (PCMM, PCMM-EWM, and FCMM-EWM), which give a poorer prediction.

5.5 Conclusion

The double step-strain experiment, especially the reversing double step-strain experiment, is a powerful tool to examine constitutive equations severely. Seven constitutive equations have been tested in this part. The FCMM-EWM Model has demonstrated a pretty good performance in both single and double step-strain experiments, except that this model gives a poor prediction of the value of $\frac{N_1(\gamma_1,t,t_1)}{\sigma(\gamma_1,t,t_1)}$. The UMM Model, which fits only linear rheological properties, gives a very good prediction in both experiments. Obviously then, the step-strain experiments conducted herein fall in the linear rheological region of the LDPE melt, which can be proven by the fact that the shear rates in the step-strain experiments are much lower than 10 s^{-1} where the Newtonian plateau ends in steady-shear experiments. Overall, the UGM Model showed the best performance in all aspects of the step-strain experiments. This is *not* a coupled-mode model. Since the coupling phenomenon is a non-linear one, and since the accessible range of step-strain experiments in our laboratory only encompassed the linear regime, we are unable to draw any additional conclusions (beyond those of Part 4) concerning the occurrence of mode coupling.

References

5.1 A. Goublomme, B. Draily, and M.J. Crochet, *J. Non-Newtonian Fluid Mech.*, 1992. **44**: p. 171.

5.2 M.J. Crochet, and A. Goublomme, *J. Non-Newtonian Fluid Mech.,* 1993. **47**: p. 281.

5.3 B. Bernstein, E.A. Kearsley, and L.J Zapas, Trans. *Soc. Rheol.*, 1963. **7**: p. 391.

5.4 M. Doi, and S.F. Edwards, *J. Chem. Soc. Faraday Trans*. 2, 1978. **74**: p. 1789, 1802, 1818.

5.5 R.G. Larson, *Constitutive Equations for Polymer Melts and Solutions*. 1988, Butterworth, Boston.

5.6 D.C. Venerus, and H. Kahvand, *J. Polym. Sci. Part B: Polym. Phys.*, 1994. **32**: p. 1531.

5.7 M.H. Wagner, and P. Ehrecke, *J. Non-Newtonian Fluid Mech.*, 1998. **76**: p. 183.

5.8 C.D. Chodankar, J.D. Schieber, and D.C. Venerus. *J. Rheol.* 47(2):413-427, 2003

5.9 B. Jiang, P.A. Kamerkar, D.J. Keffer, and B.J. Edwards, *J. of Appl. Polym. Sci.*, in press.

5.10 W.H. Li, H. Du, G.H. Yeo, and N.Q. Guo, *Smart Mater. Struct.*, 2002. **11**: p. 209.

5.11 B. Jiang, P.A. Kamerkar, D.J. Keffer, and B.J. Edwards, B.J., *J. Non-Newtonian Fluid Mech.*, 2004. **120**: p. 11.

5.12 D.C. Venerus, and H. Kahvand, *J. Rheol.,* 1994. **38**(5): p. 1297.

5.13. K. Osaki, S. Kimura, and M. Kurata, *J. Rheol*., 1981. **25**: p. 549.

Appendix

Figures

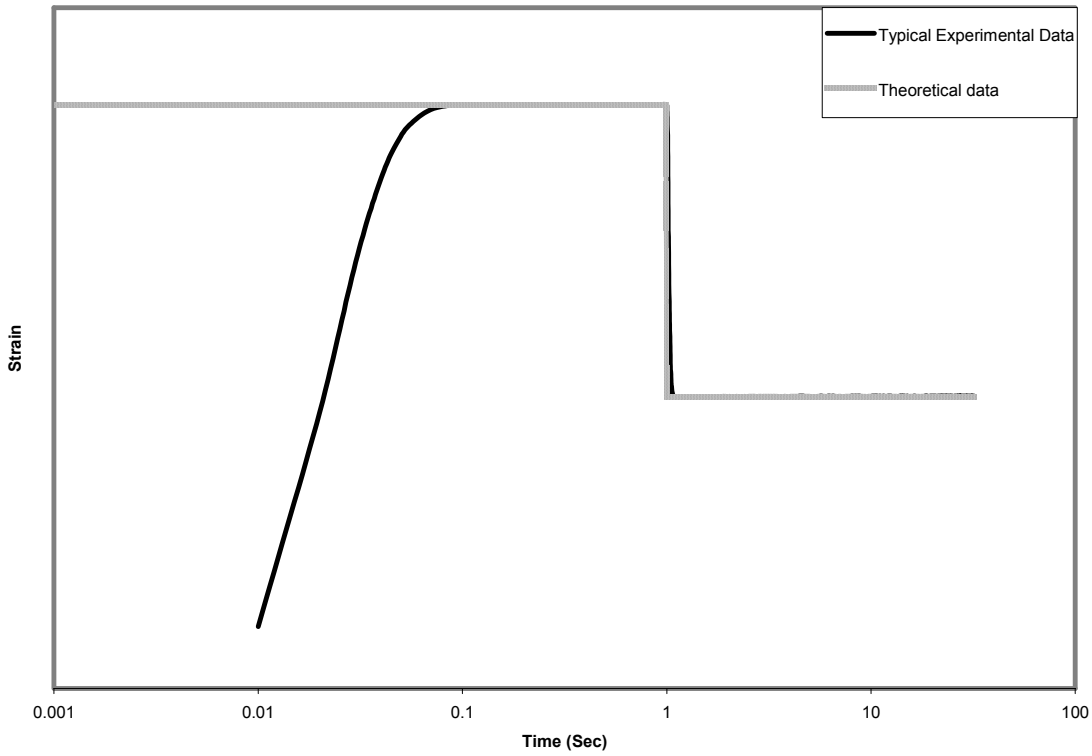

Figure 5.1: Typical variation of strain with time in step-strain shear flow both theoretically and experimentally.

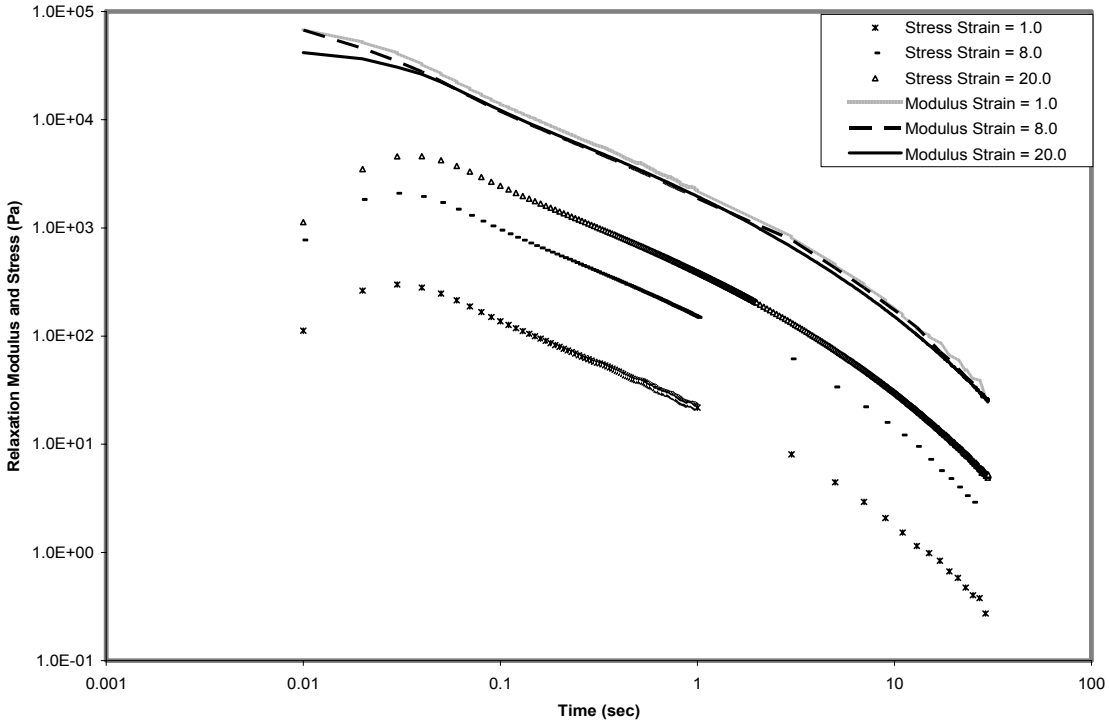

Figure 5.2: Experimental data of stress and stress relaxation modulus versus time in single step-strain experiments at strains of 1, 8, and 20%.

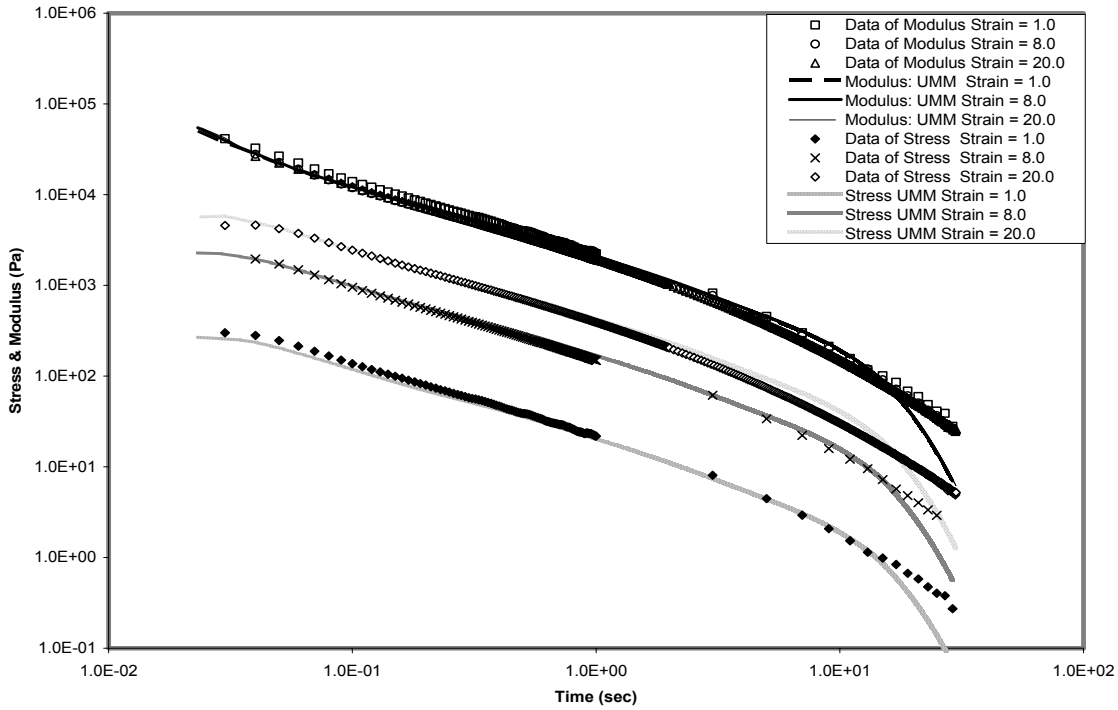

Figure 5.3: Stress and stress relaxation modulus versus time, as predicted with the UMM Model, in single step-strain experiments at strains of 1, 8, and 20%.

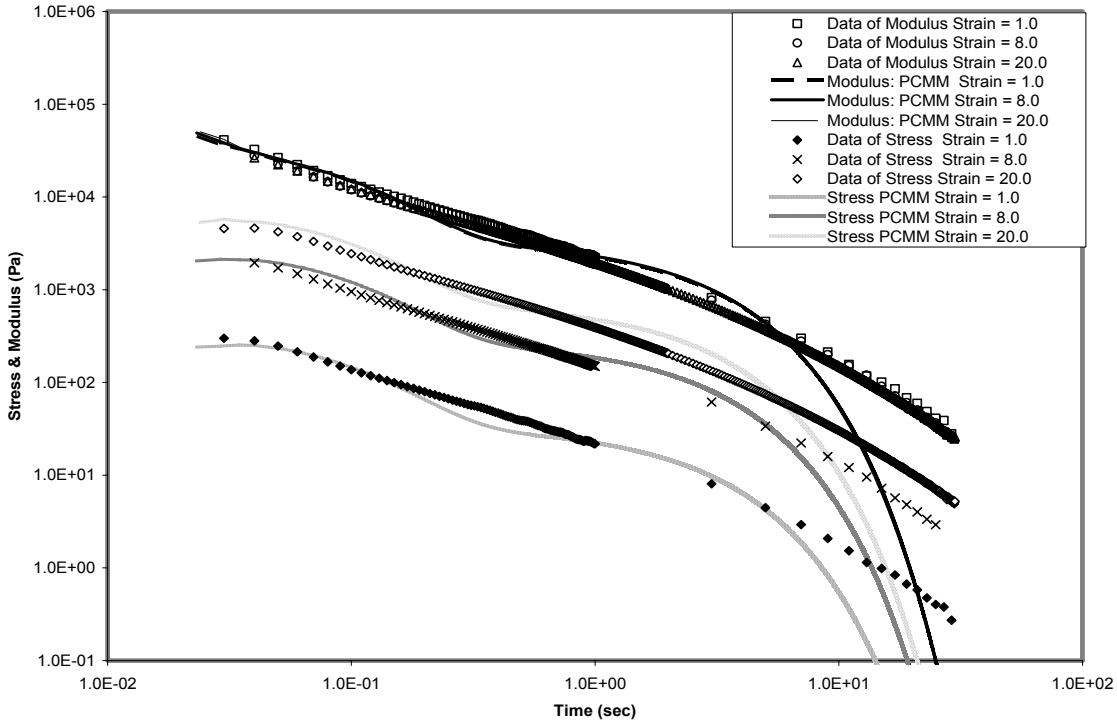

Figure 5.4: Stress and stress relaxation modulus versus time, as predicted with the PCMM Model, in single step-strain experiments at strains of 1, 8, and 20%.

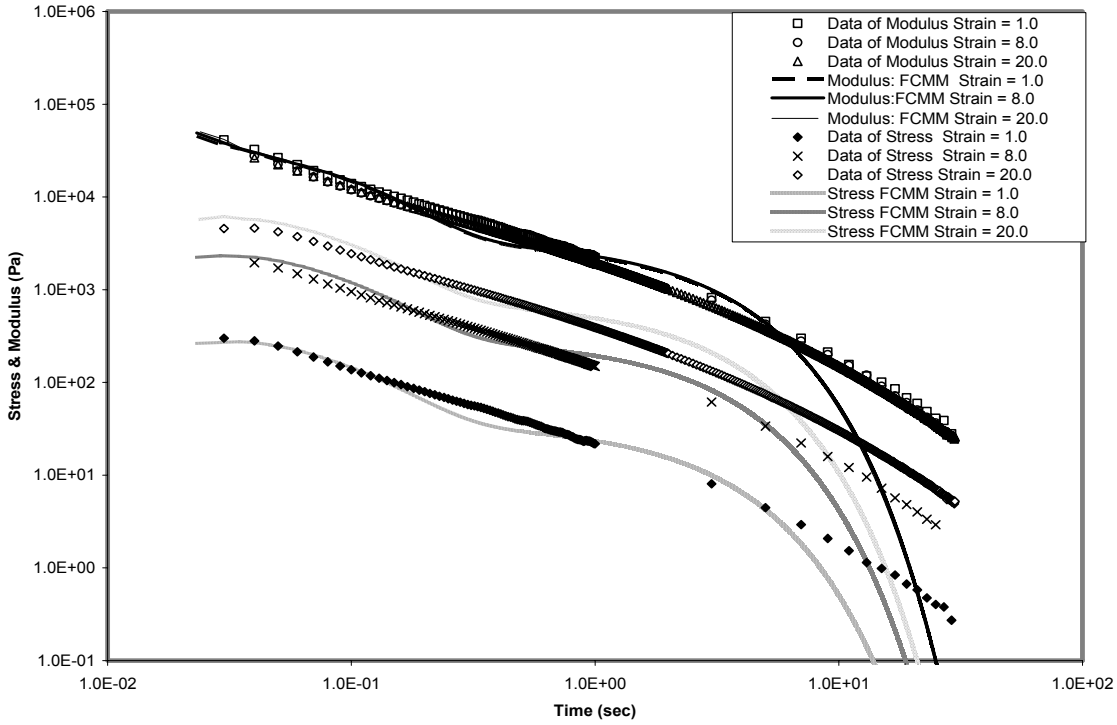

Figure 5.5: Stress and stress relaxation modulus versus time, as predicted with the FCMM Model, in single step-strain experiments at strains of 1, 8, and 20%.

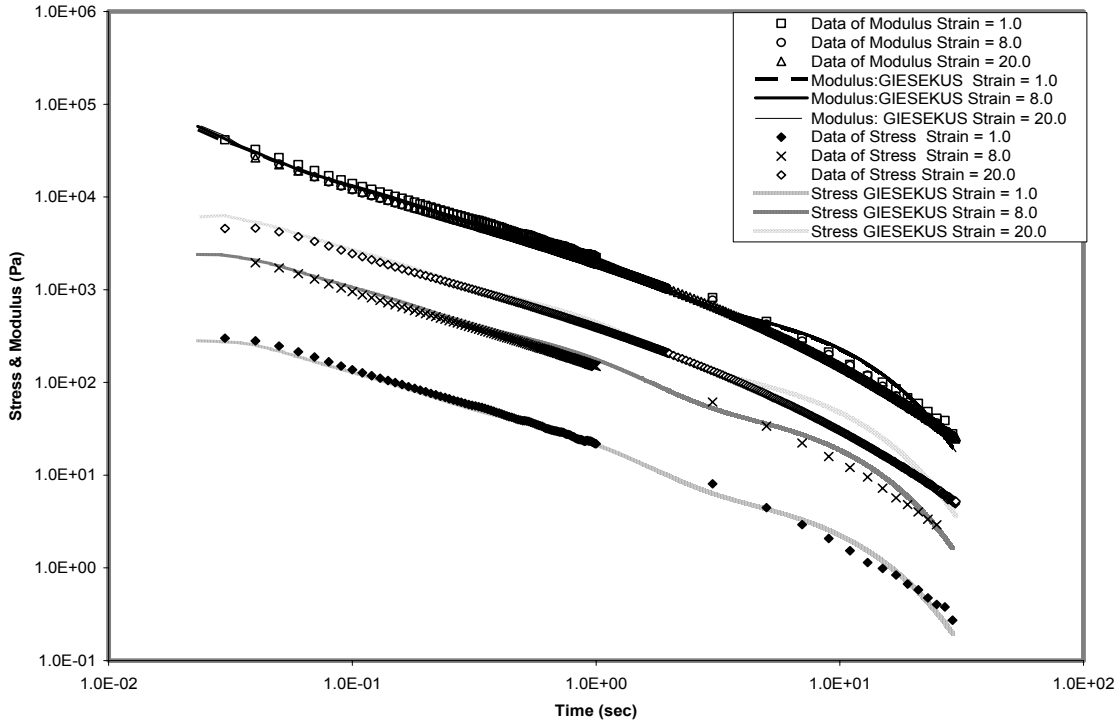

Figure 5.6: Stress and stress relaxation modulus versus time, as predicted with the UGM Model, in single step-strain experiments at strains of 1, 8, and 20%.

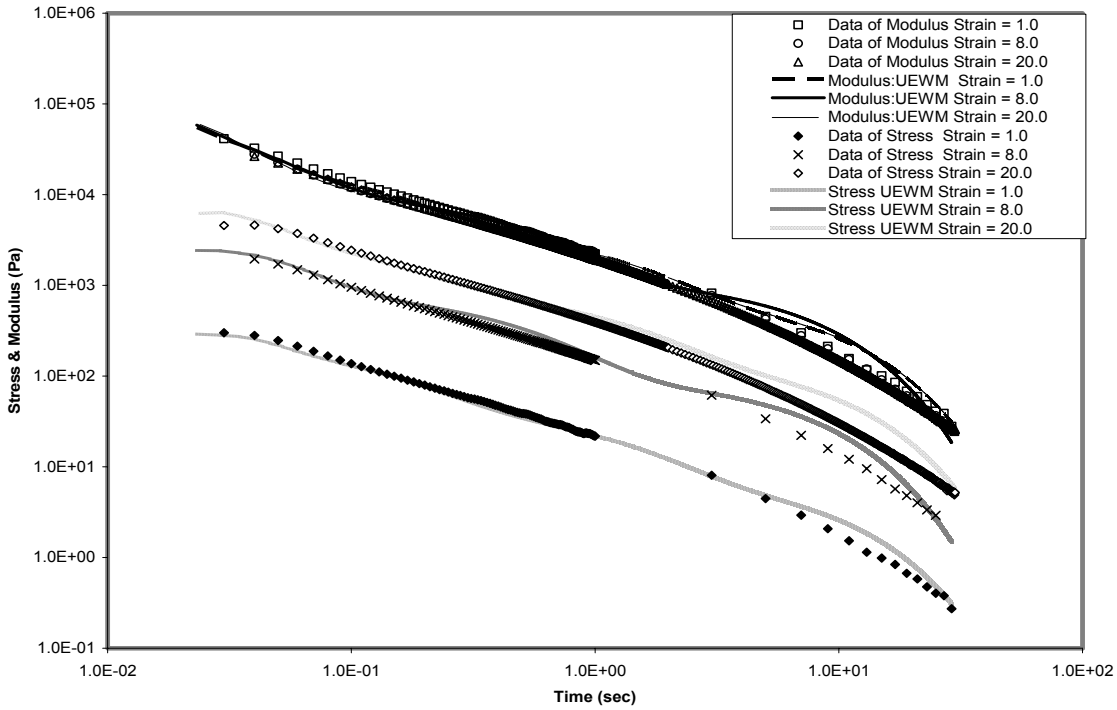

Figure 5.7: Stress and stress relaxation modulus versus time, as predicted with the UEWM Model, in single step-strain experiments at strains of 1, 8, and 20%.

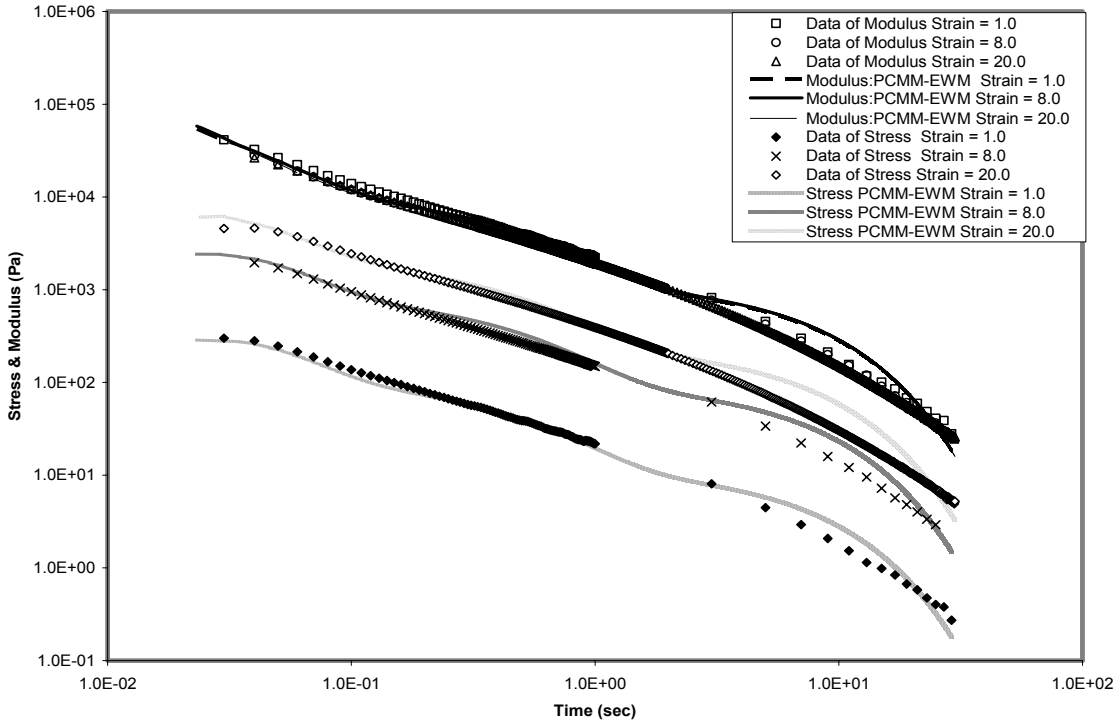

Figure 5.8: Stress and stress relaxation modulus versus time, as predicted with the PCMM-EWM Model, in single step-strain experiments at strains of 1, 8, and 20%.

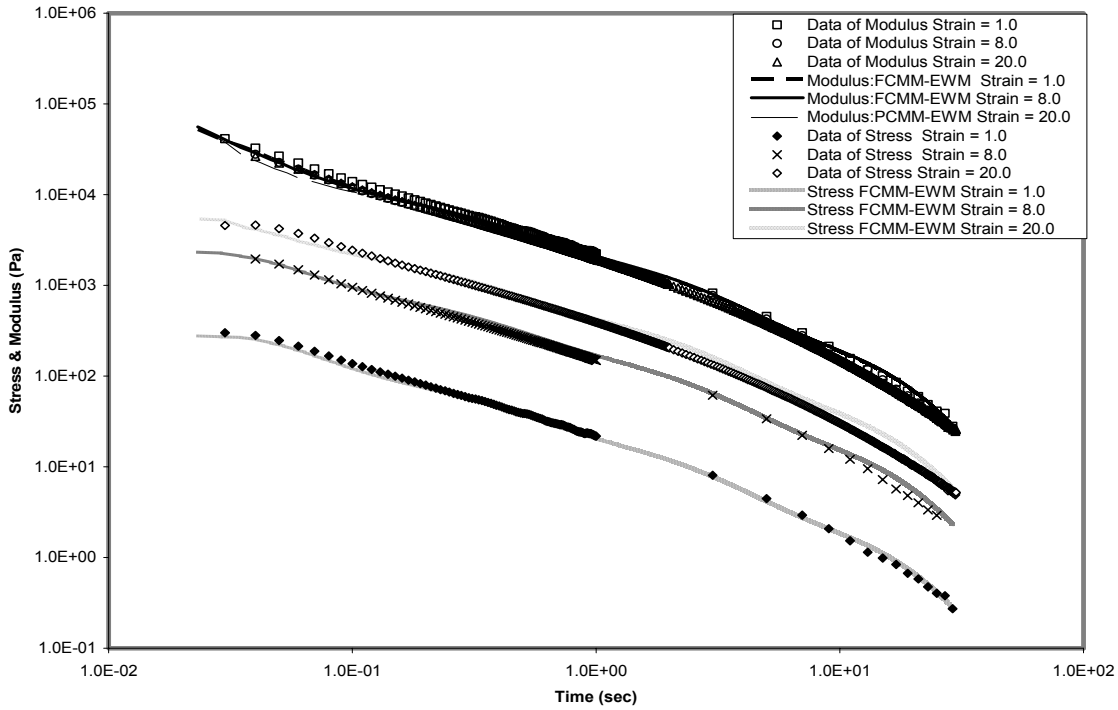

Figure 5.9: Stress and stress relaxation modulus versus time, as predicted with the FCMM-EWM Model, in single step-strain experiments at strains of 1, 8, and 20%.

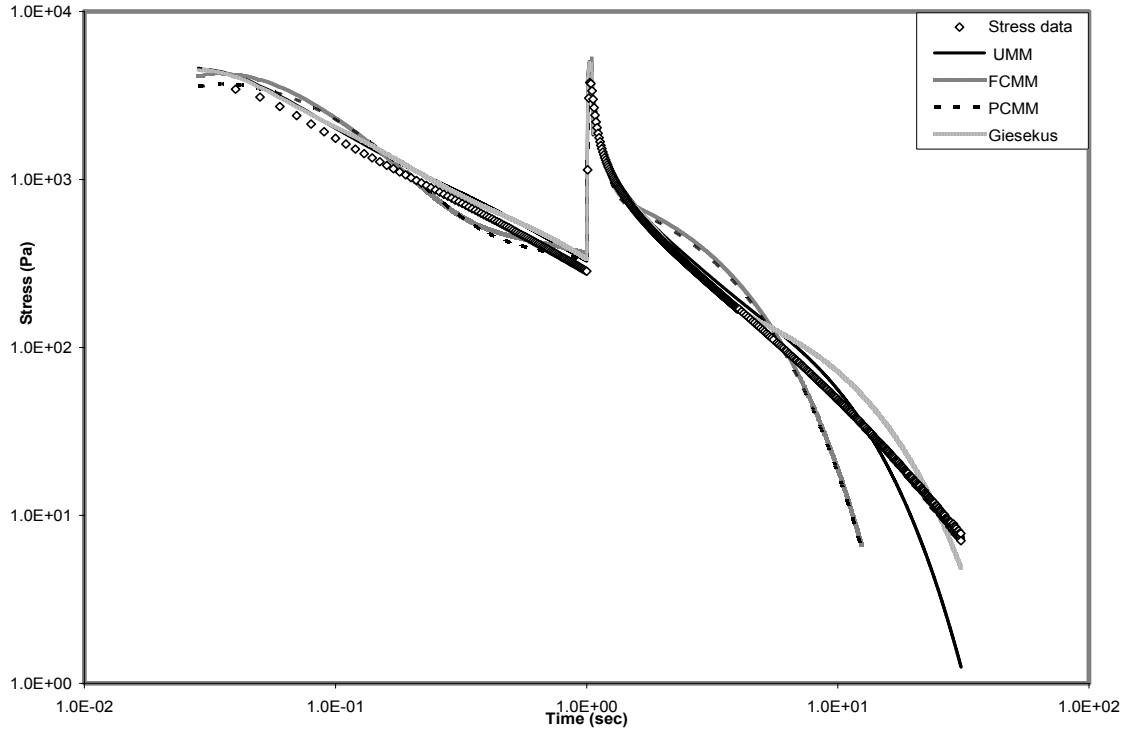

Figure 5.10: Stress versus time, as predicted with the UMM, PCMM, FCMM and UGM Models, in double step-strain experiments at strains $\gamma_1 = 15\%$ and $\gamma_2 = 30\%$.

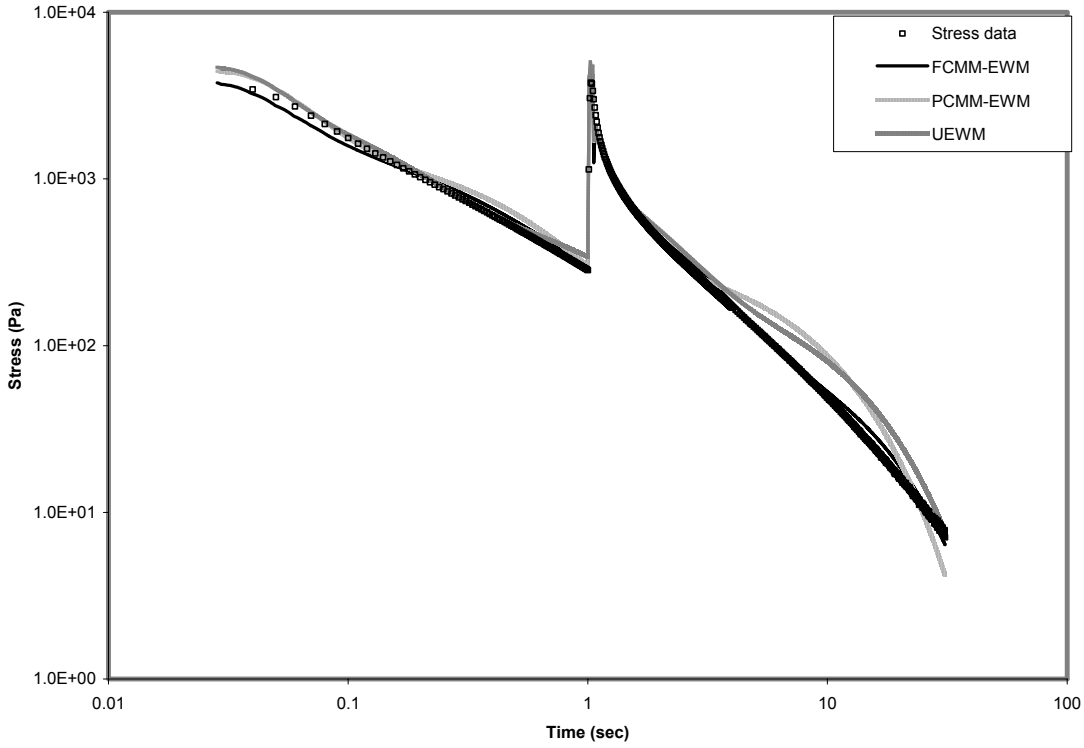

Figure 5.11: Stress versus time, as predicted with the UEWM, PCMM-EWM, FCMM-EWM Models, in double step-strain experiments at strains $\gamma_1 = 15\%$ and $\gamma_2 = 30\%$

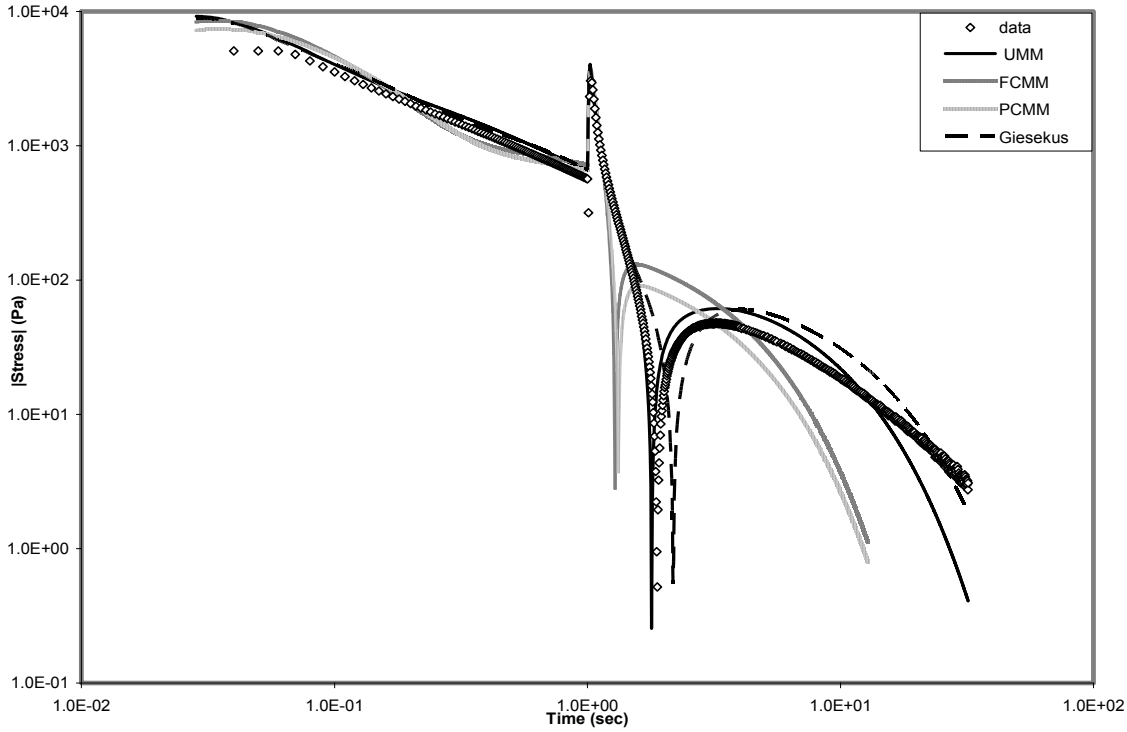

Figure 5.12: Stress versus time, as predicted with the UMM, PCMM, FCMM and UGM Models, in double step-strain experiments at strains $\gamma_1 = 30\%$ and $\gamma_2 = 15\%$.

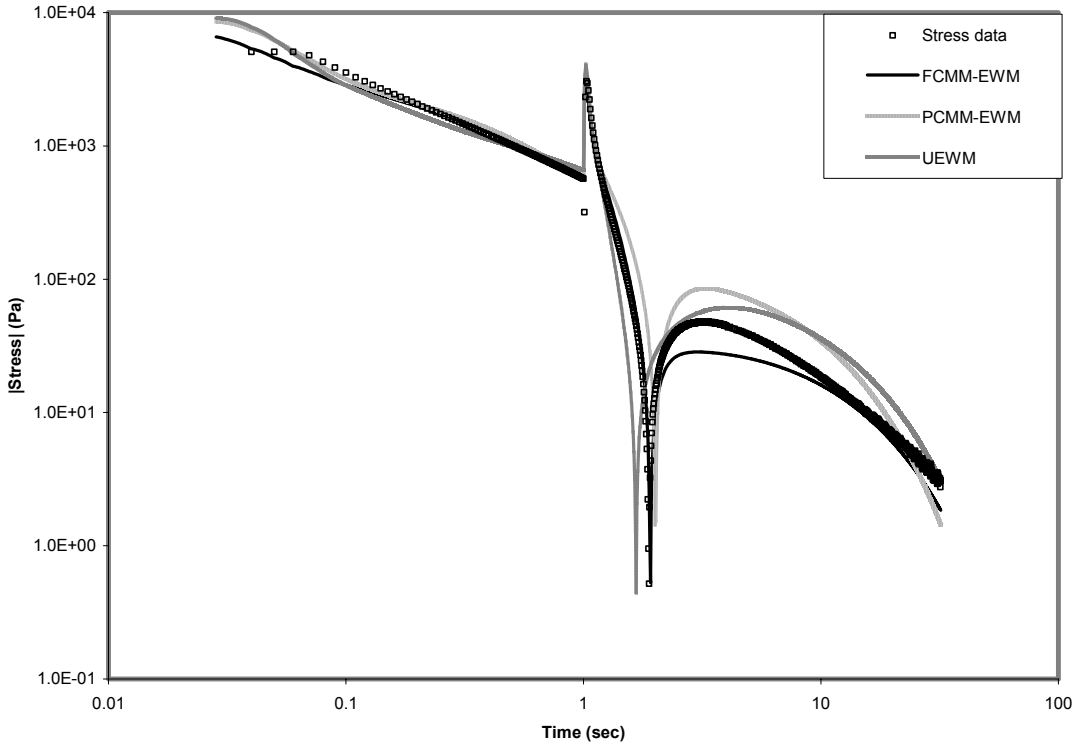

Figure 5.13: Stress versus time, as predicted with the UEWM, PCMM-EWM, FCMM-EWM Models, in double step-strain experiments at strains $\gamma_1 = 30\%$ and $\gamma_2 = 15\%$.

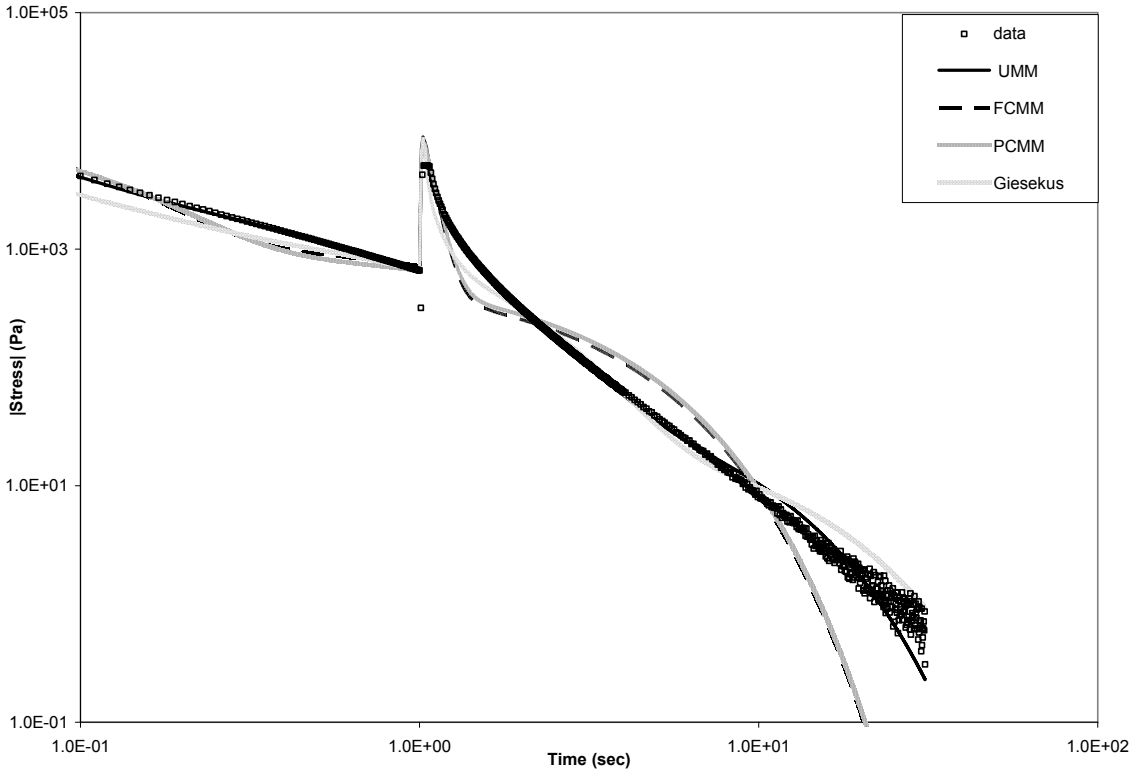

Figure 5.14: Stress versus time, as predicted with the UMM, PCMM, FCMM and UGM Models, in double step-strain experiments at strains $\gamma_1 = 30\%$ and $\gamma_2 = 0$.

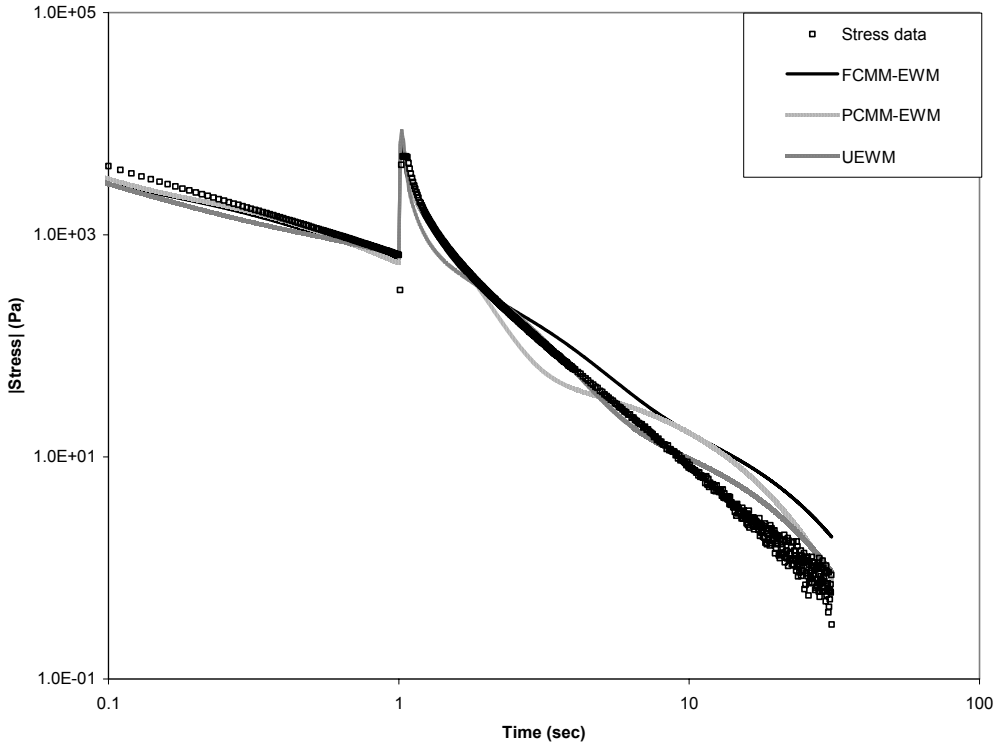

Figure 5.15: Stress versus time, as predicted with the UEWM, PCMM-EWM, FCMM-EWM Models, in double step-strain experiments at strains $\gamma_1 = 30\%$ and $\gamma_2 = 0$.

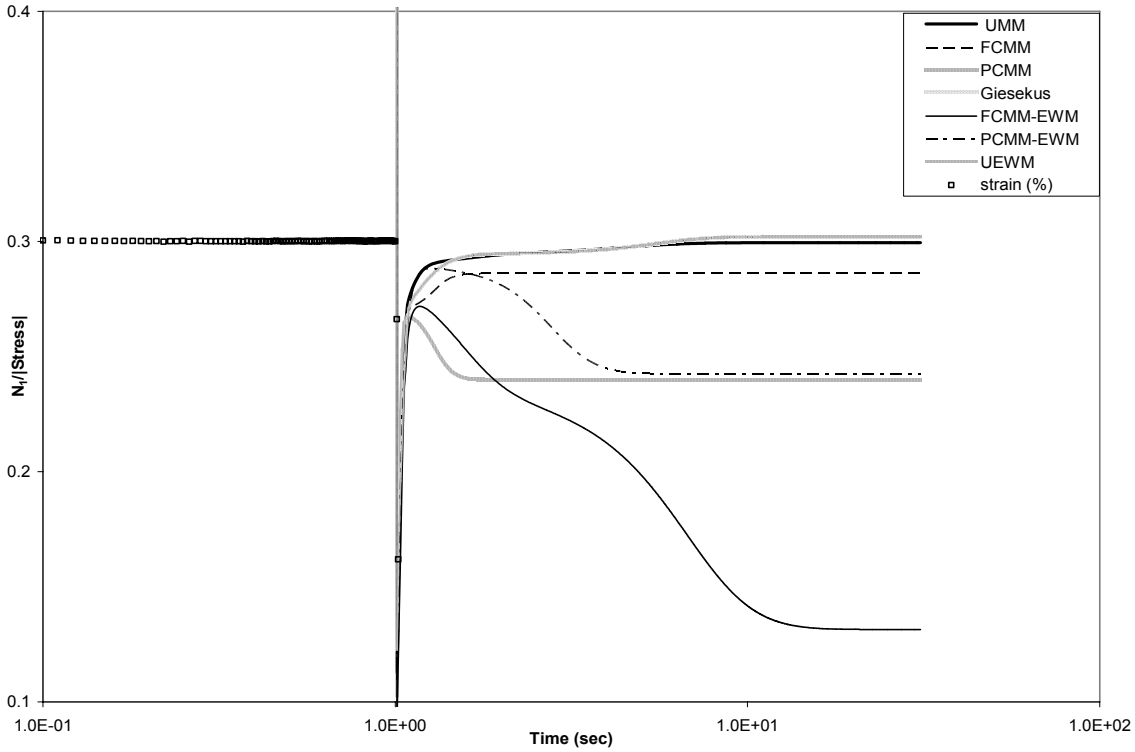

Figure 5.16: Ratio between first normal stress difference and stress versus time, as predicted for seven models, in double step-strain experiments at strains $\gamma_1 = 30\%$ and $\gamma_2 = 0$.

PART 6

The Performance of Finitely Extensible Nonlinear Elastic Springs in Elongational Flow

6.1 Introduction

In Parts 3-5, the linearly elastic spring was taken as the basis for all models examined. The linearly elastic spring corresponds to the Hookean approximation of the contributions of intra-chain conformations [6.1,6.2]. However, when the stress applied to the polymer liquid is large enough, an anharmonic entropic spring force must be used to keep the chain contour length from increasing to unphysical values [6.3]. Finitely extensible, nonlinear elastic (FENE) springs are one of the more popularly non-linear force laws. The FENE spring force law is expressed as

$$F^c = \frac{KR}{1 - R^2 / R_0^2}, \qquad R < R_0 \tag{6.1}$$

where F^c is the spring force, K is the spring constant, R is end-to-end distance vector of the polymer chain, and R_0 is the maximum possible spring extension. The FENE spring will perform like a Hookean spring for small extensions [6.4].

Such an expression as Eq. (6.1) is usually of little interest because of its complexity in numerical computation. To simplify computation, the Peterlin Approximation is usually used, in which the spring force is calculated using a an average of the denominator [6.5,6.6]: $F^c = \frac{KR}{1 - \langle R^2 \rangle / R_0^2}$, with the angular brackets denoting an average over the orientational distribution function of the polymer chains. In this case, the FENE spring is known as the FENE-P spring.

In Parts 3-5, we have examined the performance of the different models in diverse flow fields, such as transient and steady shear flow, small amplitude oscillatory shear flow, and transient uniaxial elongational flow. Most of models can quantitatively

describe shear flow very well, but the models can only qualitatively predict the behavior of the polymeric liquid in transient elongational flow. In this part, we examine whether we can use FENE-P springs in the corresponding models of Parts 3-5 to improve the model performance in elongational flow. Evidence in the literature [6.2] suggests that the FENE-P springs might act to alter the slope of the elongational viscosity versus time curves, thus allowing better fits of this quantity to be obtained relative to the linear springs.

6.2 Theory

We have described the basic concept of FENE-P springs in Sec. 6.1. Here, we will describe the FENE-P model in detail in terms of the conformation tensor. In the FENE-P Model, the extra stress tensor can be calculated through the equation [6.5]

$$\sigma_{\alpha\beta} = nK \frac{R_0^2}{R_0^2 - \mathrm{tr}(\mathbf{C})} C_{\alpha\beta} - nk_B T \delta_{\alpha\beta} \tag{6.2}$$

where σ is extra stress tensor, K, R_0 have the same meaning as in Eq. (6.1), $\mathbf{C}$ is the conformation tensor, k_B is Boltzmann's constant, n is the modal concentration, δ is the Kronecker delta function, T is absolute temperature, and $\mathrm{tr}(\mathbf{C})$ stands for the trace of the conformation tensor. We use the conformation tensor, instead of the extra stress tensor, as our primary variable for FENE-P springs since the force law of this model is nonlinear; i.e., the relationship between σ and $\mathbf{C}$ is highly nonlinear, and hence Eq. (6.2) cannot easily be inverted for $\mathbf{C}$ as a function of σ.

In our calculations, we use the dimensionless conformation tensor, $\widetilde{\mathbf{C}} = \frac{K\mathbf{C}}{k_B T}$, and the dimensionless maximum possible spring extension, $b = \frac{KR_0^2}{k_B T}$, so that Eq. (6.2) becomes [6.5]

$$\sigma_{\alpha\beta} = nk_B T \frac{b}{b - tr(\widetilde{C})} \widetilde{C}_{\alpha\beta} - nk_B T \delta_{\alpha\beta} \tag{6.3}$$

The corresponding evolution equation of the dimensionless conformation tensor can be expressed as

$$\overset{\nabla}{\widetilde{C}}_{\alpha\beta} = -\frac{1}{\lambda} \frac{b}{b - tr(\widetilde{C})} \widetilde{C}_{\alpha\beta} + \frac{1}{\lambda} \delta_{\alpha\beta} \tag{6.4}$$

where λ is the relaxation time and $\overset{\nabla}{\widetilde{C}}_{\alpha\beta}$ is the upper-convected time derivative of the dimensionless conformation tensor: $\overset{\nabla}{\widetilde{C}}_{\alpha\beta} = \frac{\partial \widetilde{C}_{\alpha\beta}}{\partial t} + v_\gamma \nabla_\gamma \widetilde{C}_{\alpha\beta} - \widetilde{C}_{\alpha\gamma} \nabla_\gamma v_\beta - \widetilde{C}_{\gamma\beta} \nabla_\gamma v_\alpha$.

In this Part, we also consider the Fully Coupled Multiple Modes Model with the White/Metzner-like extension (FCMM-EWM), and replace the linear springs of Part 4 with FENE-P springs. This model can be described using Eq. 6.3 and the following evolution equation of dimensionless conformation tensor:

$$\overset{\nabla}{\widetilde{C}}^i_{\alpha\beta} = -\frac{1}{\lambda_i} \frac{b^i}{b^i - tr(\widetilde{C}^i)} \widetilde{C}^i_{\alpha\beta} + \frac{1}{\lambda_i} \delta_{\alpha\beta} + \frac{\theta_{ij}}{2} \sqrt{\frac{n_j}{n_i \lambda_i \lambda_j}} (\widetilde{C}^i_{\alpha\gamma} \widetilde{C}^j_{\gamma\beta} + \widetilde{C}^j_{\alpha\gamma} \widetilde{C}^i_{\gamma\beta} - 2\widetilde{C}^i_{\alpha\beta}) \tag{6.5}$$

Here, θ_{ij} is the coupling factor between modes i and j. Recall that for the White/Metzner-like extension, the relaxation times change as functions of the conformation tensors. In terms of the dimensionless conformation tensor, the change of the relaxation time can be expressed as

$$\lambda_i(\widetilde{C}^i) = \lambda_{0,i}(tr(C^i) - 2)^{k_i} \tag{6.6}$$

where the power law index, k_i, is a small, negative constant.

6.3 Experimental data and computational procedure

In this part, we use the same experimental data as presented in Parts 3 and 4, for the same polymer melt. For each model with FENE-P springs, we keep all the parameters the same as in the corresponding model with linear springs, then optimize the new maximum chain extension parameters, $b_i = \frac{KR_0^2}{k_B T}$, to fit the elongational data. Then, we can compare the difference between the theoretical results and the experimental data in elongational flow. We also consider the FENE-P Model itself, which is just a UMM Model with FENE-P springs replacing the linear ones. In this case, we use the parameters of the UMM Model (given in Part 4) as the initial guess of the optimization routine. Then we optimize the b_i to fit the complex modulus, shear viscosity, and first normal stress coefficient, and then predict the elongational viscosity.

6.4 Results and discussion

In this section, we present the performance of two typical models, which were discussed above. All of the models examined in Part 4 were also tested in this part of the research with FENE-P springs replacing the linear ones.

6.4.1 The Performance of the FENE-P Spring in Shear Viscosity

As for the FENE-P Model, we limit the dimensionless maximum possible spring extension to $b_i \geq 10$, as described in Ref. [6.5]. We keep the same parameters of concentration and relaxation time from the UMM Model, which was examined in Part 4, then optimize the b_i to fit the shear viscosity and first normal stress coefficient. The parameters of the FENE-P Model are listed in Table 6.1[5].

In Figure 6.1, we plot the shear viscosity as a function of shear rate according to the FENE-P and UMM and FCMM-EWM Models as well as the FCMM-EWM with FENE-P springs (which we call the FC-FENE-P-EWM Model) model. For the FC-FENE-P-EWM Model, we just varied the b_i values to fit elongational viscosity data and kept the other parameters the same as the FCMM-EWM Model. The UMM Model gives a constant viscosity, but the FENE-P Model gives a fairly decent fit to the experimental data and the FCMM-EWM Model gives an exceptionally good fit to the data. When we added FENE-P springs into the FCMM-EWM Model to fit elongational viscosity, the performance of the corresponding FC-FENE-P-EWM Model against the shear viscosity data decreased a little compared with the FCMM-EWM Model. Since the FCMM-EWM Model fits the shear viscosity data exceptionally well, we don't expect the FC-FENE-P-EWM Model will improve the fit of shear viscosity, even if we fit the FC-FENE-P-EWM Model to the shear viscosity data. Therefore, the FENE-P spring can dramatically improve the performance on shear thinning behavior only compared to the simple UMM Model.

[5] All the tables and figures are located in the appendix at the end of the part

6.4.2 The Performance of the FENE-P Spring in Elongational Viscosity

In Figure 6.2, we plot the elongational viscosity as a function of time for different elongational rates according to the FENE-P and UMM Models. From this figure, we can see that the elongational viscosity of the FENE-P Model increases much sharper than the UMM Model, and reaches a steady-state value faster. It is fair to say that the FENE-P Model gives a worse prediction of elongational viscosity than the UMM Model.

In Figure 6.3, we plot the elongational viscosity as a function of time for different elongational rates according to the FC-FENE-P-EWM Model and the FCMM-EWM Model. From this figure, we can see that elongational viscosity of the FC-FENE-P-EWM Model increases much more sharply than the FCMM-EWM Model of Part 4, and reaches a steady-state value more easily. These observations are similar to the performance of the FENE-P Model.

6.5 Conclusion

We examined the effect of replacing linear springs (Maxwell Modes) with finitely-extensible non-linear elastic springs (FENE-P Modes) in eight viscoelastic rheological models spanning uncoupled linear models, uncoupled non-linear modes, and coupled linear models. For all of the models considered, similar results were obtained. The introduction of the FENE-P extension increases the slope of elongational viscosity vs. time curves, and causes the elongational viscosity to reach a steady state at a lower value. For the polymer studied in this work, the introduction of the FENE-P modes did not result in an improved capability of the models to predict or fit experimental data for the elongational viscosity.

References

6.1 R.B. Bird, R.C. Armstrong, and O. Hassager, *Dynamics of Polymeric Fluids*. 2 ed. Vol. 1. 1987: John Wiley and Sons.

6.2 R.B. Bird, C.F. Curtiss, R.C. Armstrong, and O. Hassager, *Dynamics of Polymeric Fluids*. 2 ed. Vol. 2. 1987: John Wiley and Sons.

6.3 G.W. Slater, S.J. Hubert, and G.I. Nixon, *Macromol. Theory Simul.*, 1994(3): p. 695.

6.4 A.P. G. van Heel, M.A. Hulsen, and B.H.A.A. van den Brule, *J. Non-Newtonian Fluid Mech.*, 1998. **75**: p. 253.

6.5 A. N. Beris and B.J. Edwards, *Thermodynamics of Flowing Systems*. 1994, New York: Oxford University Press.

6.6 A. Peterlin, *Polymer*, 1961(2): p. 257.

Appendix

Tables

Table 6.1: Parameters of the FENE-P Model, used to fit the data for complex modulus, shear viscosity, and first normal stress coefficient.

Mode No.	1	2	3	4	5	6
Λ	1.243e-3	4.978e-3	2.297e-1	9.527e-1	5.514	4.570e-2
N	2.131e-12	2.289e1	2.024	8.747e-1	2.923e-1	5.450
B	1.099e1	1.000e1	1.000e1	1.271e1	1.260e1	1.000e1

Table 6.2: Parameters of the FC-FENE-P-EWM Model, used to fit elongational viscosity.

a) Parameters for each mode.

Mode No.	1	2	3	4	5	6
$\lambda_{0,i}$ (s)	1.637E-4	2.391E-2	3.153E-2	1.015E+1	1.585	2.346E-1
n_i $(\mathrm{mol/m^3})$	7.076E-4	3.461E+1	7.329	1.347E-1	7.747E-1	2.693
k_i	-9.009E-2	-2.670	-1.320E2	-4.564E-1	-9.662E-1	-4.049
b_i	1.174e5	1.452e5	1.128e5	5.532e1	1.034e5	1.062e5

b) Coupling factors between the modes

θ_{ij}	1	2	3	4	5	6
1	-	2.215E-12	1.284E-20	1.781E-20	1.122E-10	1.787E-10
2	2.215E-12	-	1.082E-19	1.212E-20	1.316E-20	2.408E-20
3	1.284E-20	1.082E-19	-	1.236E-20	1.185E-20	4.121E-12
4	1.781E-20	1.212E-20	1.236E-20	-	1.854E-20	8.720E-9
5	1.122E-10	1.316E-20	1.185E-20	1.854E-20	-	6.446E-20
6	1.787E-10	2.408E-20	4.121E-12	8.720E-9	6.446E-20	-

Figures

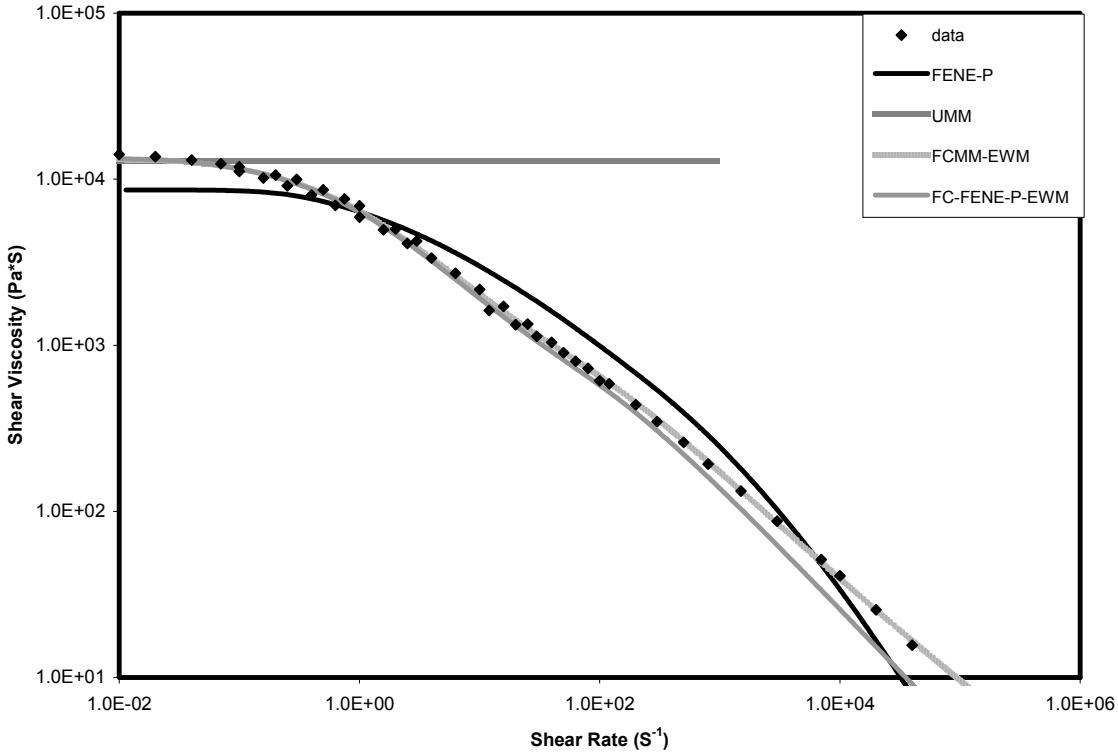

Figure 6.1: Comparison of the FENE-P, UMM, FCMM-EWM and FC-FENE-P-EWM Models for shear viscosity as a function of shear rate.

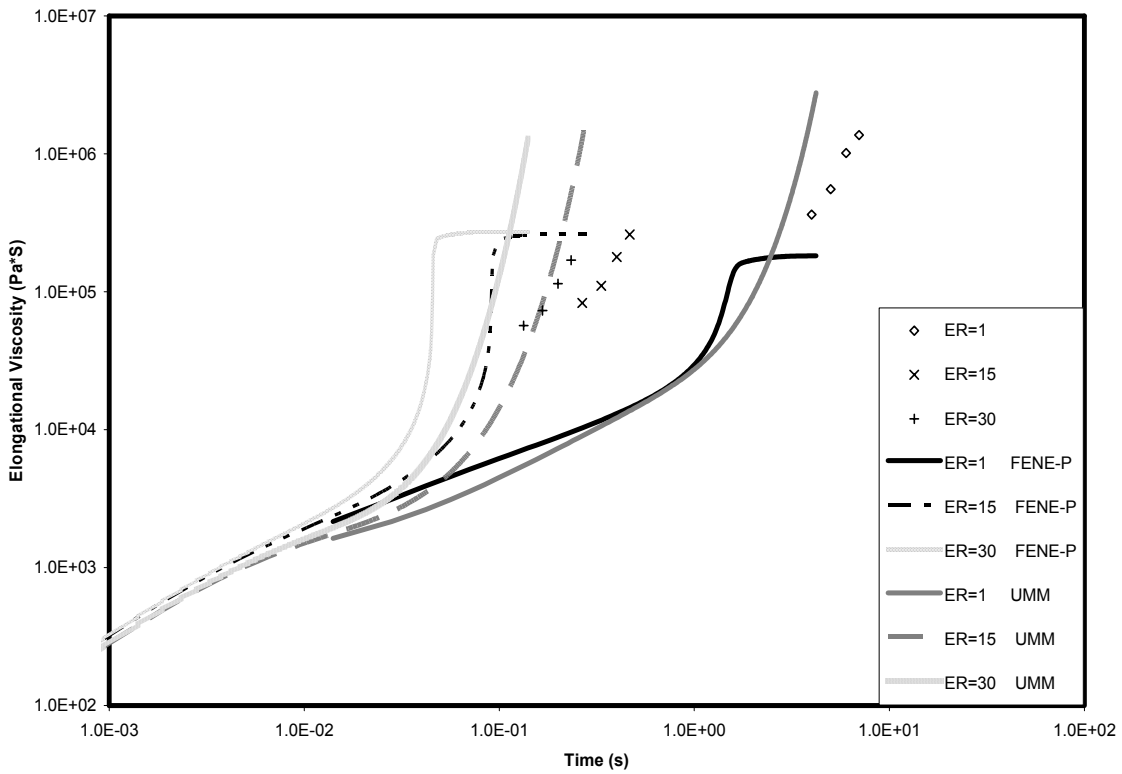

Figure 6.2: Comparison of the FENE-P and UMM Models for elongational viscosity as a function of time.

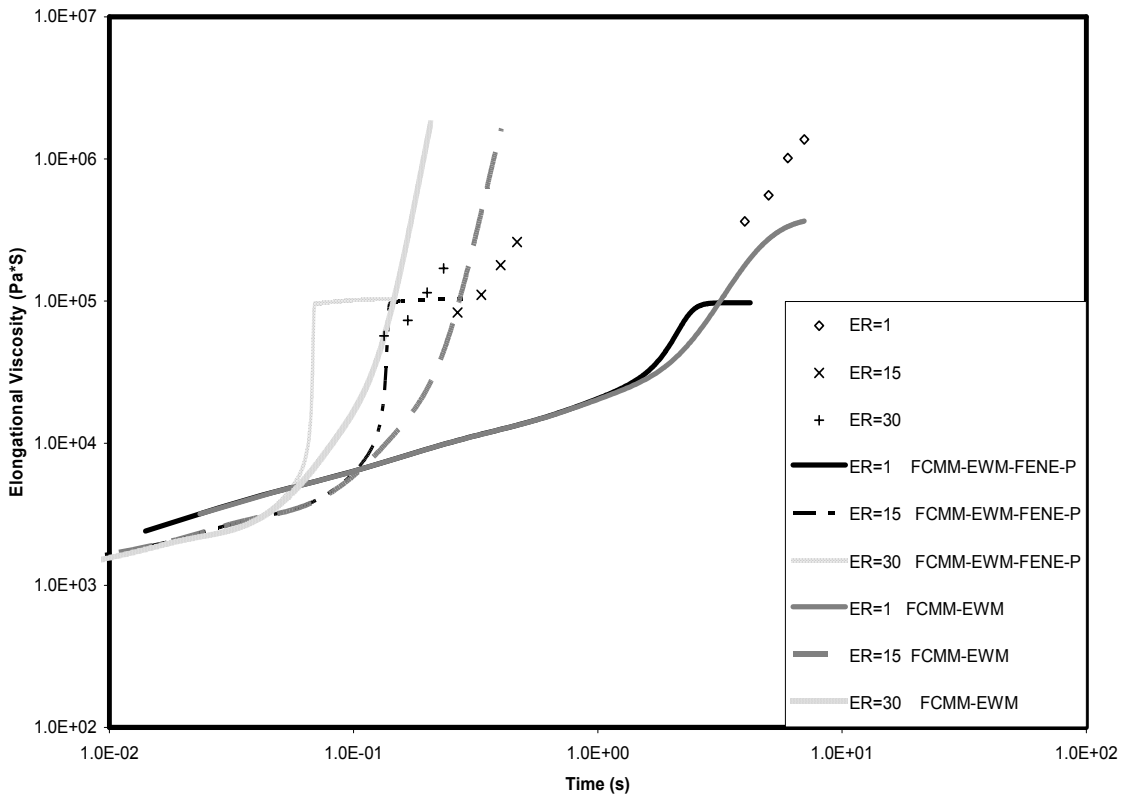

Figure 6.3: Comparison of the FC-FENE-P-EWM Model and the FCMM-EWM Model for elongational viscosity as a function of time.

PART 7

Conclusion

In Part 2, we studied the performance of the Two Coupled Maxwell Modes (TCMM) Model in describing shear-thickening behavior, which can be observed under certain conditions for high molecular weight polymers dissolved in low viscosity solvents. A full parameterization of the TCMM Model was performed by using all of the available experimental data for steady shear viscosity and dichroism in the literature. The TCMM Model gave reasonable functional dependencies of its parameters, including temperature, concentration, and molecular weight of polymer.

In Part 3, we used the Multiple Coupled Maxwell Modes Model (with pair-wise coupling) to study a typical, industrial low-density polyethylene in diverse flow fields, including (i) transient and steady-state shear flow, (ii) small-amplitude oscillatory shear flow, and (iii) transient uniaxial elongational flow.

In Part 4, several classes of multiple-mode rheological constitutive equations were examined for fitting and predicting viscoelastic flow properties of the same polymer melt as used in Part 3. Model parameters were optimized using easily obtained rheological data, and the models were then used to generate predictions for more difficult transient shear and uniaxial elongational flow experiments. These predictions were then compared to experimental data. Several models, such as the FCMM, PCMM, and FCMM-EWM Models, can give quantitative descriptions of data in different types of flow.

In Part 5, we used the same models and parameters as in Part 4 to generate predictions of data for step-strain experiments, and then compared the predictions with the experimental data. The performances of the different models were presented and discussed. Here, we provide a detailed evaluation of the models in all aspects, as

examined in Table 7.1[6]. In this table, the score for each item is 10 for a nearly perfect quantitative fit of the experimental data. If the model can only qualitatively describe a data set, we give this model 3 points. The remaining 7 points were decided by the RMS error between the experimental data and the theoretical results. From Table 7.1, we see that the FCMM-EWM and UGM Models have almost the same score, which means both models performed the best among the models examined. However, these two models have different numbers of parameters. The number of parameters of each model and the ratio of the total score to the number of parameters are listed in Table 7.2, which demonstrates that the UGM Model has a much better parameter efficiency than FCMM-EWM Model. Note that many modal parameters can turn out to be null valued during the optimization procedure. The numbers in parentheses in Table 7.2 are the ratios subtracting out the null-valued parameters from the denominator.

In Part 6, we replaced the linear elastic springs with finitely-extensible non-linear elastic (FENE) springs in the corresponding models used in Parts 4 and 5. It was hypothesized that this would improve the predictions of the elongational viscosity data. It turned out that the FENE-P springs increased the slopes of elongational viscosity versus time curves, and the elongational viscosity reached a steady-state value more easily. These results contradict the experimental data. Consequently, the FENE-P springs, with their associated increase in the number of fitting parameters, provide no improvement to the model predictions.

[6] All the tables and figures are located in the appendix at the end of the part.

Appendix

Tables

Table 7.1: The assessed score of the performance of all models examined.

Type	$G'\&G''$	$\eta(\dot{\gamma})$	$\psi_1(\dot{\gamma})$	$\psi_2(\dot{\gamma})$	$G(t,\gamma)$	$\sigma_{21}(t,\gamma_1,\gamma_2)$	N_1/σ_{21}	$\eta_e(\dot{\varepsilon})$
Usage	Fit	Fit	Fit	Predict	Predict	Predict	Predict	Predict
UMM	8	2	2	2	7	8	9	4
EWM	8	10	9	2	7	7	8	2
UGM	9	9	8	9	8	6	9	5
PCMM	5	5	5	9	6	5	7	4
FCMM	5	5	5	9	6	5	6	4
PCMM -EWM	7	10	9	3	7	7	6	5
FCMM -EWM	10	10	8	5	9	9	4	7

Table 7.2: Number of parameters and overall performance of all models. (The numbers in parentheses are the number of non-zero parameters.)

Model (N=6)	No. of Parameter	Total Score	Score/No. Para.
UMM	12	42	3.50
EWM	18	53	2.94
UGM	18	63	3.50
PCMM	15	46	3.06
FCMM	27 (16)	45	1.66 (2.81)
PCMM-EWM	21	54	2.57
FCMM-EWM	33 (23)	62	1.87 (2.70)

Vita

Bangwu Jiang was born in Ziyang, Sichuan Province, China on July 1971. He joined the Department of Chemical Engineering at East China University of Science & Technology where he received his Bachelor degree in chemical engineering in 1995. Subsequently he worked in Charioteer pharmaceutical factory, Zhejiang, China for six years. In August 2001, he pursued studies and served as General Teaching Assistant in the Department of Chemical Engineering at the University of Tennessee, Knoxville. He gained his degree of Doctor of Philosophy in Chemical Engineering in August 2005.